Detecting and Molecular Profiling Cancer Cells in Patients

by

Vanessa M. Peterson

B.S. Chemical Engineering
University of Notre Dame, 2003

Submitted to the Department of Chemical Engineering
in partial fulfillment of the requirements for the degree of

Doctor of Philosophy in Chemical Engineering

at the

Massachusetts Institute of Technology

September 2013

Signature of Author .....
Department of Chemical Engineering
July 16, 2013

Certified by .....
Ralph Weissleder
Director of Center for Systems Biology, MGH
Thesis Supervisor

Certified by .....
Robert Langer
David H. Koch Institute Professor
Thesis supervisor

Accepted by .....
Patrick Doyle
Professor of Chemical Engineering
Chairman, Committee for Graduate Students

Detecting and Molecular Profiling Cancer Cells in Patients

by

Vanessa M. Peterson

Submitted to Department of Chemical Engineering on July 16, 2013
in Partial Fulfillment of the Requirements for the Degree of
Doctor of Philosophy in Chemical Engineering

Abstract

Although tumor cells obtained from human patients by surgical biopsy, image-guided intervention, blood draws or fluid drainage (paracentesis, thoracentesis) are a valuable source for analyzing tumor cells, conventional means of proteomic analysis are limited. Highly sensitive and quantitative technologies for point-of-care and multiplexed analysis on small sample sizes are in great demand. To this end, we developed three technologies to improve our understanding of the molecular signatures of cancer in clinical samples.

In the first section, we describe a diagnostic magnetic resonance (DMR) device that was developed for point-of-care analyses of human tumors. We optimized a magnetic nanoparticle assay to improve sensitivity and robustness of the DMR approach. The DMR device was tested by analyzing samples from 50 patients. The results were then validated in an independent cohort of 20 additional patients. DMR enabled quantification of multiple protein markers in all patients. Using a four-protein signature enabled us to achieve 96% accuracy for establishing cancer diagnosis, surpassing conventional clinical analysis by immunohistochemistry. Results also show that protein expression patterns decay with time, underscoring the temporal need for rapid sampling and diagnoses. Also, a surprising degree of heterogeneity in protein expression both across different patient samples and even within the same tumor was observed, which has important implications for molecular diagnostics and therapeutic drug targeting.

In the second section we molecularly profiled tumor cells in ascites - peritoneal fluid frequently drained for symptomatic relief in advanced ovarian cancer (OvCA) patients. First, we profiled a comprehensive panel of 85 biomarkers in ovarian cancer and benign cell lines. From this data set, 31 markers were identified and profiled in a training set of human ascites samples (n=18). We identified an ascites-derived tumor signature termed ATC_{dx} containing four markers which was then validated in a cohort of 47 patients (33 ovarian cancer and 14 control) and correctly identified all 33 ovarian cancer patients. Serial samples were obtained from a subset of patients' serial samples (n=7) and profiled, demonstrating that ATCs can be used to measure treatment response and differentiate responders from non-responders. Finally, we specifically designed a novel microfluidic enrichment chip that allows rapid visualization of cancer

cells in heterogeneous ascites fluid. This chip requires small sample volumes (< 1 mL) and has single cell detection sensitivity. Furthermore, it is inexpensive to construct and can be easily fabricated using soft lithographic techniques, providing a point-of-care method that could potentially find widespread use for ATC analyses and diagnosis.

In the final section, a multiplexed proteomic assay using a photocleavable DNA barcoding method was developed to multiplex protein detection in single cells. We tested 94 antibodies against common cancer markers to examine different treatment responses and heterogeneity at the single cell level. We then extended our analysis to human clinical samples to demonstrate the potential of protein-based measurements to assist in monitoring cancer therapy through differential changes before and after treatment. We show that protein based tumor profiles can provide sufficient information to predict treatment response. Finally, we examined interpatient variability and intratumoral heterogeneity of single cells with this highly sensitive assay.

Together, these technologies can help overcome current clinical limitations and expedite advancements in cancer treatment.

Thesis Supervisors:
Director of the Center for Systems Biology, Ralph Weissleder (MGH)
Koch Institute Professor, Robert Langer (MIT)

Acknowledgements

It has truly been a journey in which I would never have been able to venture alone. I can't express enough gratitude for all the help and support from family, friends, and colleagues along the way.

First and foremost, I would like to thank my thesis advisors, Ralph and Bob for being generous with their time and providing guidance throughout my thesis construction. A special thanks to Ralph for giving me the opportunity to work in his lab at MGH as well as the many resources he made available during my research. I learned so much from his clinical and translational perspective, never losing sight of the big picture. Despite his busy schedule, he always made the time to meet whenever I needed him. His high efficiency, organization, and quick turnaround time on revisions never ceased to impress me. Hopefully, some of that has rubbed off on me.

Next, I would like to thank my thesis committee members, Kristala Prather and Cesar Castro for their scientific input on my projects. They offered intellectual insight by providing constructive feedback and sharing their expertise during our meetings. Cesar, thank you so much for our lengthy discussions. It was always so helpful to brainstorm and learn with you. You even took time to answer personal questions on cancer and connected family and friends with top-notch doctors. Your altruistic nature and continual willingness to help won't be forgotten.

Merck, for the amazing opportunity to go back to school through the doctoral assistance program, I am eternally grateful. Thank you John Lepore for all your patience and support through this 'longer-than-expected' journey through graduate school.

Although my thesis committee provided me with tools to complete a successful dissertation, the friends I met during this time deserve equal mention. These are people with whom I shared the highs and lows of my Ph.D. on a daily basis. I was lucky to be surrounded by such great labmates that were extremely intelligent, but more importantly patient, generous, and caring people. Jered Haun, for taking me under your wing when I first joined the lab and providing me with a strong foundation in biological research, for your unwavering patience and cheerfulness always made the lab atmosphere enjoyable, you are thought of highly. Thank you Greg Thurber and Jonathan Carlson, for always taking the time to answer my questions with thorough explanations. Jonathan, I appreciate all your computer technical support despite my disorderly and frustrating laptop settings. Also, I can never thank you enough for connecting my sister with such a fantastic surgeon and oncologist in Ohio.

Adeeti, aka Ethel, I will never forget our "I Love Lucy" chocolate factory moments in lab when we would start laughing so hard that we would end up crying. It made lab work fun even when we would take on way more than we could handle and end up sprinting to the T to catch the last train home. I will never forget all our NanoString memories. Undoubtedly, these are the moments I will first think of when I look back on graduate school.

Nathan, Tuang, and Maria, it was such a pleasure to work with you in the lab. I couldn't have done it without all your help. You consistently surpassed my expectations. I know you have bright futures in medical school along with all other endeavors you pursue.

I want to thank the Teresa's in my life. All the 15 minute talks really added up over the past 5 years and have helped make this journey an enjoyable one that I wouldn't trade in for the world. I am thankful for the growth and indispensable tools that have filled me with gratitude and an awareness for all the gifts life presents us with every day.

Most importantly, I wanted to thank my family. Especially to my mother and father, who from an early age instilled in me the importance of education and a strong work ethic. They always led by example and took the time out of their busy schedules to go above and beyond the role of parents. They were my teachers, coaches, and number one fans throughout my life. They always made sure that school was a priority amongst all the soccer practices, games, and tournaments that consumed the majority of my time. Getting quizzed on my multiplication factors while practicing soccer in the backyard ended up being early training for the balance needed to propel me in school. Although there have been some changes over the past few years, your love and support for me has never wavered. The memories we shared together will always be looked back upon with smiles and deep love.

I also wanted to thank my older sister Stephanie who has continuously helped pave the way for me. The advice you gave me throughout graduate school was invaluable and much appreciated. My younger brother Kevin, it was a pleasure getting to live so close to you during this time. It was always a real comfort knowing you were just around the corner. I will never forget our fun pick-up soccer league memories that were always nice break from school work.

Last but not least, I wanted to thank my husband and best friend, Ryan for all his patience and support throughout my Ph.D. You always believed in me more than I did in myself. I know all the late nights and weekends in lab must have been difficult for you in our first few years of marriage. I appreciate your caring concern and eagerness to listen. Thank you for all the reminders that thesis research is a learning experience and curing cancer is not a requirement. You know how to keep me grounded and never fail to bring a smile to my face with your humor. Your lunchtime and dinner visits were always well needed refreshing breaks. I appreciate the numerous times you went out of your way to adjust to my difficult to predict schedule and erroneous estimations when experiments would finish. Your continuous passion to learn and help others is contagious. I have learned so much from you throughout these years and continue to do so. All of our mindfulness and savoring discussions helped me to stay present and positive throughout my Ph.D work.

I wanted to dedicate this thesis in memory of my cousin and godmother, Liz Schermerhorn. Your laughter and smile always filled the room. The fun family picnics, badminton games, and blue cheese jokes are memories that will always be cherished.

I am lucky to have such a loving family (extended family, grandparents, uncles, and aunts) without whose support I could not have embraced this experience. Thank you to all of you!

Table of Contents

Abstract **2**
Acknowledgements **3**
List of Figures **10**
List of Tables **16**
Chapter 1 ..... **17**
Introduction
1.1 Thesis Organization 17
1.2 Clinical needs in cancer field 18
1.2.1 Protein expression patterns in cancer 18
1.2.2 Clinical sources of cancer cells 19
1.2.3 Treatment response 20
1.2.4 Technological needs 21
1.3 Diagnostic Magnetic Resonance (DMR) Technology 22
1.3.1 DMR Device 23
1.3.2 Magnetic nanoparticles 25
1.3.3 Cellular Magnetic labeling 26
1.3.4 NMR theory 27
1.4 Microfluidic technology 28
1.5 DNA barcoding Technology 30
Chapter 2 ..... **35**
Optimized Diagnostic Magnetic Resonance (DMR) Assay
Abstract 35
2.1 Introduction 36
2.2 Materials and Methods 37
2.2.1 Preparation of cleavable pegylated Tz and TCO nanoparticles (NPs) 37
2.2.2 Preparation of TCO-modified antibodies 39
2.2.3 Nanoparticle labeling 39
2.2.4 DMR measurements 40
2.2.5 Flow cytometry 41
2.2.6 Microscopy 42
2.2.7 Clinical samples 42
2.3 Results and Discussion 43
2.3.1 New labeling strategy for high detection sensitivity 43
2.3.2 Improved robustness and sensitivity through cleavage 45
2.3.3 Multiple amplification rounds yield higher SNRs 47
2.3.4 Application to Clinical Samples 50
2.4 Disscusion and Conclusions 52
Chapter 3 ..... **54**
DMR Technology applied to Fine Needle Aspirate (FNA) Clinical Study
Abstract 54
3.1 Introduction 55
3.2 Materials and Methods 57
3.2.1 Patient population and trial design 57

3.2.2 Sample processing 59
3.2.3 Preparation of trans-cyclooctene (TCO)-modified antibodies. 59
3.2.4 Preparation of tetrazine (Tz) modified magnetic nanoparticles (MNPs) 60
3.2.5 MNP targeting and detection by nuclear magnetic resonance 61
3.2.6 The μNMR device and its operation 62
3.2.7 Statistics 63
3.3 Results and Discussion 64
3.3.1 Cellular samples can be quantitated 64
3.3.2 Heterogenous protein expression levels across epithelial tumors 67
3.3.3 Diagnostic sensitivity, specificity, and accuracy of cancer markers 68
3.3.4 Confirmation in independent test set 71
3.3.5 Comparison to the standard-of-care 72
3.3.6 Other markers 73
3.3.7 Variability 74
3.4 Conclusions 76
Chapter 4 82
Profiling Ascites Tumor Cells (ATCs) reveals reliable targets for detection using a novel point-of-care microfluidic chip
Abstract 82
4.1 Introduction 83
4.2 Material and Methods 85
4.2.1 Patient population and analyses 85
4.2.2 Cell culture 87
4.2.3 Bulk ascites processing for more extensive profiling 88
4.2.4 CD45 Purification Step 89
4.2.5 Cell Labeling 90
4.2.6 Flow Cytometry 91
4.2.7 Statistical analysis 91
4.2.8 ATC device fabrication 93
4.2.9 Processing cells through the ATC chip 94
4.3 Results and Discussion 95
4.3.1 Experimental approach 95
4.3.2 Unique marker expression in a training set of human ascites samples 99
4.3.3 Prospective ATC profiling in a test set of human ascites samples 102
4.3.4 Serial testing to measure treatment response in individual patients 104
4.3.5 Differentiating responders from non-responders 106
4.3.6 Ascites specimen cellular composition 107
4.3.7 ATC enrichment and detection using a point-of-care microfluidic chip 109
4.4 Conclusions 110
Chapter 5 114
Multiplexed DNA Barcode Protein Assay for Molecular Profiling Cancer Cells
Abstract 114
5.1 Introduction 115
5.2 Materials and Methods 116
5.2.1 Cell lines 116
5.2.2 Clinical samples 117
5.2.3 Drug treatments 118
5.2.4 Flow cytometry 118
5.2.5 Synthesis of photocleavable DNA-antibody bifunctional linker 119
5.2.6 DNA-Antibody conjugations 120
5.2.7 Antibody storage and characterization 122
5.2.8 Linker optimization 123
5.2.9 Lysis optimization 126
5.2.10 Antibody staining and DNA collection for protein profiling 127

5.2.11 Fluorescent read-out 129
5.2.12 Single cell isolation and processing 130
5.2.13 Calculating proteomic expression profiles 130
5.2.14 Clustering 130
5.2.15 Statistical analysis 131
5.3 Results and Discussion 132
5.3.1 Single cell sensitivity 134
5.3.2 Intratumor heterogeneity 135
5.3.3 Interpatient heterogeneity 136
5.3.4 Treatment response monitoring 139
5.4 Conclusion 143
Chapter 6 144
Conclusions and Recommendations
Abstract 144
6.1 Summary 145
6.1.1 Chapter 2 145
6.1.2 Chapter 3 147
6.1.3 Chapter 4 148
6.1.4 Chapter 5 149
6.2 Recommendations for future work 149
References 152
Appendix A 164
Appendix B 167
Appendix C 169

List of Figures

Figure 1- 1. Potential sources of cancer cells in clinical samples; circulating tumor cells (CTCs), fine needle aspirates (FNA), ascites, and surgery. The main focus of this thesis is on fine needle aspirates (Chapter 3 and Chapter 5) and ascites (Chapter 4) samples. From left to right the typical number of cancer cells obtained from these samples increase. However, the invasiveness of the procedure also increases while the repeatability decreases. Exceptions to this trend are the similar repeatability and invasiveness features between ascites and FNA's 20

Figure 1-2. DMR system. (A) The schematic of the DMR system consists of a miniaturized microcoil for NMR measurements, microfluidic networks for sample handling and mixing, embedded NMR electronics, and a permanent magnet for polarizing magnetic field generation. The microcoil generates RF magnetic fields to excite samples and receives the resulting NMR signal. The NMR electronics that is designed to perform T_1 and T_2 measurements via inversion-recovery and CPMG pulse sequences, respectively. (B) The complete DMR-3 system for near-patient use. The bottom component contains all the electronic circuitry for NMR measurements while the top enclosure holds a permanent magnet and chip-sized, μL-volume sensors 24

Figure 1-3. Principle of magnetic targeting assay. Cells can be targeted with magnetic particles to alter the magnetic properties of surrounding water molecules. Magnetic nanoparticles cluster upon binding to targets which decrease the spin-spin relaxation time (T_2) of surrounding water protons. DMR measurements are shown in the bottom graphs where T_2 decreases when MNP clusters are present..... 26

Figure 1-4. Schematic of perturbation of hydrogen nuclei magnetic moments. (A) The magnetic moments of the hydrogen nuclei in water molecules originally start off aligned in the permanent magnetic field of the DMR device in the z-direction. (B) Then the magnetic moments are pushed into the xy plane when an alternating current is passed through the microcoil of the device. (C) The magentic moments eventually become out of phase with each other. (D) The decrease in the magnetic field in the xy plane (M_{xy}) over time is fitted to an exponential decay curve to determine the relaxation time, T_2. (35)..... 28

Figure 1-5. The fabrication of micropatterns using soft lithographic techniques. (A-B) A silicon wafer is spin-coated with photoresist. (C) A mask is placed on the photoresist layer. (D) The photoresist layer is then crosslinked by exposure to ultraviolet (UV) light. Then an organic solvent is used to dissolve the photoresist that was hidden under the mask and not crosslinked. This results in a master mold consisting of a silicon wafer with a pattern made of photoresist. (E) Then poly(dimethylsiloxane) (PDMS) is poured on the master, cured, and peeled away. (F) The final product is a PDMS layer consisting of micropatterns that can range in size from nanometer to micrometers. (42) 30

Figure 1-6. Schematic of NanoString Assay. (A) Schematic representation of the capture probe and the reporter probes bound to the target mRNA molecule. (B) (i)The target-probe complex is captured to the streptavidin coated surface via the biotin at the end of the capture probe. (ii) Then biotinylated complementary sequences to the 5' repeat section of the reporter probe are added and (iii) a voltage is applied so that the target-probe complex lays flat on the surface of the cartirdge. (C) Then the analyzer takes an image of the surface and counts the number of unique reporter probes present. (43) 32

Figure 1-7. Overview of the NanoString's digital profiling technology for mRNA. (A) NanoString's Technolog uses two probes, a reporter probe and a capture probe. The capture probe allows the target-probe complex to be immobilized for data colection and the reporter probe contains the flourescent barcode signal. (B) The reporter and capture probe hybridize with the target mRNA in solution (C) After the hybridization step, the excess probes are removed and (D) the target-probe complex is immoblized on the nCounter cartridge using the Prep station. (E) The surface is imaged and the barcodes are then counted and tabulated for each target molcule usng the Digital analyzer. (44) 34

Figure 2-1. Schematic of the labeling strategy used to amplify biomarker signals. The labeling step (L) refers to the initial antibody-*trans*-cyclooctene (TCO) conjugate binding to the target followed by the addition of magneto-fluorescent nanoparticles (MFNPs) conjugated to the orthogonal reactant, tetrazine

(Tz) . The signal can be subsequently amplified through additional rounds of complementary orthogonal MFNP conjugates (AMP1, AMP2) and through cleavage/purification using dithiothreitol (DTT; AMP1-C, AMP2-C). 44

Figure 2-2. Effect of nanoparticle (NP) PEGylation on signal-to-noise ratio (SNR). (A) Flow cytometry experiments comparing SK-OV-3 cells (in the absence of the primary antibody labeling step) incubated with either MFNP-PEG-Tz (green) or MFNP-Tz (orange) for 15 minutes to determine nonspecific cellular binding. PEGlyated particles displayed significantly reduced nonspecific cellular binding. (B) Dose response graphs of specific cellular (*i.e.* HER2 targeting) *versus* nonspecific cellular binding with different NPs. With PEGlayted MFNPs (left panel), non-specific binding is kept at a minimum non-significant level, whereas the non-specific binding increases in a dose-dependent manner with non-PEGlayed MFNPs (right panel). (C) The overall signal-to-noise ratio (SNR) with PEGlyated (green) and non-PEGlyated (orange) MFNPs. 45

Figure 2-3. Comparison of the cleavage method to whole cell detection. (A) Comparative NMR signals for HER2-targeted SK-OV-3 cells using the cleave (blue) *versus* the non-cleave (yellow) method (~3,500 cells); control samples were incubated with NPs alone. (B) Detection sensitivity of SK-OV-3 cancer cells using the AMP1 and AMP1-C methods (**See Figure 2-1**). Note the ~10-fold increase in detection sensitivity following the cleavage method. Data are expressed as a mean ± standard deviation. (C) Comparative detection between the NMR-based cleavage method and flow cytometry demonstrated an excellent correlation (R^2 = 0.99). Expression levels of four markers (EGFR, EpCAM, HER2, MUC1) across two model cell lines (SK-OV-3, SK-BR-3) were pooled together. NMR detection was performed on ~3,500 cells whereas flow cytometry used ~35,000 cells. MFI: mean fluorescent intensity.... 47

Fig 2-4. Comparison of successive amplification rounds. (A) Fluorescent signals detected from the initial labeling step and for each subsequent amplification step showed excellent co-localization, confirming that multiple MFNP layers can be applied to cellular targets for signal amplification. The MFNP-cleaved cells displayed negligible fluorescent signal, suggesting maximal MFNP release into suspension. The scale bar represents 30 µm. (B) Comparative NMR signal for HER2-targeted SK-OV-3 cells (3,500 cells). AMP2-C conferred the largest increase in SNR but AMP1-C had the highest SNR/unit time. (C) Cellular detection threshold for different cleavage methods (Labeling, AMP1, and AMP2; see **Figure 2-1**) based on HER2 targeting of SK-OV-3 cells. 49

Figure 2-5. Processing of primary clinical samples. (A) Human clinical ascites from pancreatic cancer was profiled for 4 different biomarkers: EGFR, EpCAM, HER2, and MUC1. The AMP1 labeling method was then assessed with and without the subsequent cleavage step. The cleavage step generated higher signal levels. (B) Comparison of different analytical methods (flow cytometry, diagnostic magnetic resonance) for MUC1 detection in clinical samples. Error bars represent the standard error from at least three NMR measurements. 51

Figure 3-1. The effect of prospective preservation treatments on extracellular (A) and intracellular (B) protein measurements. Live: live cells; FA: 2% formaldehyde; meth: 100% methanol; TX: triton X-100 0.05% in PBS, FB1: Fix buffer 1, BD Biosciences; Sap: saponin. *: optimized conditions chosen for subsequent experiments. 59

Figure 3-2. Validation of NMR measurements. Plots showing the correlation of EGFR measurements obtained by µNMR versus ELISA, FACS or immunohistochemistry (IHC) in clinical samples where sufficient cells were available for conventional proteomic techniques (typically 10^{5-6} for ELISA and FACS versus 10^2 for DMR). Note the excellent correlation coefficients for the different methods. Bottom: representative immunofluorescent stains of a representative human sample. The primary antibody (green) was labeled with AlexaFluor-488 and TCO. The magnetic nanoparticle (red) was labeled with VT680 and Tz. Note excellent co-localization between nanoparticles (conferring NMR properties) and antibody (protein content). 66

Figure 3-3. Biomarker expression level distribution. Waterfall plots showing the expression levels of each of the different biomarkers sorted from high (left) to low (right). Each column represents a different patient sample (green = malignant; blue = benign). 67

Figure 3-4. Expression levels of different biomarkers arranged by patient number. Patients 5, 12, 17, 18, 21, 42 had benign lesions. 68

Figure 3-5. Receiver operating characteristic (ROC) curves for single markers, a dual marker set, as well as for triple and quadruple marker combinations to determine optimum DMR threshold values. A_z: area under the curve. 95% CL: 95% confidence limits. 69

Figure 3-6. Analysis of sample heterogeneity. (A) Repeat measurement of the same samples (note the different scale compared to other graphs). (B) Measurement of repeat FNA samples obtained via the same coaxial needle. (C) Measurement of repeat FNAs from different tumor sites. (D) The effect of time at 4°C before fixation (e.g. during transport to central laboratory facility) on protein measurements. Note the rapid change in expression levels in unfixed samples. 76

Figure 4-1. ROC analyses of training set. ROC curves were plotted for individual markers using the 13 OvCA and 13 benign samples of the training set (top). The area under the curve (AUC) and the optimal cutoff level were calculated and are summarized in the bottom table. The cutoff values were then used to determine the sensitivity, specificity, accuracy of each individual marker and the V3 and ATC_{dx} panel 92

Figure 4-2. ATC chip design and measurements. (A) The layout of the ATC chip with 4 differently sized wells (n = 4,925) for cell capture. (B) An example of captured cells (green represents DAPI staining) on micro-wells. 94

Figure 4-3. Schematic of on-chip purification and labeling. (A) First, ascites fluid is collected from the patient which contains malignant cells amongst aninflammatory milieu of host cells. (B) Ascites cells are added to the chip followed by an antibody cocktail (calretinin-Biotin, CD45-Biotin, EpCAM-FITC, Vimentin-RITC). Then streptavidin-coated magnetic particles and Anti-Rabbit Dylight 650 bind to the rabbit biotinylated calretinin and CD45 antibodies. (C) A magnet under the inlet allows the non-magnetically labeled malignant cells to pass freely through the microchip while the benign cells are bound to the magnet. The four different size microwells (40, 30, 20,15 um) allow for capture of the malignant cells while allowing for the typically smaller leukocytes to pass through the device. (D) The ATCdx signature (EpCAM+ and/or Vimentin+/Calretinin-/CD45-) can then be imaged to determine number of ATCs....95

Figure 4-4. Schematic approach. A total of 85 putative ovarian cancer protein markers were identified through literature, database and other screens (top left). Markers were tested in 12 ovarian cell lines (**Figure 4-5**) and a subset examined in ascites from human patients (**bottom left; n=65; Figure 4-6 and 4-7**). A microfluidic chip (**Figure 4-3**) was developed for point-of-care analysis (bottom right). 96

Figure 4-5. Profiling of cancer cell lines. Twelve different ovarian cancer (OvCA) cell lines, and six benign cell lines (two mesothelial cell lines (LP9, LP3); two benign ovarian cell lines (TIOSE4,TIOSE6); primary human lymphocytes/neutrophils) were tested for their expression levels (λ=signal/background-1) of putative diagnostic protein markers using flow cytometry. For each marker the frequency of cell lines with λ >1.5 (red) are shown on right hand side of the heat map (grey bar) and are rank-ordered by abundance. The data is categorized into 4 subgroups: i) markers present in malignant cells (Unique Malignant; top left), ii) markers in malignant and benign cells (Ubiquitous, right), iii) markers in benign cells only (Benign; middle left), and iv) markers absent in both cell types (Absent; bottom left). This dataset was used to identify markers for subsequent analysis of primary human samples (**Figure 4-6**). Parenthesis represents different antibodies used for the same marker (**Appendix A**). The CD56 antibody (clone MOC-31) used in this screening was found to cross react with EpCAM therefore was not used in clinical sample profiling. 98

Figure 4-6. Profiling of primary human samples in training set. (A) Multicolor flow cytometry was used for gating of mesothelial (calretinin+), leukocytes (CD45+), and CD45/Calret- cells. (B) A subgroup of 31 markers identified in the cell line screen (**Figure 4-5**) were subsequently tested in a training set (n=19). The data are rank-ordered by abundance (yellow = lowest; red = highest). The markers were placed into four different categories: unique malignant, overlapping markers (Ubiquitous), benign, and absent using cutoffs described in the methods section. The three OvCA patients with lowest EpCAM expression levels had the highest vimentin expression levels suggestive of epithelial to mesenchymal

transition (EMT). This training set led to identification of the ATC_{dx} panel where malignancy is defined by either having an EpCAM+ and/or V3+ (Vimentin+/Calretinin-/CD45-) signature. Heatmap values are the log ratio of the fluorescent signal over the ctrl (λ=Sig/Ctrl-1) where the ctrl is the secondary antibody without the primary antibody. 100

Figure 4-7. Prospective testing of ATC marker panels in 47 patients. (A) Ascites samples were tested for the presence of 6 individual markers in 33 ovarian cancer patients (left) and 14 controls (right). EpCAM alone was positive in 31 samples. By using the V3 marker set (Vimentin+/Calretinin-/CD45-) and EpCAM together (ATC_{dx}), all 33 samples were correctly identified (green heat map). ATCs were identified in malignant samples, but not in benign, samples. Grey squares represent data not measured due to insufficient number of cells for flow cytometry. Color scale is same as Fig. 3. (B) Waterfall plots of the individual markers profiled in the test set. Dotted red lines represent the optimal threshold values determined from ROC analyses performed on the training set. 103

Figure 4-8. Serial analysis of ATCs. ATCs were obtained serially from a single patient over a 14 week treatment cycle. Carboplatin and Paclitaxel (Taxol®) were given in weeks 2 and 5, and Bevazucimab (Avastin®) was given in week 11. The number of ATCs were measured over the course of treatment (ATC burden) using ATCdx. Additionally, protein markers related to biological processes such as proliferation (Ki67, pH3, pCyclinD), mRNA translation (p4E-BP1), DNA repair (Ku80, pH2Ax, 53BP1) apoptosis (cleaved CASP3, cleaved CASP8, cleaved CASP9, cleaved PARP) and pathway inhibition (pS6RP, p53, pERK) were also measured. This demonstrates that molecular profiling of ascites can be used as a tool to monitor treatment response over the course of therapy. All samples were stained with DAPI, Calretinin, and CD45 antibodies and gated to exclude doublets, mesothelial cells, and leukocytes respectively. Data are expressed as the average of the mean fluorescent intensity +/- SEM. 105

Figure 4-9. Predictive ATC markers of treatment response. Key treatment response markers are plotted for 6 patients who were analyzed serially and either responded to treatment (left) or progressed (right). Responders typically have proliferation (Ki67, pH3, pCyclinD), mRNA translation (p4E-BP1) and protein translation (pS6RP) markers downregulated compared to the non-responders. Each marker was measured in duplicate for each time point and the error bars represent the SE. 107

Figure 4-10. Ascites cellular composition and volume. Ascites samples from 65 patients with (blue; n=46) or without (green; n=19) ovarian cancer were analyzed for total cell number (top left), malignant cell number (bottom left; ATCs), cell volume (top right) and fraction of malignant cells compared to total cells (bottom right). Viable cells were counted using trypan blue staining and the Countess cell counter (Invitrogen). Malignant cell number were determined using ATCdx via flow cytometry. Data are plotted as waterfall plots. 108

Figure 4-11. Design of microfluidic chip for ATC analysis. (A) A microfluidic chip, containing multiple and differently sized cell capture scaffolds, was designed for high fluid throughput (see **Figure 4-1** for details). The chip was designed to be optically transparent so that staining could be performed directly on-chip. (B) Using this device, ATCs were enriched by 57-fold, and each well was capable of capturing either one cell or clusters of cells. Staining for EpCAM (green) and CD45/Calretinin (red) for benign host cells is shown. ATCs appear larger and do not overlap with host cells. 110

Figure 5-1. Synthesis of photocleavable bifunctional linker. 120

Figure 5-2. DNA per antibody for each Conjugate. The number of alien DNA fragments per antibody was measured by NanoString method (shown in graph) and independently confirmed by ssDNA quantification and Qubit protein measurement. On average there were 3-5 DNA fragments per antibody. 123

Figure 5-3. Scheme of DNA-antibody conjugation. (A) DNA and antibodies were linked through a photocleavable bifunctional linker. The linker was first reacted with the amine groups on the antibody for 1.5 hr at RT. After excess small molecule was removed, thiolated DNA was added at 10x excess to the antibody-linker mix. The final antibody-DNA chimera was purified via both size separation and IgG specific pulldown. DNA could subsequently be released most efficiently by photocleavage at a specific wavelength (365 nm) as shown across a number of wavelengths. A time course of the photocleavage

reaction indicates that maximal release is reached within 15 min. (B) Alternative linker strategies were investigated but not pursued further due to their reduced cleavage efficiency (DTT; linker 1: tetrazine-trans-cyclooctene click chemistry; linker 2: Traut's reagent and the photocleavable bifunctional linker). Linker cleavage was tested by measuring released DNA via NanoDrop and directly on the NanoString platform. The optimized photocleavable linker had a 2.4x greater signal compared to DTT, and over 10x more signal than linker 1 or 2. 126

Figure 5-4. Optimizing lysis and blocking methods. Four different lysis and blocking methods (A-D) were used to recover DNA from labeled cells. Lysate conditions included A) Proteinase K + PKD lysis buffer, B) Proteinase K + ATL lysis buffer, C) ATL lysis buffer alone and D) UV cleavage alone (no cell lysis). The lysate conditions were tested in duplicate (x-axis) measuring DNA signal (y-axis) and different intracellular proteins (z-axis). The best reaction condition was method B (Proteinase K + ATL lysis buffer). Using method B with a photocleavage yielded an additional 20% increase in signal. 127

Figure 5-5. Correlation to Flow Cytometry. (A) Bulk cell analysis from DNA barcoding shows high cancer antigen presence in ovarian cancer cell lines SKOV3 (high CD44, Her2) and ES2 (high CD44) but low cancer marker expression in benign ovarian epithelial cell line TIOSE6. (B) Results for each marker (y axis) correlate linearly with high, significant correlations for all three cell lines (SKOV3: Pearson R = 0.96, r^2 = 0.89, p <.0001; ES2: Pearson R = 0.96, r^2 = 0.91, p <.0001; TiOSE6: Pearson R = 0.78, r^2 = 0.60, p <. 0001). In addition, profiling on SKOV3 and ES2 cell lines with DNA-conjugated antibodies, showed high correlation to profiling with unmodified antibodies (SKOV3: Pearson R = 0.93, r^2 = 0.92, p<.0001; ES2: Pearson R = 0.85, r^2 = 0.72, p<.0001). 129

Figure 5-6. Multiplexed protein analysis in single cells. (Left) Cells are harvested from cancer patients by fine needle aspirate. In this case, a heterogeneous population of EpCam positive cancer cells (green) is displayed alongside mesothelial cells (red) with nuclei shown in blue (Hoechst) from an abdominal fine needle cancer aspirate. Cancer cells were enriched and isolated via magnetic separation on microfluidic devices using both positive (e.g. EpCam/CK+) and negative (e.g. CD45-) selection. (Middle) Cells of interest are "stained" with a cocktail of DNA conjugated antibodies. The conjugates contain a photo-cleavable linker (i**nsert; Figure 5.2**) to allow DNA release after exposure to specific wavelengths of light. DNA-antibody conjugates released from lysed cells are isolated via size-separation and IgG pull down. (Right) Released "alien" DNA barcodes (Appendix C) were processed with a fluorescent DNA barcoding platform (NanoString Technologies). Fluorescent barcodes were hybridized and imaged via a CCD camera. The quantified barcodes were translated to protein expression levels by normalizing according to DNA per antibody and housekeeping genes and subtracting non specific binding from control IgGs. 133

Figure 5-7. Multiplexed cell profiling. Representative example of 88 different antibodies spanning cancer-relevant pathways are profiled in triplicate on the MDA-MB-231 triple negative breast cancer cell line. DNA signal is converted to protein binding by normalizing according to relative DNA per antibody levels. Non-specific binding from expression of six control IgGs is subtracted and expression was normalized by housekeeping proteins. Housekeeping proteins (Cox IV, Histone H3, Tubulin, Actin and GAPDH) are shown at the far right and have consistent expression. 134

Figure 5-8. Detection sensitivity. (A) 500,000 cells from the epidermoid carcinoma cell line, A431, were lysed and processed as shown in Fig. 1. Dilutions corresponding to 5, 15, and 50 cells were then compared to the bulk measurement, showing good correlation at low cell numbers (Spearman R = 0.98). (B) Correlation values for analyzing small cell numbers as well as single cell analysis selected by micromanipulation. (C) Protein expression profiles (log 2 expression values) of four single cells are compared to profiles of the bulk sample. While all cells showed similar relative protein expression, single cells 1 and 2 showed nearly identical profiles to bulk measurements, whereas single cells 3 and 4 showed lower overall protein levels. Correlations were highly significant when comparing all single cells to bulk measurements (p<.0001). 135

Figure 5-9. Single-cell profiling in patient sample. A fine needle aspirate was obtained from a patient with biopsy-proven lung adenocarcinoma. (A) Eleven harvested cells were analyzed individually, and protein expression levels in each cell (y axis) were correlated with expression levels from the bulk tumor sample (x axis). Though all of the cells show a linear trend, the spread and distribution of the markers

varies from cell to cell. (B) Spearman R correlation coefficient values are displayed for each of the single cells to each other and to the bulk measurement. Single cells showed higher correlations to each other as opposed to the bulk. This is expected, as the bulk represents an average measurement of all cells, and thus in a heterogeneous population, is less likely to correlate strongly with a single clonal phenotype. ..136

Figure 5-10. Inter-patient heterogeneity in lung cancer. Fine needle aspirates were obtained from six patients with biopsy-proven lung adenocarcinoma, and bulk samples (~100 cells each) were processed as shown in Fig. 1. Expression data is normalized by row to show differences between each patient. Patients 1, 2, and 5 showed similar protein profiles. This partially concurred with genotyping as both patients 1 and 2 had EGFR exon 19 amplification and T790m mutations. Patient 5 shows a similar profile but had a KRAS mutation. This suggests that different genotypes may result in similar proteomic phenotypes and is consistent with the observation that both EGFR T790M and KRAS mutations are known markers for resistance to EGFR inhibitor therapy (191,192). Patients 3, 4, and 6 all had distinct proteomic profiles, and all had differing mutations. Patient 3 had an exon 20 EGFR mutation, and patient 4 had an EGFR L858R mutation and an additional BRAF mutation. Patient 6 was noted to have an EML4-ALK translocation. Protein clustering also reveals interesting personalized targets. For example, Patient 4 (EGFR/BRAF mutant) had high pERK1/2 and pS6RP as expected; however, this patient also showed a high level of PARP, Ku80 and pH2A.x, which are markers for DNA repair/damage. This suggests that PARP inhibitors or DNA damaging agents (cisplatin) could be effective in this patient. 138

Figure 5-11. Effect of different therapies on protein expression profiles in the triple negative breast cancer cell line MDA-MB-436. MDA-MB-436 cells were treated with different agents and marker proteins were measured. Treatment response markers for each group identified inhibition of expected proteins (p-mTOR, pS6RP, pERK for targeted treatments; pH2A.X, pATM/ATR substrate for DNA damaging agents). Furthermore, unsupervised hierarchical clustering based on euclidean distance (MATLAB) grouped drug treatments by their mechanisms of action (molecularly targeted vs. DNA-damaging) and primary targets (EGFR for Gefitinib/Cetuximab vs. mTOR/PI3K for PKI-587).....139

Figure 5-12. Screen for treatment response in triple negative breast cancer cell line (MDA MB 436; BRCA1-/-). Heat Map shows fold changes of markers grouped into various categories. Drugs cluster depending on mechanism of action. 140

Figure 5-13. Monitoring and predicting treatment response in patients receiving PI3K inhibitors. (A) Four patients with biopsy-proven adenocarcinoma were treated with PI3K inhibitors, and primary cancers were biopsied before and after treatment. The heat map is a pre-post treatment difference map showing log2 fold changes in protein expression (normalized by row to highlight differences between patients). Patients segregate into two clusters (correlation distance metric; weighted linkage): tumors that responded and tumors that progressed. The patient in the third column received a higher dose of the PI3K inhibitor (400 mg bid as opposed to 150 mg bid) and showed greater up-regulation and down-regulation across the marker panel. (B) Profiles of five drug-naive lung cancer patients are shown with clustering based on correlation metrics with weighted linkage. The patients group into responders and non-responders. A marker ranking algorithm identifies H3K79me2 as the top differential marker between responders and non-responders. The dotted box shows that this marker clusters with proteins across many protein networks including pS6RP (a downstream target of PI3K), pH2A.X (DNA damage marker), PARP (DNA repair protein) and 4EBP1 (protein translation). The predictions correlated with subsequent clinical observation.....142

List of Tables

Table 1-1 summarizes some of the current clinical needs in the cancer field. 22

Table 3-1. Clinical information for 70 patients with suspected abdominal malignancies. 65

Table 3-2. The sensitivity, specificity and accuracy of different markers (single or in combination). 71

Table 3-3. Verification of the diagnostic value for the four-panel markers in an independent test set of 20 patients. 72

Table 3-4. Verification of the diagnostic value for the four-panel markers in an independent test set of 20 patients. 73

Table 4-1. Characteristics of ovarian cancer patients (n=46). 86

Table 4-2. Sample numbers of different data sets. 87

Table 4-3. Sensitivity, specificity, and accuracy of different protein markers in the training set 101

Table 4-4. Sensitivity, specificity, and accuracy of different protein markers. 104

Table 5-1. **Significant markers between A431 +/- gefitinib (single cells).** This displays all markers that showed significant difference between gefitinib-treated vs. untreated A431 single cells and the average expression values as calculated via Nanostring Profiling for each cohort. Markers were determined by pairwise t-testing and corrected for multiple testing errors by using a false discovery rate of 0.2. 132

Chapter 1

Introduction

1.1 Thesis Organization

My thesis is divided into six chapters which examine three novel platforms for diagnosing cancers, measuring treatment response, and examining intratumoral and interpatient hetoregeneity in clinical settings. These platforms exploit three different technologies; 1) diagnostic magnetic resonance (DMR), 2) microfluidics and 3) DNA barcoding developed for robust proteomic analyses of cancer cells within scant clinical samples. DMR and microfluidics highlight point-of-care applications while DNA barcoding enables high multiplexing.

Chapter 1 includes a literature review of existing needs for sensitive, multiplexed, and point-of-care protein analyses in oncology with a focus on specimen-limited goals. It also provides background on the above mentioned technologies leveraged in this thesis project. **Chapter 2** details the optimization of the DMR assay while **Chapter 3** discusses implementation of DMR technology in the clinical setting to analyze fine needle aspirates (FNAs) from 60 patients. **Chapter 4** focuses on the molecular profiling of ascites tumor cells (ATCs) from ovarian cancer patients (n=46). A diagnostic panel was identified and then leveraged using an inexpensive point-of-care microfluidic chip customized for detecting ATCs. **Chapter 5** elaborates on a novel proteomic assay using antibodies conjugated to unique DNA barcodes for high multiplex measurements (>100) of protein markers. This assay uses the commercially available

NanoString technology as a readout for the unique DNA barcodes. We demonstrate the assay's high sensitivity and potential for measuring intratumoral and interpatient heterogeniety in clinical settings. Then we extend its analytical reach by evaluating treatment response in patients. Finally, the thesis ends with **Chapter 6** comprising conclusions, impact of my work, and recommendations for future studies.

1.2 Clinical needs in cancer field

1.2.1 Protein expression patterns in cancer

Due to the highly adaptive and heterogenous nature of cancer cells (1,2), it has become clear the importance of molecular profiling to classify cancers, stratify patients for molecular targeted therapies and to assess treatment efficacy (3). An expanded proteomic knowledge of clinically harvested cancer cells will potentially provide new information about tumor biology (4). An increasing number of biopsy-driven cancer trials rely on data from either: 1) genomic analyses revealing driver oncogenes and specific mutations (5) or 2) a limited number of hand-picked protein biomarkers intended to serially monitor cellular responses (6,7). Currently, there are many technologies available for high multiplexed analysis of DNA and mRNA. However, there still remains a large unmet need for proteomic tools with similar multiplexing capabilities. Moreover, mRNA levels do not always correlate with protein content (8,9) and the amount of protein produced for a given amount of mRNA depends on the current physiological state of the cell. An mRNA produced in abundance can be degraded rapidly or tranlsated inefficiently. Also, many proteins are subjected to various chemical modifications after translation. These post translational modifications (PTMs) such as phosphorylation, ubiquitination, methylation, and acetylation are critical to protein

function and profoundly influence their activities. Variable protein levels and PTMs within tumors can directly affect drug pharmacodynamics, including the extent to which drugs engage their targets, trigger alternative molecular pathways, and induce tumor cell death or resistance (10). Despite appreciation for the biological relevance of variable protein levels, tools to profile the landscape of key protein networks in clinical samples are lacking.

1.2.2 Clinical sources of cancer cells

It can be expected that soon, clinical trials will incorporate collection of tumor samples at key treatment nodes; before therapy, during therapy, and at relapse. Since repeat surgical resection is impractical and potentially risky, focus has shifted towards samples, such as fine needle aspirates (FNAs) and ascites, which can be obtained less invasively and serially (**Figure 1-1**). Molecular profiling of these cancer cells can be useful for diagnosis, prognosis, or early readouts of treatment response, drug resistance, disease progression, and/or disease recurrence (11). It holds promise for improving treatment success and reducing toxicity (12). A paradigm shift is needed so that each cancer patient is offered a personalized treatment plan for their unique molecular signature (13).

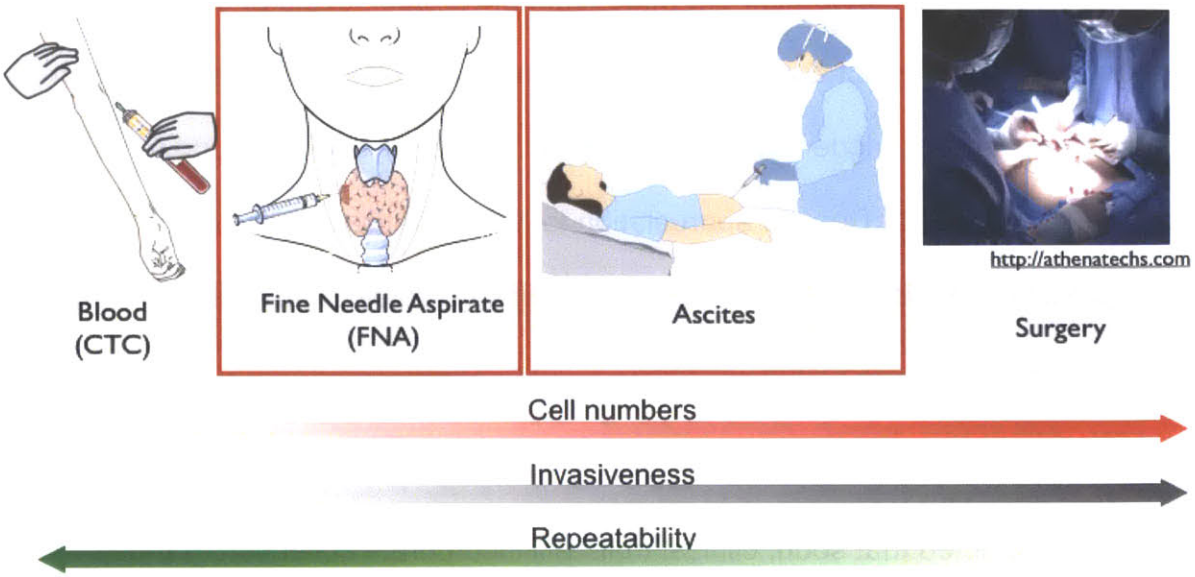

Figure 1- 1. Potential sources of cancer cells in clinical samples; circulating tumor cells (CTCs), fine needle aspirates (FNA), ascites, and surgery. The main focus of this thesis is on fine needle aspirates (Chapter 3 and Chapter 5) and ascites (Chapter 4) samples. From left to right the typical number of cancer cells obtained from these samples increase. However, the invasiveness of the procedure also increases while the repeatability decreases. Exceptions to this trend are the similar repeatability and invasiveness features between ascites and FNA's.

1.2.3 Treatment response

Currently, efficacy or failure of standard therapies is typically determined during or at the end of treatment. This results in many unnecessary drug side effects often without clear medical benefit. Thus, methods that predict treatment efficacy prior to administration are needed (14). Molecular profiling of specific biomarkers can help identify biological subsets of cancers with activated or deregulated pathways conferring predictive biomarkers of treatment response. As a result, the appropriate patients could be treated with the appropriate targeted therapy tailored to their unique molecular profile.

Although it is expected that cytotoxic chemotherapies will continue to anchor many cancer treatment plans, the expanding arsenal of molecular targeted agents is poised to improve treatment response and prolong disease remission. Currently, there

are a number of small-molecule inhibitors and monoclonal antibodies in clinical trials and on the market that target different critical cancer pathways (2,15,16). With sufficient molecular information, informed decisions regarding which patients to enroll in a clinical trial and what drug combinations to use can be made.

Based on molecular profiling data, patients harboring abnormalities in specific pathways can also be treated with targeted therapies to minimize toxicity. For example, if patient's cancer cells have upregulated Ras-Raf-MEK-MAPK pathway activity, MEK inhibitors such as Selumetinib (15,17) become viable options; whereas patients with PI3K pathway deregulation can be treated with a PI3K, Akt, or mTOR inhibitor such as PKI-587 (18), MK-2206 (19), or Rapamycin (20), respectively. Poly (ADP-ribose) polymerase (PARP) inhibitors (21) can be leveraged in BRCA mutation carriers to cause cell death due to unrepaired DNA single stranded breaks, accumulation of double stranded breaks, and collapsed replication forks. EGFR is a receptor tyrosine kinase that is commonly overexpressed in cancers and targeted with gefitinib, erlotinib, or cetuximab (22-24). The overexpression of ERBB2 has also been observed in breast and ovarian cancer patients and treated with trastuzumab or pertuzumab (25). Recent experience dictates high levels of eventual resistance. As such, identifying ideal combination strategies using actionable predictive and pharmacodynamic biomarkers to render clinical benefit is of paramount importance (26). Achieving success here would confer a paradigm shift in our approach to treating cancer.

1.2.4 Technological needs

Highly sensitive and quantitative technologies able to detect and molecularly profile cancer cells in clinical samples in a manner superior to current clinical methods

(e.g. cytology or histology) are in demand. Many conventional clinical technologies are time-consuming, expensive, or require considerable sample sizes. Clinical samples are typically limited in cell number and require multiple molecular markers to help clinicians render accurate prognoses, diagnoses, or treatment plan decisions. Technologies with fast, sensitive, and multiplex measurements are needed to help monitor disease (**Table 1-1**). Furthermore, low cost, high-throughput, and portable platforms assembled using standard microfabrication technology could foster transformative advances. This chapter will next provide background on the three technologies driving this thesis work; 1) DMR, 2) microfluidic, and 3) DNA barcoding.

Table 1-1 summarizes some of the current clinical needs in the cancer field.

CURRENT CLINICAL NEEDS
• Tools for early diagnosis and prognosis
• Tools for rapid detection in biological specimens with limited number of cancer cells (blood, FNA, ascites, etc.)
• Tools for multiplexed profiling of signaling networks including post translational modifications (phosphorylation, acetylation, methylation, etc.)
• Tools to objectively measure treatment response or resistance
• Tools to monitor relapse (malignancy progression, metastases, etc.)

1.3 Diagnostic Magnetic Resonance (DMR) Technology

Compared to other analytical techniques, magnetic detection enables measurements in turbid biological samples with minimal preparation steps (27). Light-based assay methods such as bioluminescence, absorption, colorimetry, or

fluorescence (used in flow cytometry) are sensitive to materials in the sample that scatter light, absorb light or fluoresce. Diagnostic magnetic resonance (DMR) technology lacks this problem because it employs magnetic fields to generate and detect signal. Since magnetic fields can pass through biological samples regardless of their optical properties, assays can be performed in diverse media, including whole blood and culture media (27). Standard techniques, such as Western blots, require relatively large sample sizes and often are time consuming due to the multiple processing steps involved (e.g. cell lysis, protein denaturation, and protein separation via gel electrophoresis). These techniques are not feasible when analyzing certain heterogeneous biological samples such as FNA, ascites, or blood that contain very limited number of cancer cells (<1,000). The high detection sensitivity of DMR enables detection even in small sample sizes. The platform is also versatile and scalable to accommodate additional biomarkers of interest, it offers robust portable operation, and is relatively inexpensive compared to conventional histopathology, all key attributes for emerging nanotechnology-based diagnostics.

1.3.1 DMR Device

In the past, NMR measurements have been performed using clinical MRI scanners or benchtop relaxometers operating at NMR frequencies of 100 kHz-50 MHz (28,29). Benchtop systems are equipped with permanent, low field (<1 T) magnets for field generation, which simplifies operation and equipment housing. However, the main drawback is the large sample volume needed. The DMR system was developed to overcome this limitation and has the distinct capability to perform measurements on smaller sample volumes.

The schematic diagram below (**Figure1-2**) shows the different parts of the DMR system used for NMR detection. With the miniaturized NMR probe and microcoil, the requirement for spatial homogeneity of magnetic fields becomes less critical. A small portable magnet can be used to generate the magnetic field, and sample volumes are significantly reduced (~10 µl). Thus, the DMR platform can be packaged as a portable handheld unit for point-of-care operations (27). An early prototype system, including NMR probes, RF generators, and power, weighed only 3 kg yet was over 60 times more sensitive than conventional NMR (27).

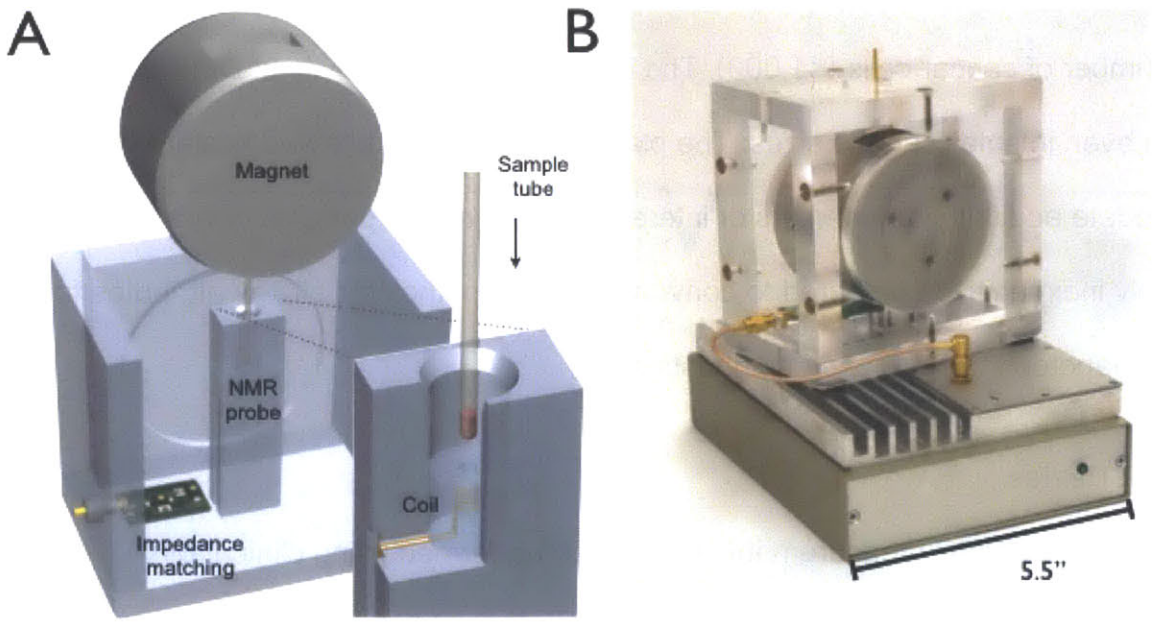

Figure 1-2. DMR system. (A) The schematic of the DMR system consists of a miniaturized microcoil for NMR measurements, embedded NMR electronics, and a permanent magnet for polarizing magnetic field generation. The microcoil generates RF magnetic fields to excite samples and receives the resulting NMR signal. The NMR electronics are designed to perform T_1 and T_2 measurements via inversion-recovery and CPMG pulse sequences, respectively. (B) The complete DMR-3 system for near-patient use. The bottom component contains all the electronic circuitry for NMR measurements while the top enclosure holds a permanent magnet and chip-sized, µL-volume sensors.

Monolithic integration of all NMR electronics in a CMOS IC chip has enabled the development of the smallest functional NMR system to date (27). Due to system

miniaturization, the detector needed to be designed to overcome two key challenges. The first issue was low signal levels due to the small sample size. The second issue was fast signal decay due to field inhomogeneity from the small, portable magnet. These two problems were solved by implementing a low noise RF amplifier with high voltage gain and development of an on-chip digital pulse generator for CPMG sequences.

Improvements have been made to the DMR platform over the past few years of development. The latest DMR-3 has additional advanced features compared to previous prototypes such as DMR-1 (27) and DMR-2 (30) including: a) a disposable, thin-walled sample container, which tightly slides into the coils and b) custom designed and easy to use NMR hardware which automatically tunes measurement settings (NMR frequency, pulse width, and power) to compensate for environmental factors such as temperature fluctuations.

1.3.2 Magnetic nanoparticles

Many various properties of magnetic nanoparticles (MNP) can be optimized for use in DMR technology. One key property is relaxivity, r_2, which can have a significant impact on the detection sensitivity of DMR. MNP with higher relaxivities induce larger changes in R_2. This can be achieved by increasing the size of the magnetic core of the MNP (30). However, MNP need to remain small enough so that they can still bind to cell surface markers and permeate into cells for intracellular targeting (31). Smaller MNP also tend to stay in solution and exhibit superparamagnetic behavior so that spontaneous magnetic aggregation does not occur (32,33). In addition, it is important that the MNP be hydrophilic and biocompatible so that they do not induce change in the

expression profiles of cells (34). Most commercially available MNP are not well suited for DMR assays because of their large size and low relaxivity. Custom synthesized 40 nm cross-linked iron oxide (CLIO) nanoparticles have been used in our lab due to their excellent biological properties and ease of antibody modifications.

1.3.3 Cellular Magnetic labeling

The DMR sensor consists of a miniaturized NMR probe that measures the transverse relaxation rate (R_2) of water molecules in specific biological samples in which cell biomarkers are labeled with magnetic nanoparticles (30). The presence of bound or clustered magnetic nanoparticles attached to the intended molecular target on the cell leads to a corresponding decrease in the bulk spin-spin relaxation time (T_2) or an increase in the spin-spin relaxation rate ($R_2=1/T_2$) of surrounding water molecules (**Figure 1-3**). The DMR sensor measures the relaxation rate, R_2, of water protons in samples, and can be used for detecting and profiling cancer cells (30).

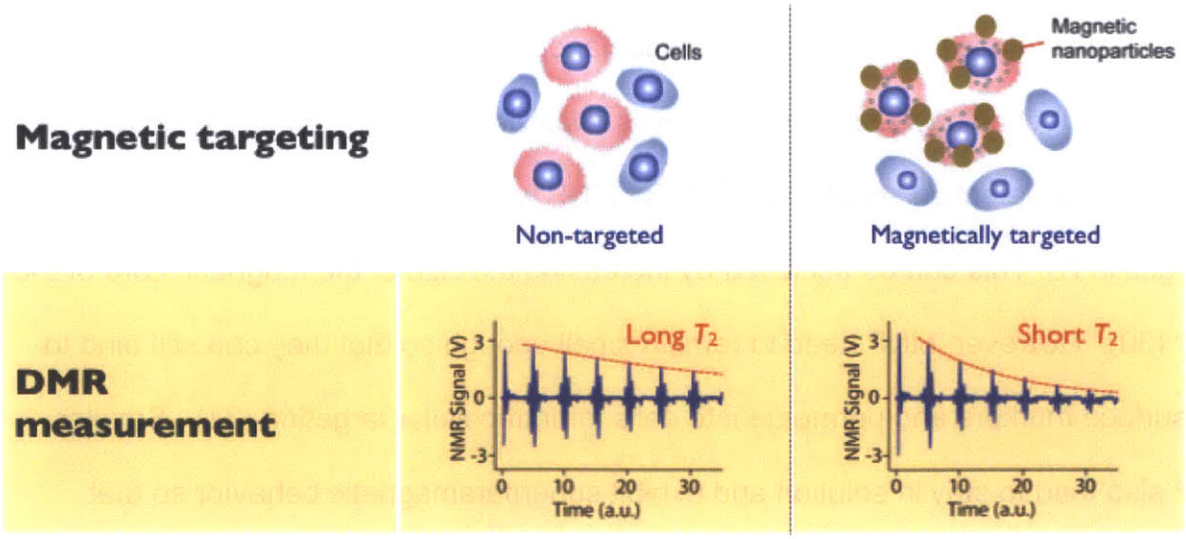

Figure 1-3. Principle of magnetic targeting assay. Cells can be targeted with magnetic particles to alter the magnetic properties of surrounding water molecules. Magnetic nanoparticles cluster upon binding to targets which decrease the spin-spin relaxation time (T_2) of surrounding water protons. DMR measurements are shown in the bottom graphs where T_2 decreases when MNP clusters are present.

1.3.4 NMR theory

The nuclei of hydrogen atoms in water molecules have a magnetic moment that align with the magnetic field produced by an external magnet (along the z-axis; **Figure 1-4 A**). An alternating current is then passed through the microcoil in the DMR device which creates a temporary magnetic field that is perpendicular to that of the permanent magnet. This causes the magnetic moments of the hydrogen nuclei to rotate into the xy plane where they initially start off spinning in phase with each other (**Figure 1-4 B**). Over time they start to spin at different speeds and become dephased. The magnetic field in the xy plane, M_{xy}, originally starts off having a high amplitude because the magnetic moments of the hydrogen nuclei are in phase with each other. However, M_{xy} decreases over time as the individual magnetic moments of each hydrogen nuclei become out of phase (**Figure 1-4 C**). This change in magnetic field induces an electrical current in the microcoil which is then detected and converted into a voltage measurement in the electronics of the DMR device. The decrease in voltage over time is then fitted to an exponential decay curve to determine the relaxation time, T_2 (**Figure 1-4 D**). When there are magnetic nanoparticles present, the magnetic moments of the hydrogen nuclei in the water molecules lose their coherence faster resulting in a decrease in T_2 or an increase in the relaxation rate R_2 ($1/T_2$).

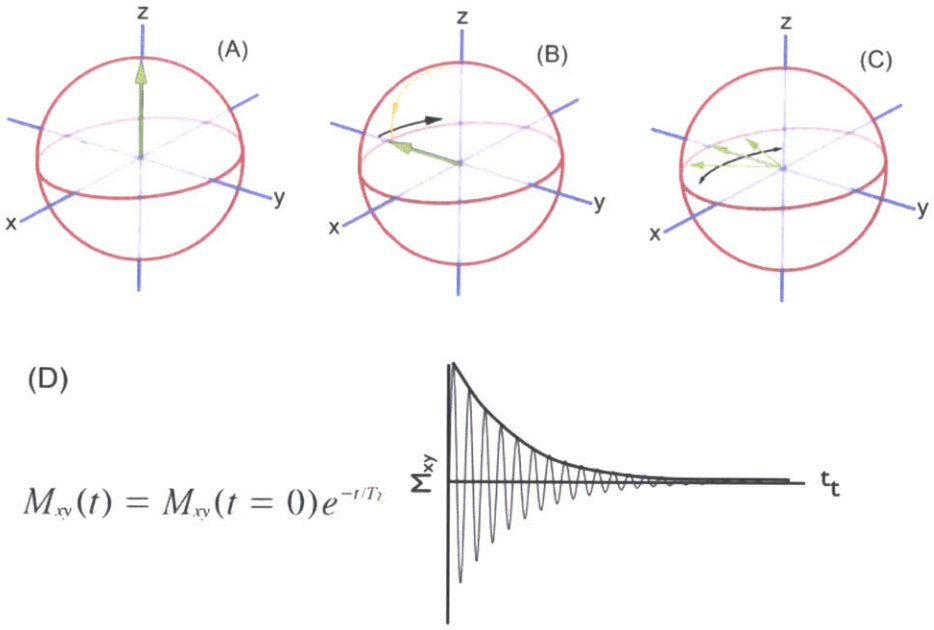

Figure 1-4. Schematic of perturbation of hydrogen nuclei magnetic moments. (A) The magnetic moments of the hydrogen nuclei in water molecules originally start off aligned in the permanent magnetic field of the DMR device in the z-direction. (B) Then the magnetic moments are pushed into the xy plane when an alternating current is passed through the microcoil of the device. (C) The magentic moments eventually become out of phase with each other. (D) The decrease in the magnetic field in the xy plane (M_{xy}) over time is fitted to an exponential decay curve to determine the relaxation time, T_2. (35)

1.4 Microfluidic technology

The field of microtechnology is beginning to revolutionize biological analysis and create new ways of analyzing and manipulating bio-samples such as cells *in vitro*. The size scale (nanometers to micrometers) is well matched to the physical dimensions of biological samples (cells, extracellular vesicles, etc.) and is advantageous in that only tiny volumes of reagents are needed (36). In addition, portable microdevices can be easily scaled-up for high-throughput analysis in point-of-care settings. For these aforementioned reasons, it is not surprising that recent microfluidic systems with embedded physical microstructures on the micro or nanoscale have attracted significant attention.

Soft lithography first introduced by G.M. Whitesides *et al* (37-39) consists of a set of techniques that are particularly well suited for generating microscale or nanoscale structures in soft materials. It has proven useful in providing microfluidic devices for a wide range of applications such as label-free methods for the separation and enrichment of cancer cells from complex heterogeneous bodily fluids (40,41). It is envisioned that soft lithography will continuously find use in integrated microfluidic systems due to its simple, cheap, and quick route toward micro/nanofabrication.

Soft lithography includes techniques that can create soft polymeric molds such as polydimethylsiloxane (PDMS) replicas from an original hard master. The master is typically fabricated by conventional photolithography (36) to transfer a pattern envisioned by the designer onto a material such as silicon (**Figure 1-5 A**). A photoresist layer is added to the the silicon wafer by spin-coating (**Figure 1-5 B**). The pattern can be drawn with a computer-assisted design (CAD) program and then transferred onto a photomask. The photomask is typically a glass plate that has on its surface an opaque material (*e.g.* chrome) in the desired pattern. The mask is then placed on top of the photoresist layer (**Figure 1-5 C**). UV light is shone through the mask and onto the photoresist. The photoresist portions that are exposed to the UV light become crosslinked, causing them to be insoluble in a developing solution. This is known as a negative photoresist (positive photoresist gives the inverse pattern). The wafer and mask are then separated, and the photoresist portions that were not exposed to UV light (not crosslinked) can be removed using a developing solution such as an organic solvent (**Figure 1-5 D**). The silicon wafer now contains a photoresist microstructure pattern that can be used as a master for soft lithographic methods. The pattern can be

transferred rapidly and inexpensively to a PDMS layer with a simple procedure consisting of pouring the PDMS onto the master, curing at 65°C, and then peeling the PDMS layer away (**Figure 1-5 E,F**).

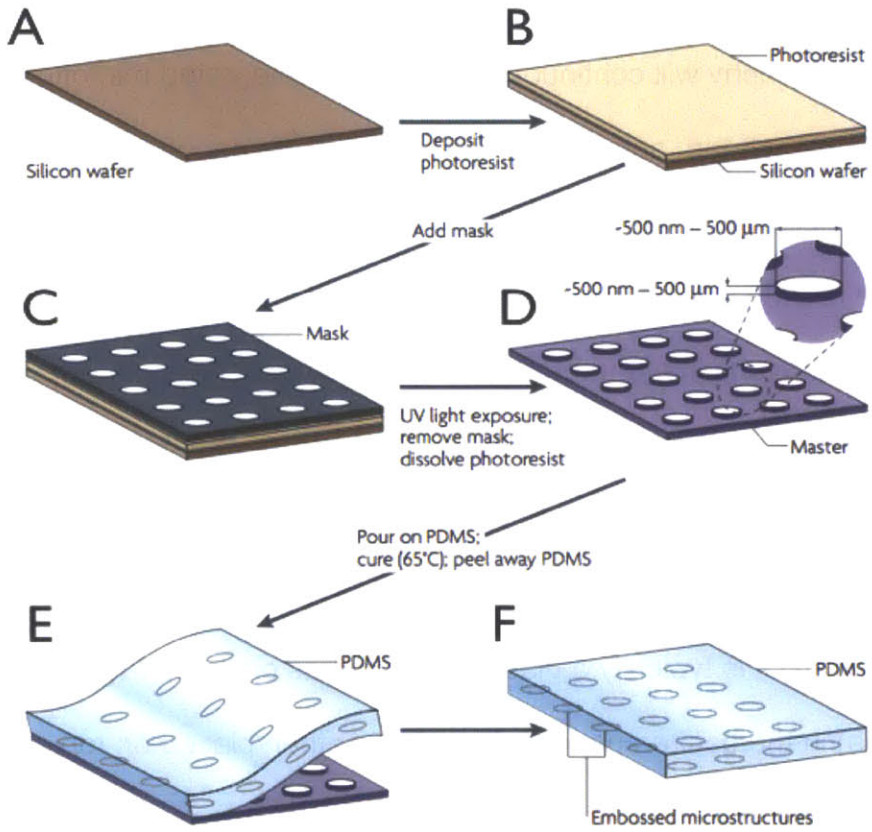

Figure 1-5. The fabrication of micropatterns using soft lithographic techniques. (A-B) A silicon wafer is spin-coated with photoresist. (C) A mask is placed on the photoresist layer. (D) The photoresist layer is then crosslinked by exposure to ultraviolet (UV) light. Then an organic solvent is used to dissolve the photoresist that is hidden under the mask and not crosslinked. This results in a master mold consisting of a silicon wafer with a pattern made of photoresist. (E) Then poly(dimethylsiloxane) (PDMS) is poured on the master, cured, and peeled away. (F) The final product is a PDMS layer consisting of micropatterns that can range in size from nanometer to micrometers. (42)

1.5 DNA barcoding Technology

DNA barcoding (e.g. NanoString) technolgy was originally developed for high-throughput RNA expression profiling with a direct digital readout. It has high sensitivity (0.5 femtomolar) and requries only a small amount of total RNA starting material with no

amplification needed (43). It is an extremely fast and easy assay to set up requiring only 15 minutes of hands-on time. The assay involves capture probes and reporter probes designed with complementary base pairs to the mRNA targets of interest. The capture probe contains three components: 1) a complementary sequence to the mRNA target, 2) a repeated sequence at the 3' end, and 3) a biotin group at the end of the 3' repeat section (**Figure 1-6 A**). The reporter probe also consists of three main parts: 1) a complementary sequence to the mRNA target of interest, 2) a repeated sequence at the 5' end, and 3) a fluorescent barcode composed of different combinations of four spectrally non-overlapping dyes (**Figure 1-6 A**). The four different dyes are arranged over seven regions allowing for a total of 4^7 or 16,384 possible unique barcodes (43). A single strand of M13 bacteriophage DNA is used as the backbone of the barcode section of the reporter probe (44). Fluorescently tagged 900 nucleotide sequences of RNA that are complementary to the seven different regions of the backbone are preannealed to the backbone (43). This results in the spacing and length of each region creating a unique seven spot fluorescent pattern that the digital analyzer can detect (**Figure 1-6 C**).

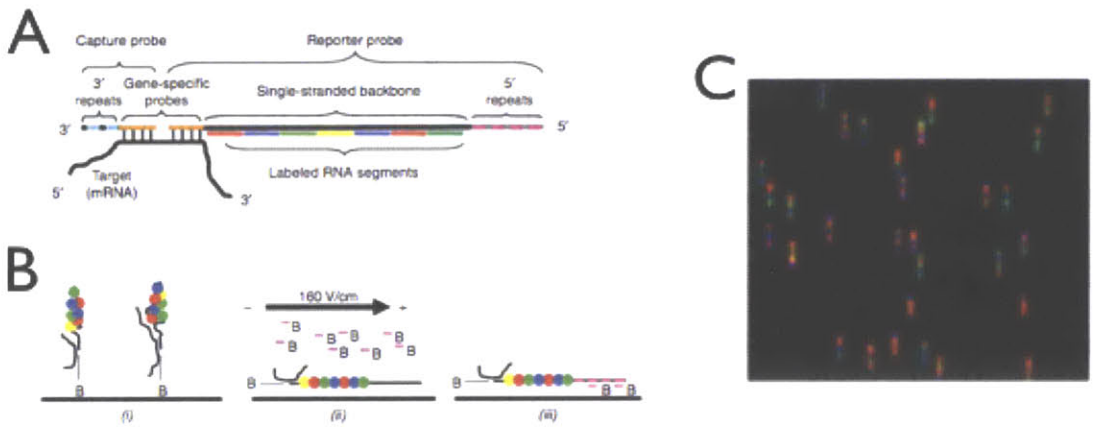

Figure 1-6. (A) Schematic representation of the capture probe and the reporter probes bound to the target mRNA molecule. (B) (i)The target-probe complex is captured to the streptavidin coated surface via the biotin at the end of the capture probe. (ii) Then biotinylated complementary sequences to the 5' repeat section of the reporter probe are added and (iii) a voltage is applied so that the target-probe complex lays flat on the surface of the cartirdge. (C) Then the analyzer takes an image of the surface and counts the number of unique reporter probes present. (43)

Initially, the capture probe, the reporter probe, and the mRNA are added together and hybridized overnight at 65°C (**Figure 1-7 A,B**). The sample is then placed on the automated prep station (~2 hrs) which removes the excess reporter and capture probes from the target-probe complex using two sequential purification steps (**Figure 1-7 C**). First, magnetic particles with complementary sequences to the 3' repeat section of the capture probe are used to capture the target-probe complex and wash away excess reporter probe. In the second purification step, magnetic particles with complementary sequences to the 5' repeat section of the reporter probe are used to capture the target-probe complex and remove excess capture probe. In the final step, the target-probe complex is bound to the streptavidin coated surface of the NanoString cartridge via the biotinylated 3' end of the capture probe. Biotinylated complementary sequences to the 5' repeat section of the reporter probe are then added to the cartridge and a voltage is

applied so that the bound target-probe complex lies flat on the surface (**Figure 1-6 B, Figure 1-7 D**). Then the cartridge is moved from the prep station to the digital analyzer where images are obtained and the number of unique fluorescently labeled barcodes are counted (**Figure 1-7 E**). This step takes typically 4 hrs, but again there is no hands on time required and up to six cartridges can be placed on the analyzer at one time and run overnight. Each cartridge contains 12 spots for samples enabling up to 72 samples to be run per day for high throughput screening. Chapter 5 will discuss how we developed a novel highly sensitive proteomic assay for multiplex measurement of > 100 markers in samples with limited number of cells (1-50 cells) using this technology as the final readout.

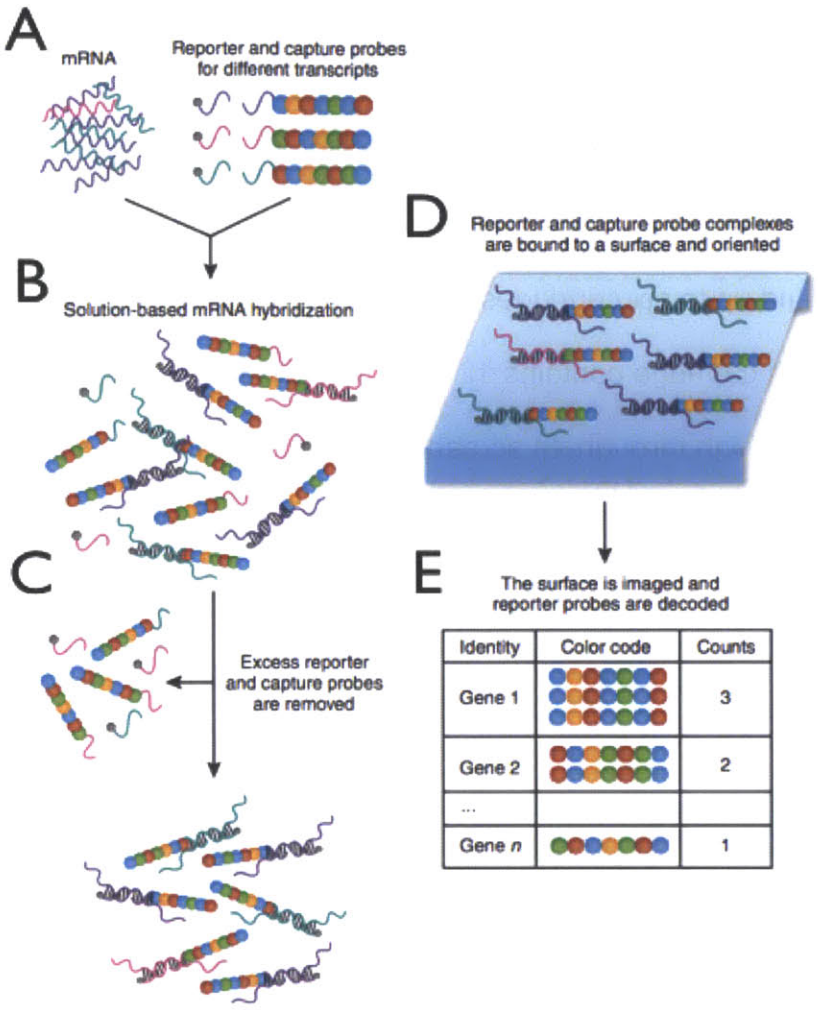

Figure 1-7. Overview of the NanoString's digital profiling technology for mRNA (A) NanoString's Technolog uses two probes, a reporter probe and a capture probe. The capture probe allows the target-probe complex to be immobilized for data colection and the reporter probe contains the flourescent barcode signal. (B) The reporter and capture probe hybridize with the target mRNA in solution (C) After the hybridization step, the excess probes are removed and (D) the target-probe complex is immoblized on the nCounter cartridge using the Prep station. (E) The surface is imaged and the barcodes are then counted and tabulated for each target molecule usng the Digital analyzer. (44)

Chapter 2

Optimized Diagnostic Magnetic Resonance (DMR) Assay

Parts of this chapter have been published in:
Peterson, V., Castro, C., Lee, H., Weissleder, R. Orthogonal Amplification of Nanoparticles for Improved Diagnostic Sensing. ACS Nano, 6(4), 3506-3513, 2012.

Abstract

There remains an ongoing need for fast, highly sensitive, and quantitative technologies that can detect and profile rare cells in freshly harvested samples. Recent developments in nanomaterial-based detection platforms provide advantages over traditional approaches in terms of signal sensitivity, stability, and the possibility for performing multiplexed measurements. Here, we describe a bioorthogonal, nanoparticle amplification technique capable of rapid augmentation of detection sensitivities by up to 1-2 orders of magnitude over current methods. This improvement in sensitivity was achieved by i) significantly reducing background noise arising from non-specific nanoparticle binding, ii) increasing nanomaterial binding through orthogonal rounds of amplification, and iii) implementing a cleavage step to improve assay robustness. The developed method allowed sensitive detection and molecular profiling of scant tumor cells directly in unpurified human clinical samples such as ascites. With its high sensitivity and simplified assay steps, this technique will likely have broad utility in nanomaterial-based diagnostics.

2.1 Introduction

Nanoparticles (NPs) of different sizes, shapes and compositions have been increasingly employed for *in vitro* diagnostics (45,46). NP-based sensing technologies are often more sensitive than small molecule sensors, due to their multivalency, (47), exploitation of novel physical effects (48,49) simplified purification and analysis, and because assays can be multiplexed. Recently, enormous progress has been made in developing NPs with unique optical or magnetic signatures. For example, advanced gold/silver clusters (45,50) and newer doped ferrites with high magnetization can detect analytes within the femtomolar (fM) range(51,52). However, there is still a gap between current detection limits and the abundance of biological targets, which requires either purification and concentration, or amplification. This is especially the case in clinical diagnostic settings, such as cancer (53,54) or infectious diseases (55-57), where detection of rare targets (e.g, cells or bacteria) in clinical samples is necessary.

A variety of amplification methods have been previously described; these include two-step methods (avidin-biotin, click chemistry (58,59)), DNA-templated amplification (60) and supramolecular host chemistry (61). Based on newer cycloaddition chemistries for rapid conjugation, we hypothesized that multiple steps of alternating orthogonal chemistries could be used as an alternative amplification method with higher sensitivity. Of particular interest are {4+2} cycloaddition reactions, which are extremely fast and selective, and for which a number of orthogonal reaction partners have already been described (62,63). Unlike DNA methods, these cycloadditions do not require sample heating (annealing) nor do they require sensitive polymerases or catalysts. Here, we describe the systematic exploration of one such method. Specifically, we investigated

the effect of repeated rounds of orthogonal NP labeling on amplification (signal over noise), and the implementation of an additional cleavage modification that would confer synergistic improvements to the assay's performance. We show that this optimized labeling method significantly improves detection sensitivities of nuclear magnetic resonance (NMR)-based sensing (diagnostic magnetic resonance, DMR). Unlike conventional methods such as flow cytometry, whose uses are often limited due to time-consuming sample-purification and accompanying cell loss, this new labeling strategy allowed cancer cells to be detected and molecularly profiled in unpurified clinical samples. We expect that this new technique will have broad applications in future nanomaterial-based diagnostics.

2.2 Materials and Methods

2.2.1 Preparation of cleavable pegylated Tz and TCO nanoparticles (NPs)

Magnetofluorescent nanoparticles (MFNP) were synthesized by reacting cross-linked iron oxide (CLIO) NPs with amine reactive cyanine dyes (VT-680xl, Perkin Elmer), as previously described (58). The amino-MFNP contained approximately 62 primary amine groups and ~7 VT-680 molecules conjugated to the surface. The hydrodynamic diameter was 27 nm, as determined by dynamic light scattering (Zetasizer 1000HS; Malvern Instruments), and the r_1 and r_2 relaxivities were 26.3 and 52.3 mM^{-1} s^{-1}, respectively, at 40°C and 0.47 T (Minispec MQ20; Bruker). MFNP molar concentration was determined based on an estimated molecular mass of 447,000 daltons (8000 Fe atoms per core crystal, 55.85 daltons per Fe atom (64,65)).

MFNPs with a polyethylene glycol (PEG) spacer between the particle and the

orthogonal reactant were prepared in a three step process. First, the MFNPs were reacted with 2000 molar equivalents (relative to the MFNPs) of sulfosuccinimidyl 6-{3´ (2-pyridyldithio)-propionamido} hexanoate (sulfo- LC-SPDP, Thermo Scientific) in phosphate buffered saline (PBS) for 1.5 hours at room temperature. Excess sulfo-LC-SPDP was removed using a 100 kD ultracentrifugation unit (Amicon), and washed three times with PBS at 1800 rcf for 15 minutes. In the second step, 2000 molar equivalents of thiol-PEG-amine (3.4 kDA, Creative Pegworks) relative to the MFNPs, were reacted in PBS and aged overnight at 4°C on a shaker. Excess thiol-PEG-amine was removed using a 100 kDa ultracentrifugation unit (Amicon), and washed three times with PBS at 1800 rcf for 15 minutes. In the third step, amine-PEG terminated MFNPs were modified with either 2,5-dioxo-pyrrolidin-1-yl 5-(4-(1,2,4,5-tetrazin-3-yl)benzylamino)-5-oxo-pentanoate (Tz-NHS) or (E)-Cyclooct-4-enyl 2,5-dioxopyrro-lidin-1-yl carbonate (trans-cyclooctene N-hydroxy-succinimidyl ester; TCO-NHS), synthesized as previously reported (66). This reaction was performed using 250 molar equivalents of Tz-NHS or 2000 molar equivalents of TCO-NHS (relative to the MFNPs), and proceeded in PBS containing 10% dimethylformamide (DMF) and 10 mM of sodium bicarbonate at room temperature for 4 hours. Excess orthogonal reactant was first removed using a 100 kDA ultracentrifugation unit (Amicon), which concentrated the sample down to ~0.25 ml for the final purification step using gel filtration (Sephadex G-50, GE Healthcare). For MFNPs conjugated to Tz without the PEG spacer, the first two steps were omitted.

2.2.2 Preparation of TCO-modified antibodies

Monoclonal antibodies: trastuzumab (Genentech), Cetuximab (Bristo Myers Squibb), anti-EpCAM (clone 158206, R&D systems) and anti-MUC1 (clone M01102909, Fitzgerald Industries) were modified with TCO-NHS. If sodium azide was present, it was removed using a 2 ml Zeba desalting column (Thermo Fisher). The reaction was performed using 1000 molar equivalents of TCO-NHS and 0.5 mg of antibody in PBS containing 10% (v/v) DMF and 10 mM sodium bicarbonate for 4 hours at room temperature. Samples were then purified using Zeba columns and the antibody concentration was determined by absorbance measurement (NanoDrop 1000 Spectrophotometer, Thermo Scientific). On average, antibodies bore ~15 TCO molecules. The TCO-modified antibodies retained their affinity as previously confirmed (58). In addition, this conjugation can be further improved by directing the chemical modification to the F_C portion of antibody (*e.g.*, *via* oxidation of its glycosidic chains) (67).

2.2.3 Nanoparticle labeling

The human cancer cell lines SK-OV-3 and SK-BR-3 were obtained from ATCC and maintained in McCoy's 5A with 10% fetal bovine serum (FBS), 1% penicillin/ streptomycin, 3% sodium bicarbonate, and 1% L-glutamine. Prior to experiments, cells were grown to ~90% confluency, released using 0.05% trypsin/0.53 mM ethylenediaminetetraacetic acid (EDTA), and washed once with PBS containing 2% bovine serum albumin (PBS+). Cells were then fixed with Lyse/Fix buffer (BD Biosciences 558049) for 10 minutes at 37 °C and washed twice with PBS+. The fixed

cells were then either analyzed real-time or frozen down at -20°C for subsequent labeling. In the next step, cells were labeled with TCO modified monoclonal antibodies (10 µg ml-1) in 0.15 ml of PBS+ for 30 minutes at room temperature; antibodies were omitted in control samples. Cells were washed once with PBS to remove the excess antibody. For the initial labeling with MFNPs, cells were resuspended in 0.4 ml MFNP-PEG-Tz (40 µg Fe/ml) for 15 minutes at room temperature. The NP concentration was then determined by measuring the iron (Fe) content through absorbance, at a characteristic wavelength of 400 nm (NanoDrop 1000 Spectrophotometer, Thermo Scientific) and with a known standard for calibration. For the initial amplification (AMP1), cells were washed once and resuspended in 0.4 ml of 40 µg Fe/ml MFNP-PEG-TCO (15 minutes, room temperature). Likewise, cells from the AMP1 step were washed once and resuspended in 0.4 ml of 40 µg Fe/ml of MFNP-PEG-Tz (15 minutes, room temperature) for the second amplification (AMP2). After the last round of labeling, cells were washed once with PBS+ and this was followed by a final wash with PBS. For the cleaving step, samples were mixed with dithiothreitol (DTT; 100 mM) and kept at 37°C for 15 minutes. Finally, cells were centrifuged down and the supernatant (containing the MFNPs) was removed for magnetic resonance measurements. The cleaved MFNPs in DTT (AMP1-C) had a monodisperse mean diameter of ~100 nm (Malvern).

2.2.4 DMR measurements

Magnetic resonance measurements were performed using the miniature NMR system developed for point-of-care diagnostics (68). The miniaturized NMR device was used to measure the transverse relaxation rate on 1-2 µl sample volumes, using Carr-

Purcell-Meiboom-Gill pulse sequences with the following parameters: echo time, 3 ms; repetition time, 4 s; number of 180° pulses per scan, 900; number of scans, 7. A detection threshold of $\Delta T_2 \geq 2.5\%$ was used to rule out instrumental errors (68). All measurements were performed in triplicate, and the data are presented as the mean ± standard error of the mean. The measured T_2 values were then converted to ΔR_2^+, ($R_2 = 1/T_2$, $\Delta R_2^+ = R_2^{sig} - R_2^{\theta}$), where R_2^{sig} and R_2^{θ} are the transverse relaxation rates for targeted and control samples, respectively. For the same cell concentration the measured ΔR_2^+ value is proportional to the amount of MFNP loaded onto each cancer cell (30,60). A negative or zero signal signifies that there is no significant difference in DMR signal between biomarker labeled cells and non-specific binding of MNP to cells within the detection limit. To determine the absolute number of biomarkers, polymer microspheres (Bangs Laboratories) with a known amount of binding sites were used to create calibration curves to translate DMR levels to the number of biomarkers present.

2.2.5 Flow cytometry

At the conclusion of the MFNP amplification step, but before the cleavage step, samples were measured for VT-680 fluorescence using an LSRII flow cytometer (Becton Dickinson). Mean fluorescence intensity (MFI) was determined using FlowJo software to quantitate the amount of NP present. Two standard deviations above the non-labeled cell measurement was used as the lower limit of detection.

2.2.6 Microscopy

SK-BR-3 cells were magnetically labeled using the method described above. MFNPs with different fluorophores were employed: VT-680-MNP-PEG-Tz for labeling, FITC-MNP-PEG-TCO for AMP1, and RITC-MNP-PEG-Tz for AMP2. Samples were transferred to a 96-well plate at the end of labeling, and again after the cleavage step. Images were acquired at 20x with a DeltaVision screening system (Applied Precision Instruments) and images were analyzed using FIJI software (version 1.45).

2.2.7 Clinical samples

Human clinical ascites from pancreatic cancer was profiled. To compare the cleaving and non-cleaving methods, non-purified samples were divided and screened for EGFR, EpCAM, HER2, and MUC1. For each marker, both AMP1 and AMP1-C were employed as described above. Marker expression levels were determined based on the ratio of positive marker (ΔR_2^+) and control ($\Delta R_2^\theta = R_2^\theta - R_2^{PBS}$). Purified clinical samples were prepared through CD45 negative selection using CD45 magnetic beads and LS columns (Miltenyi Biotec). Both purified and non-purified samples were then targeted for MUC1, and their magnetic labeling was amplified *via* AMP1 and AMP1-C. Samples were analyzed using either DMR or flow cytometry, and the percent ratio of the non-purified signal to the purified signal was determined.

2.3 Results and Discussion

2.3.1 New labeling strategy for high detection sensitivity

Figure 2-1 summarizes the scheme of the developed labeling method. We hypothesized that the cellular loading of nanoagents, specifically magneto-fluorescent nanoparticles (MFNPs), could be maximized *via* the sequential application of MFNPs conjugated with orthogonal binding partners. Specifically, to form an initial MFNP layer, cellular targets were first labeled with antibodies modified with *trans*-cyclooctene (TCO) before being coupled with MFNPs derivatized with tetrazine (Tz) (58). This primary labeling can then be amplified through alternating applications of MFNP-TCO (Amplification 1; AMP1) and MFNP-Tz (AMP2) to form multiple MFNP layers. In addition to amplification, bound MFNPs could also be released from cells, collected and resuspended in buffer prior to performing analytical measurements. In so doing, it is theoretically possible to confer improved detection sensitivity and reliability by 1) eliminating biological contaminants (*e.g.*, cellular debris, components of extracellular matrix, non-targeted cells), and 2) reducing measurement artifacts caused by the sedimentation of labeled cells. In order to provide such functionality, the orthogonal reactants (TCO and Tz) were immobilized onto the MFNP surface through a cleavable linker (*e.g.*, disulfide bond; see Methods for details).

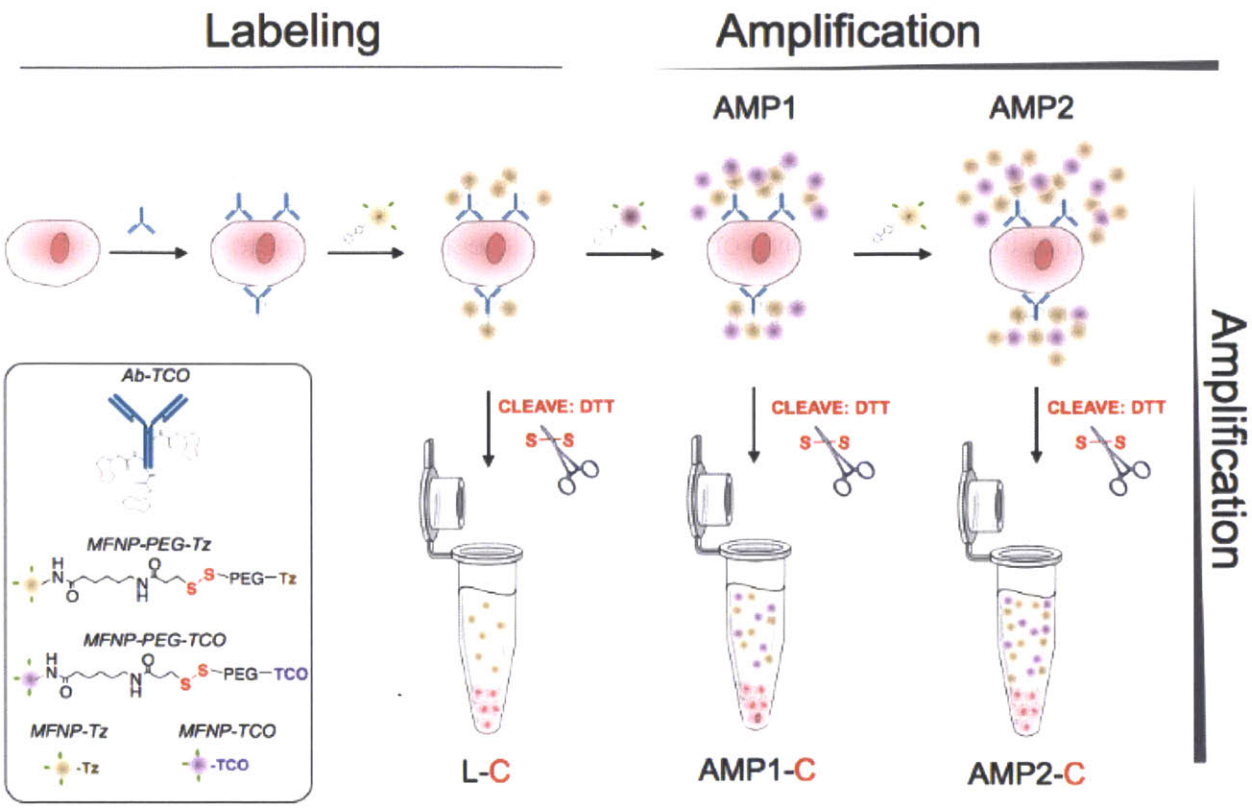

Figure 2-1. Schematic of the labeling strategy used to amplify biomarker signals
The labeling step (L) refers to the initial antibody-*trans*-cyclooctene (TCO) conjugate binding to the target followed by the addition of magneto-fluorescent nanoparticles (MFNPs) conjugated to the orthogonal reactant, tetrazine (Tz) . The signal can be subsequently amplified through additional rounds of complementary orthogonal MFNP conjugates (AMP1, AMP2) and through cleavage/purification using dithiothreitol (DTT; AMP1-C, AMP2-C).

Our first goal was to optimize both the NPs as well as the labeling protocols. Cancer cells (SK-OV-3, human ovarian carcinoma) overexpressing HER2 (human epidermal growth factor receptor 2; ~1×10^6 receptors per cell) were used as a model cell line. Anti-HER2 antibodies (trastuzumab) were first modified with TCO (HER2-TCO; with each antibody bearing ~ 20 TCO (58)). Two types of orthogonal MFNP were then prepared: one with Tz directly conjugated to the particles (MFNP-Tz) and the other with a polyethylene glycol (PEG) spacer between the particle and the orthogonal reactant (MFNP-PEG-Tz). The PEGylation was expected to minimize non-specific MFNP binding to cells. Indeed, when SK-OV-3 cells (in the absence of the primary antibody labeling

step) were incubated with MFNP-PEG-Tz, the background signal from nonspecific binding was significantly smaller (>20-fold) than that of MFNP-Tz (**Figure 2-2 A**). SK-OV-3 cells targeted with HER2-TCO followed by the application of either MFNP-Tz or MFNP-PEG-Tz showed similar dose-dependent responses (**Figure 2-2 B**). With MFNP-PEG-Tz, however, the background signal remained significantly low (**Figure 2-2 B**), which in turn increased the achievable signal-to-noise ratio (SNR; **Figure 2-2 C**). Note that keeping the background signal low is critical to the amplification strategy, as it prevents SNR degeneration during multiple rounds of MFNP-Tz / MFNP-TCO layering.

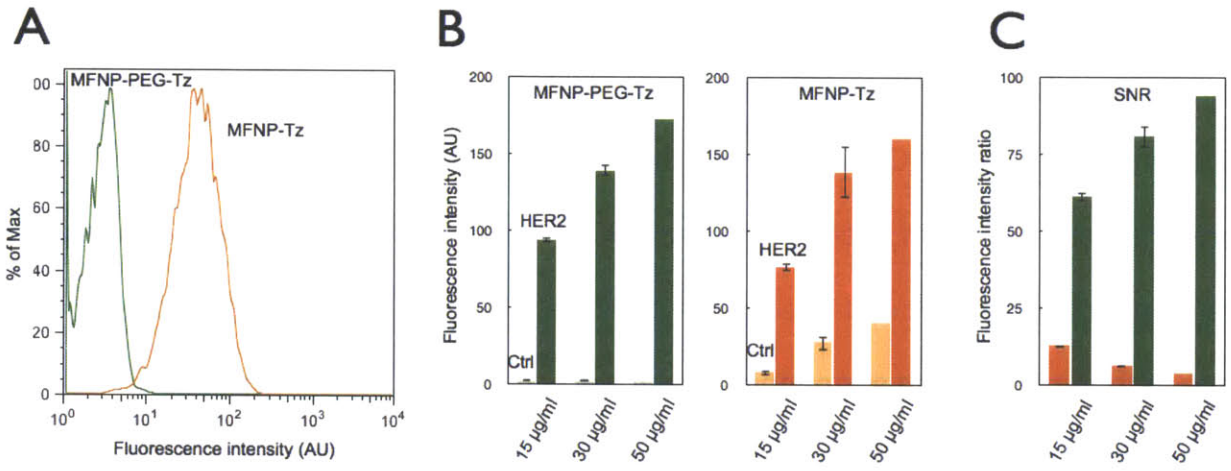

Figure 2-2. Effect of nanoparticle (NP) PEGylation on signal-to-noise ratio (SNR). (A) Flow cytometry experiments comparing SK-OV-3 cells (in the absence of the primary antibody labeling step) incubated with either MFNP-PEG-Tz (green) or MFNP-Tz (orange) for 15 minutes to determine nonspecific cellular binding. PEGlyated particles displayed significantly reduced nonspecific cellular binding. (B) Dose response graphs of specific cellular (*i.e.* HER2 targeting) *versus* nonspecific cellular binding with different NPs. With PEGlayted MFNPs (left panel), non-specific binding is kept at a minimum non-significant level, whereas the non-specific binding increases in a dose-dependent manner with non-PEGlayed MFNPs (right panel). (C) The overall signal-to-noise ratio (SNR) with PEGlyated (green) and non-PEGlyated (orange) MFNPs.

2.3.2 Improved robustness and sensitivity through cleavage

We next quantitated the effects of MFNP-cleavage on detection sensitivity. Following primary cell labeling with HER2-TCO and MFNP-PEG-Tz, SK-OV-3 cells were

further treated with MFNP-PEG-TCO (AMP1). Cell-bound MFNPs were then released by cleaving disulfide linkers (AMP1-C), and separated from cellular contents *via* centrifugation. The transverse relaxation rate (R_2) of samples was subsequently measured by DMR. The cell-number matched comparison showed a significantly higher R_2 following the cleaving method (**Figure 2-3 A**; >200% enhancement in SNR). The observed high R_2 is presumably due to an increase in particle size, as a result of inter-particle clustering between MFNP-PEG-Tz and MFNP-PEG-TCO. It has previously been shown that clusters of small magnetic NPs (<100 nm) are more efficient at accelerating NMR signal decay and thereby result in higher R_2.(49,69-71) Further measurement of particle size by dynamic light scattering supported this hypothesis. The cleaved materials (AMP1-C) had a monodisperse hydrodynamic diameter of ~100 nm, whereas the size of the original particle was ~30 nm. Note that the effect of clustering is more pronounced in the AMP1-C stage as particles are free in suspension, and thus able to further interact with surrounding water molecules. The higher R_2 and homogeneous dispersion of MFNPs in solution rendered the cleaving method more sensitive (>10 times) and robust than direct cellular detection (**Figure 2-3 B**). When subsequently compared with conventional flow cytometry, the gold standard for cellular detection, the cleave-based DMR technique showed an excellent correlation ($R^2 = 0.99$), a finding that validated its analytical capacity (**Figure 2-3 C**).

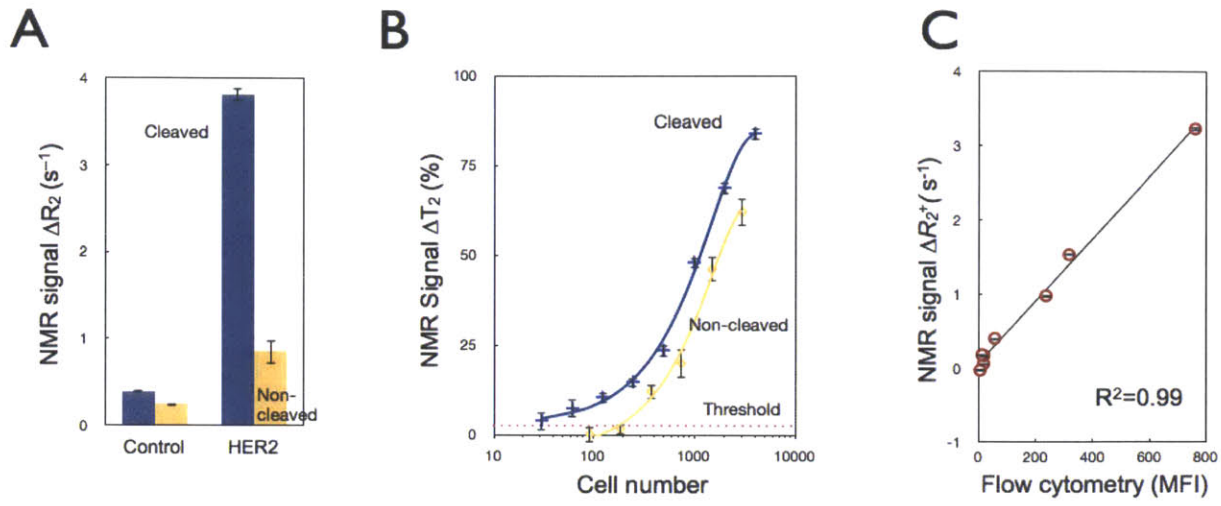

Figure 2-3. Comparison of the cleavage method to whole cell detection. (A) Comparative NMR signals for HER2-targeted SK-OV-3 cells using the cleave (blue) *versus* the non-cleave (yellow) method (~3,500 cells); control samples were incubated with NPs alone. (B) Detection sensitivity of SK-OV-3 cancer cells using the AMP1 and AMP1-C methods (**See Figure 2-1**). Note the ~10-fold increase in detection sensitivity following the cleavage method. Data are expressed as a mean ± standard deviation. (C) Comparative detection between the NMR-based cleavage method and flow cytometry demonstrated an excellent correlation (R^2 = 0.99). Expression levels of four markers (EGFR, EpCAM, HER2, MUC1) across two model cell lines (SK-OV-3, SK-BR-3) were pooled together. NMR detection was performed on ~3,500 cells whereas flow cytometry used ~35,000 cells. MFI: mean fluorescent intensity.

2.3.3 Multiple amplification rounds yield higher SNRs

We next characterized the signal amplification strategy through multiple applications of MFNPs. Cancer cells (SK-BR-3), primarily labeled with HER2-TCO and MFNP-PEG-Tz, were incubated with alternating applications of MFNPs and their orthogonal binding partners: MFNP-PEG-TCO (AMP1), MFNP-PEG-Tz (AMP2). **Figure 2-4 A** shows fluorescent micrographs of labeled cells, where the labeling and amplification steps were made distinguishable by conjugating different fluorescent dyes to the MFNPs. The images show excellent co-localization between these steps, and thereby confirm that the layering indeed amplifies the primary target and not other cellular structures/processes. Equally important was the finding that the MFNP-cleaved cells display negligible fluorescent signals, suggesting that there is maximal MFNP

release into suspension. The DMR assays were performed using MFNP samples that had been cleaved from SK-OV-3 cells after each labeling and amplification step. Successive increases in R_2 were observed with each round of amplification (**Figure 2-4 B**); there was, likewise, a corresponding improvement in detection sensitivities (**Figure 2-4 C**).

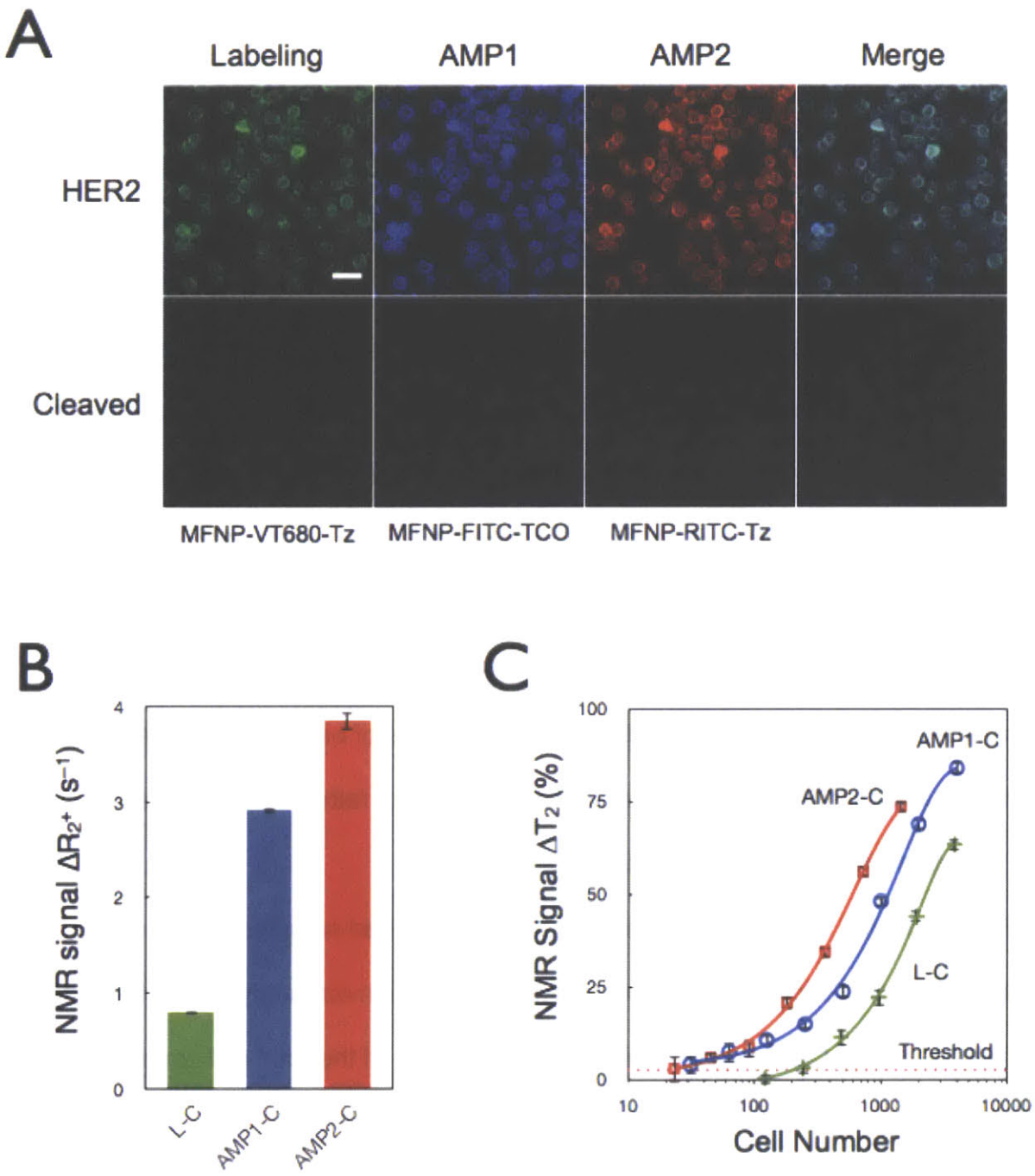

Fig 2-4. Comparison of successive amplification rounds. (A) Fluorescent signals detected from the initial labeling step and for each subsequent amplification step showed excellent co-localization, confirming that multiple MFNP layers can be applied to cellular targets for signal amplification. The MFNP-cleaved cells displayed negligible fluorescent signal, suggesting maximal MFNP release into suspension. The scale bar represents 30 μm. (B) Comparative NMR signal for HER2-targeted SK-OV-3 cells (3,500 cells). AMP2-C conferred the largest increase in SNR but AMP1-C had the highest SNR/unit time. (C) Cellular detection threshold for different cleavage methods (Labeling, AMP1, and AMP2; see **Figure 2-1**) based on HER2 targeting of SK-OV-3 cells.

2.3.4 Application to Clinical Samples

The overall goal of the study was to improve assay sensitivity and robustness in native clinical samples (*e.g.*, fine needle aspirates, biopsies, ascites, blood, sputum), which are inherently complex in composition, as well as heterogenous and variable in cell number (30). We therefore tested our new method for cancer cell detection in malignant human ascites from patients with pancreatic cancer. Samples were divided into two sets, one for the non-cleaving (AMP1) and the other for the cleaving method (AMP1-C). For each set, samples were screened for EGFR (epidermal growth factor receptor), EpCAM (epithelial cell adhesion molecule), HER2, and MUC1 (mucin-1) biomarkers. The cleaving approach was found to produce superior results, revealing otherwise barely or undetectable markers (*e.g.*, MUC1 and EpCAM; **Figure 2-5 A**). Integral to this method's successful detection of low level of biomarkers is the preferential amplification of signals emanating from target rather than from background, which effectively maximizes the SNRs.

For this study, we tested both purified and non-purified samples to reflect the clinical reality and clinical need, respectively. Purification in our study was achieved by negatively selecting CD45+ cells, which comprise ~90% of the total cell concentration in the samples. Due to significant and inevitable cell losses (ofter >40% of the initial cell number), it is always advantageous to avoid or minimize sample purification steps, especially when dealing with complex clinical samples. In both purified and non-purified specimens, MUC1 was labeled using non-cleaving (AMP1) and cleaving (AMP1-C) techniques. DMR measurements of AMP1-C generated the least signal variation between the non-purified and purified sets. Importantly, the non-purified signal was

~90% of the purified signal. Eliminating the cleaving steps (AMP1) reduced the non-purified signal to 16% of the purified signal, as measured by DMR, and to 3% of the purified signal, as measured by flow cytometry (**Figure 2-5 B**). In summary, the cleaving method enhanced detection in unaltered samples, and thus obviated the need for purification steps. Flow cytometry, however, clearly benefits from the inclusion of a purification step when detecting and profiling scarce cells in heterogeneous biological samples such as human derived specimens.

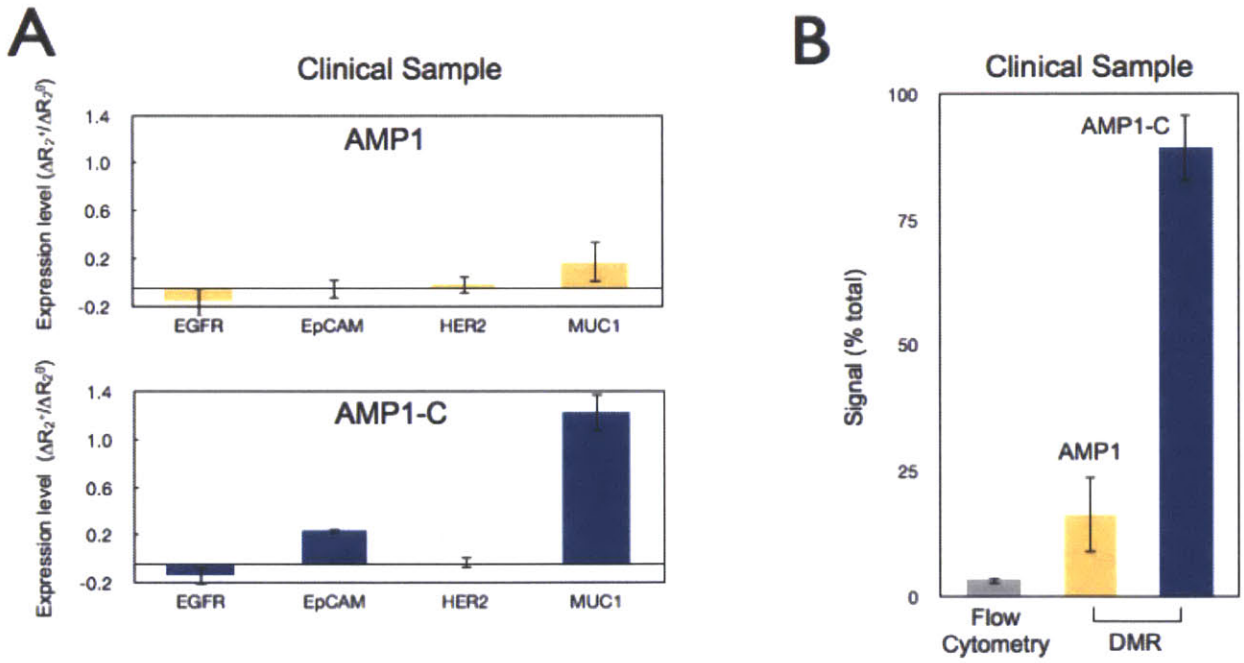

Figure 2-5. Processing of primary clinical samples. (A) Human clinical ascites from pancreatic cancer was profiled for 4 different biomarkers: EGFR, EpCAM, HER2, and MUC1. The AMP1 labeling method was then assessed with and without the subsequent cleavage step. The cleavage step generated higher signal levels. (B) Comparison of different analytical methods (flow cytometry, diagnostic magnetic resonance) for MUC1 detection in clinical samples. Error bars represent the standard error from at least three NMR measurements.

2.4 Disscusion and Conclusions

Utilizing the cycloaddition chemistry for signal amplification, we have developed a new NP-based diagnostic strategy for higher detection sensitivity and robustness. The method relies on i) increasing the number of NPs bound to the target for signal amplification and ii) cleavage of the NP from its target prior to measurement. Amplification is achieved by labeling with successive rounds of complementary TCO and Tz NPs. However, we found that this strategy only works well when background noise remains low. We achieved this by using PEG spacers on the NP surface to minimize non-specific binding of the NP. The cleavage of NPs from labeled cells further increased the detection sensitivity by over an order of magnitude. This was likely a result of a) the MFNPs being surrounded by large numbers of water molecules, which could increase the R_2; and b) cleaved MFNP-Tz and MFNP-TCO forming clusters, which could also increase the R_2. In addition to enhancing sensitivity, the cleavage method also improves the detection reliability; the measurement is free from artifacts caused either by cell sedimentation or by the presence of clumps/extraneous matter often found in clinical samples. Finally, the cleavage method simplifies operation. Results are highly reproducible and longitudinal samples do not have to be analyzed in real time (unless desired). Rather, measurements can be done at the investigator's convenience since, unlike labeled cells where variations can occur due to dissociation of the MFNPs from cells, cleaved MFNPs are stable and do not vary over time. Lastly, because the analytical measurement does not require the cells after the cleavage step, it is possible that rare cells could be relabeled for other biomarkers. For instance, samples could be first profiled for a less abundant marker (MFNP labeling and

amplification followed by cleavage); the same sample then can be screened for more abundant markers using the same MFNP labeling and cleavage strategy (60).

We envision a variety of applications for this technology. While originally developed and optimized for robust cellular analyses and measurements in ascitic fluid, we anticipate that this method could likewise be applied to fine needle aspirates, blood, biopsy specimens, sputum and other biological sources. A particularly interesting application is the possibility of performing multiplexed measurements of rare cells such as circulating cancer cells, immune cell subpopulations or stem cells. Finally, we envision that this novel method could be applied to other profiling methods and nanomaterials. For example, the method could be adapted to ELISA-based MFNP approaches to enable detection of soluble markers in blood or urine. In such assays, the soluble marker would be first captured on micron sized polystyrene beads or microtiter plates before undergoing an AMP2-C procedure to augment sensitivities. It is also possible that this method could be adapted to non-magnetic NPs, *i.e.* using particles detectable by light sensing(72) or by plasmon resonance techniques (73-75).

Chapter 3

DMR Technology applied to Fine Needle Aspirate (FNA) Clinical Study

Parts of this chapter have been published in:
Haun, J.*, Castro, C.*, Wang, R., Peterson, V., Marinelli, B., Lee, H., Weissleder, R. MicroNMR Enables Rapid and Multiplexed Molecular Analysis of Scant Human Cancer Cells. Sci. Transl. Med. 2011 Volume 3, Issue 71, p. 71ra16.

Abstract

While tumor cells obtained by image-guided intervention are a valuable source for clinical cancer diagnostics, conventional means of analysis are limited. Here, we report on a quantitative microNMR system for rapid, multiplexed analysis of cancer cells. We implemented the technology in a clinical setting to analyze cells harvested from 50 patients and validated the results in an independent test set from another 20 patients. Single fine needle aspirates yielded sufficient numbers of cells to quantify multiple protein markers in all patients within 60 minutes. Moreover, we report accuracies for establishing cancer diagnoses of up to 96%, surpassing conventional clinical analyses. Our results also showed time dependent protein expression patterns, underscoring the advantage of near-patient analysis, and a surprising level of expression heterogeneity both across the different patient samples and even within the same tumor, which has important implications for molecular diagnostics and therapeutic drug targeting. The described quantitative point-of-care technique is poised to significantly enhance current molecular diagnostic capabilities.

3.1 Introduction

Primary and metastatic solid cancers comprise cancer cells, structural host cells and inflammatory immune cells. Yet, while individual cancer cells may exhibit a stable signature (76,77), tumors as a whole are highly adaptive and heterogenous (1,2), and thus may respond differently to therapeutics based on stochastic differences in protein levels across the population (78). It is therefore becoming clear that molecular diagnostics of cancer cells will yield critical information for classifying cancers, stratifying patients for molecular targeted therapies and for assessing treatment efficacy (3). An expanded proteomic knowledge of clinically harvested cancer cells will also likely yield new information about tumor biology (4).

Within a clinical setting, primary cancer cells are typically obtained through image-guided intervention or open surgical procedures (79). Percutaneous biopsy is a well established clinical procedure that yields cells for cytology via 22 gauge (G) fine needle aspirates (FNAs) and small tissue fragments for histology via 16-19 G core biopsies. Samples are commonly processed using conventional histological stains, prior to immunohistochemical (IHC) evaluation if sufficient tissue remains (for perspective, tissue sections contain billions of cells). However, the latter is only semi-quantitative, time consuming and can be technically challenging.

To date, the routine study of cancer cells by multiplexed molecular diagnostics has been hampered by four major challenges. First, the standard methods of IHC require tissue fragments (several mm^3), and this limits the number of markers processed per specimen. Procuring more tissue through larger core sizes (< 18G), however, carries increased risk for procedural complications, exacerbated by frequent use of clinically

indicated anticoagulation and/or aspirin. Second, tissue samples may be hypocellular, fragmented or necrotic due to inherent sampling variation. Third, not all proteins of interest are invariably expressed at sufficiently high levels to be detected by routine IHC (80). Finally, manual or automated imaging analyses and quantitation of marker expression can be technically challenging (81). Indeed, non-diagnostic samples and false negative results within larger clinical studies occur in 5-25% of biopsies (82,83), which often leaves clinicians with the dilemma of whether to re-biopsy and further the risk of morbidity. In the present study, we thus sought to develop a point-of care molecular diagnostic system for rapid, quantitative, and multiplexed analysis of cancer cells from FNAs rather than biopsies for near real-time analysis within a clinical setting.

In previous studies, we created nanoparticle based magnetic affinity ligands for both *in vivo* imaging (84,85) and cell based diagnostics using early iterations of miniaturized nuclear magnetic resonance (NMR) devices (27,49). However, although these reports demonstrated the potential for protein analysis of scant cell populations using cell lines and mouse models, such tools had not previously been extended from the regulated laboratory setting into near-patient scenarios due to the technical complexities associated with assay preparation, the need to measure multiple biomarkers rather than single ones, and data processing. Given the finite number of channels in earlier microNMR (μNMR) devices, molecular analyses had previously been limited to 1 to 3 proteins of interest.

Here, we report on a 1) next generation and integrated clinical μNMR device (DMR-3) capable of rapid and quantitative analyses of multiple protein markers and 2) its first human-based application, notably molecularly profiling cancer cells attained

through FNAs. The system incorporates multiplexed measurement capacity, microfluidic specimen delivery, feedback control for temperature variations, and a user-friendly interface within a 10 x 10 cm footprint for clinical bedside operation (**Figure 1-2**). Compared to earlier devices (27,30), DMR-3 is more sensitive, temperature stable, and contains integrated analysis and measurement software. Following optimization of magnetic affinity ligands, we clinically tested this device on 50 patients with suspected malignancies, and then validated our findings in an independent cohort containing an additional 20 patients (n = 70 patients total). To determine whether this new technology could overcome current diagnostic challenges in oncology, the study was specifically designed to address the following questions: a) What is the diagnostic accuracy of the μNMR technology and how does it compare to the current standard-of-care? b) What is the heterogeneity of marker expression within and across patients? and c) What are the *ex vivo* properties of recently harvested cancer cells with respect to marker distribution, cellular half-lives, and changes in biomarker profiles over time (86)? Overall, we showed that processed samples from single FNAs contain sufficiently high cell numbers for real-time, quantitative analysis of numerous molecular biomarkers. We thus anticipate that the technology will have a wide range of applications in oncology and that the approach will be transferable to other markers, cell types and specimens for real-time diagnostics.

3.2 Materials and Methods

3.2.1 Patient population and trial design

Fifty subjects were enrolled from a consecutive series of patients who had been

referred for clinical biopsy of an intra-abdominal lesion. The study was approved by the Massachusetts General Hospital (MGH) Institutional Review Board and informed consent was obtained from all participants. Computed tomography or ultrasound-guided FNA and core biopsies occurring within the MGH Abdominal Imaging and Intervention suites were conducted per routine. Subjects either had an established diagnosis of a solid epithelial cancer or an *a priori* suspicion of cancer, based on imaging results and the presence of tumor markers. One to two FNA passes were obtained and processed for μNMR analyses as described below. Two clinicians (C.M.C. and R.W.), blinded to the μNMR results, reviewed each subject's documented clinical, imaging, and pathology data. In rare instances where pathology was equivocal, data from repeat biopsies and/ or follow-up radiographic imaging were used to reach a consensus on clinical outcome.

In a subset of patients with lesion diameters of at least 2 cm, additional FNA passes were performed to quantitate measurement reproducibility, to measure repeat regional and temporal heterogeneity or to compare μNMR measurements to FACS. To determine reproducibility, μNMR measurements were performed successively for each processed sample without further manipulation. Procedures for measuring repeat sampling heterogeneity involved performing repeated aspirations along the same coaxial needle pass (i.e. single lesion site) or by repositioning to a different region of the same lesion (i.e. multiple lesion sites). Temporal heterogeneity of samples was determined by obtaining and pooling multiple single lesion site FNAs, which were then aliquoted and preserved at 4°C until processing at different time-points.

To determine whether initial findings were generalizable, an independent test set containing an additional 20 subjects were enrolled. Samples from these patients were

processed identically but only the four-marker panel (MUC-1+HER2+EGFR+EpCAM) was assayed.

3.2.2 Sample processing

For each patient, FNA specimens were expelled into EDTA-coated Vacutainer tubes (BD Biosciences) using 2 mL saline for transport. Following centrifugation (400 x g for 5 min) and resuspension, samples were divided into two separate groups for detection of extracellular or intracellular markers. We initially tested a variety of fixation and permeabilization protocols to optimize marker detection and to limit magnetic nanoparticle (MNP) background (**Figure 3-1 A and B**). Based on results from these tests, the extracellular group was lightly fixed with 2% formaldehyde and the intracellular group was fixed with Fix Buffer 1 (FB1, BD Biosciences) and semi-permeabilized with saponin (Perm/Wash buffer, BD Biosciences) as per the manufacturer instructions.

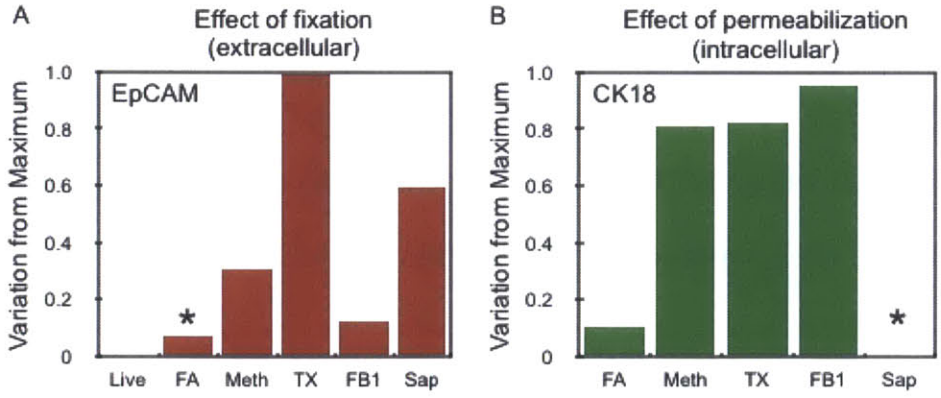

Figure 3-1. The effect of prospective preservation treatments on extracellular (A) and intracellular (B) protein measurements. Live: live cells; FA: 2% formaldehyde; meth: 100% methanol; TX: triton X-100 0.05% in PBS, FB1: Fix buffer 1, BD Biosciences; Sap: saponin. *: optimized conditions chosen for subsequent experiments.

3.2.3 Preparation of trans-cyclooctene (TCO)-modified antibodies.

Monoclonal antibodies against proteins of interest were reacted with (*E*)-

cyclooct-4-enyl 2,5-dioxopyrrolidin-1-yl carbonate (TCO-NHS), which was synthesized as previously reported (66). The reaction was performed using 0.25 to 0.5 mg of antibody and 1000 equivalents of TCO-NHS in 10% dimethylformamide (DMF) for 3 hours at room temperature. Unreacted TCO-NHS was then removed using 2 mL Zeba desalting columns (Thermo Fisher), and antibody concentration was determined by absorbance measurement. TCO valencies were determined based on changes in molecular weight using MALDI-TOF (matrix-assisted laser desorption/ionization-time-of-flight) mass spectrometry (58). Briefly, the antibody was diluted to 150 µg/mL using water and combined at a ratio of 2:1 with sinapinic acid (1 mg dissolved in 0.1 mL 70/30 acetonitrile/water with 0.1% trifluoroacetic acid; Thermo Fisher). 1 µL was then dried onto a sample plate. Data was collected using a Voyager-DE BioSpectrometry Workstation MALDI-TOF mass spectrometer (Applied Biosystems) and analyzed using a custom MATLAB (MathWorks) program. The number of TCO modifications per antibody was then calculated based on the difference in molecular weight compared to the unmodified antibody, and by assuming that a 152.2 dalton net mass was added per TCO (Table S2) (58). Variations in TCO loading were likely the result of differences in the availability of amine sites between different species and IgG subclasses.

3.2.4 Preparation of tetrazine (Tz) modified magnetic nanoparticles (MNPs)

Cross-linked iron oxide (CLIO) nanoparticles were prepared as described previously (49). Briefly, 3 nm monocrystalline cores composed of $(Fe_2O3)_n(Fe3O4)m$ were synthesized within a matrix of 10 kDa dextran. These were cross-linked with epichlorohydrin and reacted with ammonia to produce MNPs with primary amine groups

(NH_2-MNPs). The number of amines per MNP was approximately 89, as determined by reaction with *N*-succinimidyl 3-(2-pyridyldithio) propionate (SPDP; Thermo Fisher) and dithiothreitol. The hydrodynamic diameter was 28.8 nm, as measured by dynamic light scattering (Zetasizer 1000HS; Malvern Instruments). At 40°C and 0.47 T (Minispec MQ20; Bruker), the R_1 and R_2 relaxivities were 25.2 mM^{-1} s^{-1} and 64.5 mM^{-1} s^{-1}, respectively. Tz-MNPs were created by reacting NH_2-MNPs with 500 equivalents of 2,5-dioxopyrrolidin-1-yl 5-(4-(1,2,4,5-tetrazin-3-yl)benzylamino)-5-oxopentanoate (Tz-NHS), synthesized as previously reported (58). This reaction proceeded in PBS containing 5% DMF for 3 hours at room temperature. Excess Tz-NHS was removed by gel filtration using Sephadex G-50 (GE Healthcare). Tz-MNP concentration was determined by absorbance measurement at 410 nm using a known standard for calibration. MNP molar concentration was then determined based on an estimated molecular weight of 447,000 dalton (8000 Fe atoms per core crystal, 55.85 dalton per Fe atom (65)). Tz-MNPs were stable at pH 6.5 for several months as determined by analytical methods.

3.2.5 MNP targeting and detection by nuclear magnetic resonance

Each specimen was divided into aliquots in microcentrifuge tubes and incubated with TCO-modified monoclonal antibodies (10 µg/mL) in 0.15 ml of the appropriate buffer (extracellular samples: PBS containing 1% BSA, or PBS+; intracellular samples: saponin-based Perm/Wash from BD Biosciences containing 1% BSA, or PW+) for 10 minutes at room temperature. Samples were then pelleted by centrifugation, aspirated, and resuspended directly with Tz-MNP (100 nM). After incubating for 30 minutes at room temperature on a rotator, samples were washed twice by centrifugation with PBS+

or PW+, washed once with PBS, and then resuspended in 20 µL PBS.

3.2.6 The µNMR device and its operation

In this study, we designed a new µNMR system (DMR-3) specifically intended for clinical applications. The µNMR system conceptually consists of solenoidal microcoils, a portable magnet, and custom-built NMR hardware (**Figure 1-2**). To maximize the sample filling factor (≈ 1) and hence the NMR signal level, the solenoidal coils were embedded in polydimethylsiloxane (PDMS) along with the fluidic channels. Samples were either directly injected to the fluidic channels, or were contained in thin-walled (thickness: 25 µm) tubes which were then inserted into the coil bores. The coils were mounted on a printed circuit board containing impedance matching networks and multiplexers. A polarizing magnetic field (0.5 T) was generated by a portable, permanent magnet (PM1055-050N, Metrolab). The NMR hardware houses a digital signal processor (DSP) unit (C2000 series, Texas Instruments), a radio frequency (RF) generator (AD9954, Analog Devices) and an analog-to-digital converter (AD7690, Analog Devices). The DSP unit controls the entire operation of the system, and communicates with an external smartphone for user-inputs. For robust NMR measurements, the DPS unit was programmed to maintain a constant offset between two frequencies: the NMR frequency (determined by the external magnetic field) and the RF carrier (for excitation). The transverse relaxation rate (R_2) was measured within the 1 µl sample volume of the microcoil using Carr-Purcell-Meiboom-Gill pulse sequences with the following parameters: echo time (TE): 4 ms; repetition time (TR): 6 s; the number of 180° pulses per scan: 500; the number of scans: 8. R_2 values were

subtracted from the R_2 value for PBS alone to obtain ΔR_2. Marker levels were calculated as described in the Supplementary Materials and Methods.

3.2.7 Statistics

The Spearman correlation coefficient was used to assess the correlations between different variables, and the nonparametric Mann-Whitney test was used to determine the magnitudes of between-group differences. Random effects models were used to separate within-subject variability (reproducibility of the NMR measurements) from between-subject variability. We constructed receiver operating characteristic (ROC) curves for individual markers and selected marker combinations by plotting sensitivity versus 1-specificity and calculated the areas under the ROC curves (A_z). An $A_z = 0.5$ was used to indicate that the test shows no difference between the two groups while an $A_z = 1.0$ was used to indicate that the test gives a perfect separation between the groups. When assessing discrimination accuracy of marker combinations, we first used logistic regression to estimate a risk score function and then constructed the ROC curves based on this risk score function. We defined the optimal cutoff value for identifying malignant status as the point on the ROC curve with the minimal distance between the 0% false-negative and the 100% true-positive rate. We calculated sensitivity, specificity, as well as accuracy, using standard formulas. We also employed a "leave-one-out" cross-validation method to calculate prediction accuracy for a future patient. Specifically, we omitted one sample before selecting the optimal cutoff point using the remaining samples. We repeated this until every sample had been left out once and then calculated the prediction accuracy based on the accuracy rates for the

left-out samples. We used the bootstrap method to estimate the standard errors for the prediction accuracy rates estimated from the "leave-one-out" cross-validation. All tests were two-sided and a P-value less than 0.05 was considered statistically significant. All μNMR and MALDI-TOF measurements were performed in triplicate and the data are presented as the mean ± standard error.

3.3 Results and Discussion

3.3.1 Cellular samples can be quantitated

A total of 50 patients, presenting with suspected abdominal malignancies and referred for routine biopsy, were initially enrolled in the study. Of these, 44 patients' lesions were ultimately malignant and 6 patients' lesions were benign, as determined by repeat core biopsies, serial follow-ups, imaging (including PET-CT), and/or from clinical information (**Table 3-1**). For each patient, a 1-2 pass FNA sample was obtained using a 22G needle. This was followed by a series of routine core biopsies (17G) for conventional standard-of-care analysis. In selected patients, additional FNA samples were obtained to further quantify sample heterogeneity and to validate our measurements against accepted gold standards (see below). Each FNA sample was washed with 1-2 mL of buffered saline and processed for μNMR for subsequent measurement of 11 variables: 9 cancer related markers (EpCAM, MUC-1, HER2, EGFR, B7-H3, CK18, Ki-67, p53, and Vimentin), a CD45 count, and the total cell density. *A priori* selection of these protein markers were based on current practice (e.g. EpCAM and CK18) (87,88) or on reports of clinically relevant over-expression (89-91).

Table 3-1. Clinical information for 70 patients with suspected abdominal malignancies.

Characteristic	Original diagnostic set		Independent test set	
	Number	%	Number	%
Number of patients	50		20	
Age				
Median	64		63	
Range	29-86		24-90	
Gender				
Male	24	48%	7	35%
Female	26	52%	13	65%
Lesion type				
Malignant	44	88%	14	70%
Benign	6	12%	6	30%
Tumor Subtypes				
Breast	2	4.5%	2	14%
Gastrointestinal	13	30%	4	28%
Genitourinary	3	6.5%	1	7%
Gynecologic	4	9%	3	22%
Lung	8	18%	1	7%
Pancreatic	7	16%	3	22%
Undifferentiated	7	16%	0	0%
History				
Prior history of cancer	30	60%	4	20%
No prior therapies	20	42%	7	35%
Active treatment	11	22%	9	45%
Biopsy Site*				
Visceral	36	72%	9	45%
Non-visceral	14	28%	11	55%
Lesion Size (axial dia.)				
< 1 cm	3	6%	10	50%
1-3 cm	25	50%	6	30%
> 3 cm	22	44%	4	20%
Biopsy Modality				
Ultrasound	14	28%	16	80%
CT	36	72%	4	20%

*Visceral sites include, liver, brain, adrenal glands, pancreas, and kidney. Nonvisceral sites include lymph nodes, abdominal wall, breast, bones, and skin.

To maximize detection sensitivity, we adapted a highly efficient bioorthogonal approach for sensing that uses *trans*-cyclooctene (TCO) / tetrazine (Tz) chemistry (58). Curves calibrating μNMR signals with cellular expression levels for each of the markers were obtained prior to the study. Our μNMR-derived measurements of markers in clinical samples correlated well against accepted gold standards (**Figure 3-2**). For example, the correlation coefficient between μNMR and ELISA measurements for EGFR, a clinically important marker, was 0.99 (**Figure 3-2 A**).

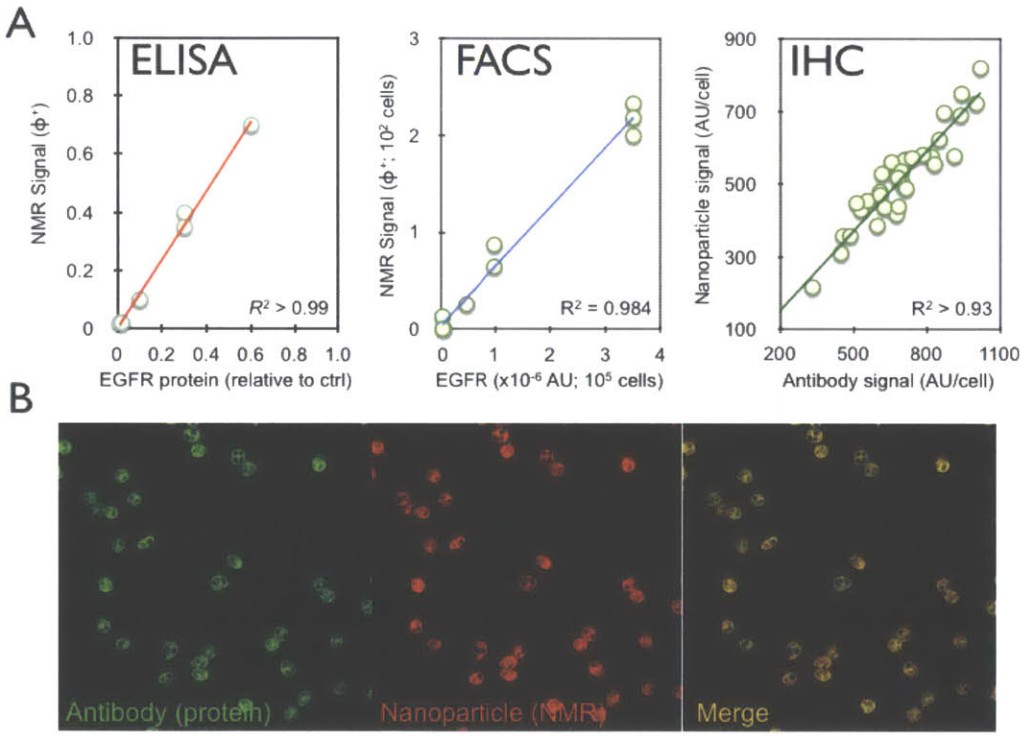

Figure 3-2. Validation of NMR measurements. (A) Plots showing the correlation of EGFR measurements obtained by μNMR versus ELISA, FACS or immunohistochemistry (IHC) in clinical samples where sufficient cells were available for conventional proteomic techniques (typically $10^{5\text{-}6}$ for ELISA and FACS versus 10^2 for DMR). Note the excellent correlation coefficients for the different methods. (B) Representative immunofluorescent stains of a representative human sample. The primary antibody (green) was labeled with AlexaFluor-488 and TCO. The magnetic nanoparticle (red) was labeled with VT680 and Tz. Note excellent co-localization between nanoparticles (conferring NMR properties) and antibody (protein content).

All FNA samples yielded sufficient cell numbers for subsequent μNMR analysis. On average, 3,866 ± 456 cells were obtained per patient. Of these, approximately one-

third were CD45-positive leukocytes (1,354 ± 207 cells). The remaining cells were non-leukocytes, primarily tumor cells (as determined by extensive FACS analysis in optimization studies), and these were aliquoted into samples containing an average of ~200 cells for each of the 9 biomarker measurements. To determine the global expression levels of each marker, we created waterfall plots to determine overall distribution (**Figure 3-3**). As expected, there was a spectrum of marker expression with approximately one-third of samples each showing high, intermediate, and low or absent protein levels, respectively. Benign samples typically fell into the latter two categories.

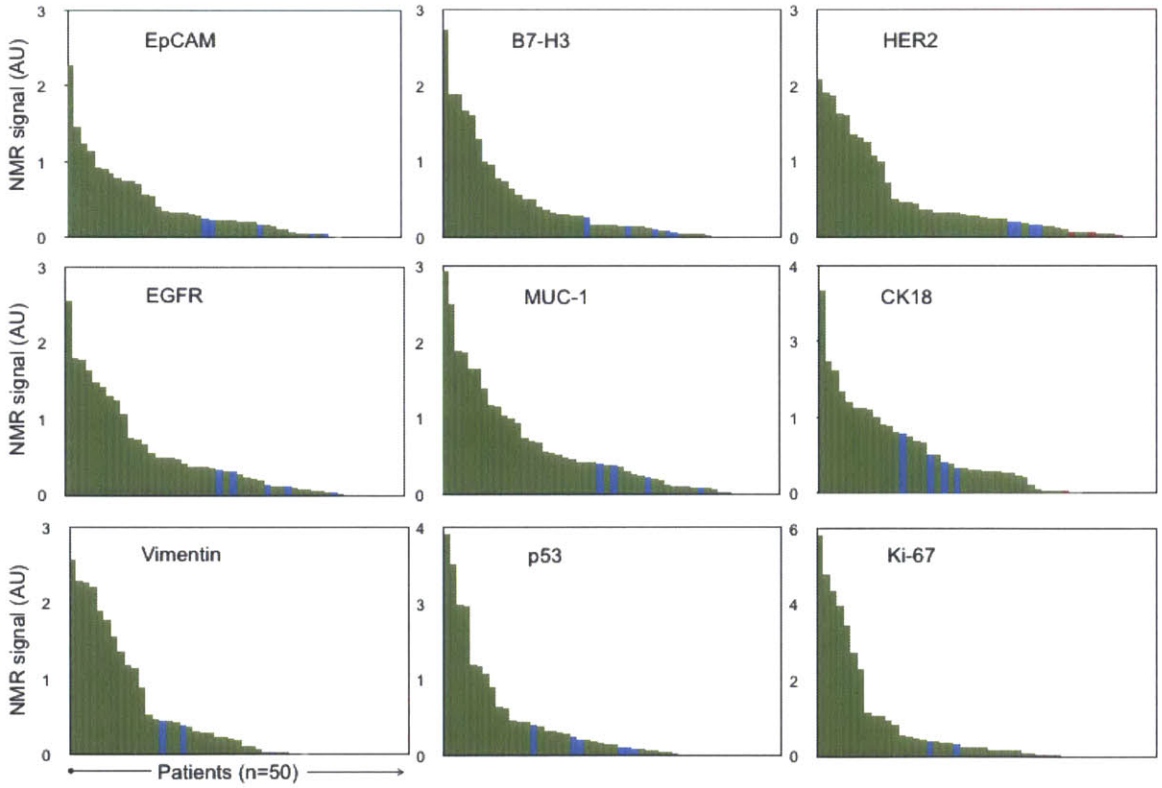

Figure 3-3. Biomarker expression level distribution. Waterfall plots showing the expression levels of each of the different biomarkers sorted from high (left) to low (right). Each column represents a different patient sample (green = malignant; blue = benign).

3.3.2 Heterogenous protein expression levels across epithelial tumors

To determine whether protein expression levels (shown in **Figure 3-3**) correlated

between samples, we plotted them for each patient and found that there was considerable heterogeneity in the magnitude of expression across patient samples (**Figure 3-4**). To further examine the interrelationship between markers, we calculated Spearman correlations. MUC-1, EGFR, B7-H3 and HER2 demonstrated moderate correlations with one another (coefficients ranging from 0.4-0.6). No strong associations were found between EpCAM expression and the other four extracellular markers. Intracellular and extracellular marker expressions did not correlate strongly with one another. In the samples tested, no single marker was able to universally discriminate between malignant and benign samples.

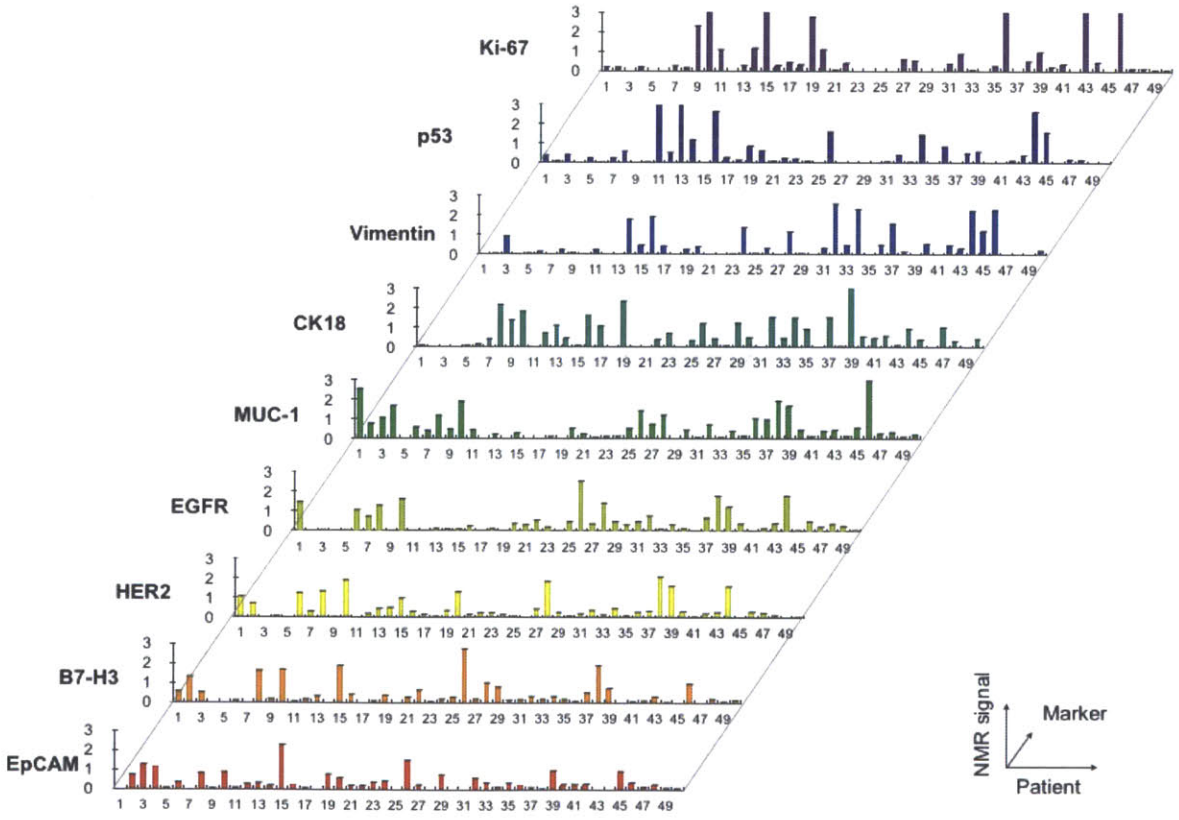

Figure 3-4. Expression levels of different biomarkers arranged by patient number. Patients 5, 12, 17, 18, 21, 42 had benign lesions.

3.3.3 Diagnostic sensitivity, specificity, and accuracy of cancer markers

To determine the clinical performance of the nine cancer-related markers, we performed receiver operating characteristic (ROC) analyses. **Figure 3-5** compares the areas under the ROC curves (A_z values) for individual markers, a dual marker pair (EpCAM + CK18), as well as for the best triple and quadruple marker combinations. We next established a threshold for creating a classification rule based on a single marker or on the estimated risk score function of a marker combination.

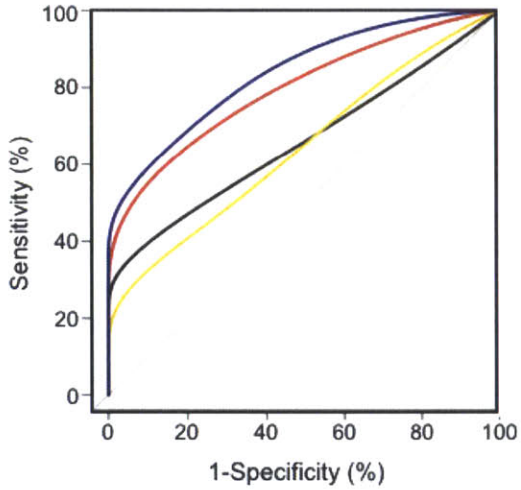

Marker	Az	Standard error	95% CL
MUC-1	0.8220	0.0775	0.6701 - 0.9738
EGFR	0.7462	0.0840	0.5815 - 0.9109
B7-H3	0.7140	0.0868	0.5439 - 0.8841
HER2	0.7140	0.0741	0.5688 - 0.8592
Ki-67	0.6875	0.1059	0.4800 - 0.8950
EpCAM	0.6534	0.0922	0.4727 - 0.8342
Vimentin	0.6439	0.1168	0.4150 - 0.8729
CK18	0.5890	0.1295	0.3352 - 0.8428
p53	0.4470	0.0785	0.2932 - 0.6007
EpCAM+CK18	0.6572	0.1169	0.4281 - 0.8863
MUC-1+HER2+EGFR	0.8636	0.0781	0.7106 - 1.0000
MUC-1+HER2+EGFR+EpCAM	0.8826	0.0781	0.7295 - 1.0000

Figure 3-5. Receiver operating characteristic (ROC) curves for single markers, a dual marker set, as well as for triple and quadruple marker combinations to determine optimum DMR threshold values. A_z: area under the curve. 95% CL: 95% confidence limits.

Optimized diagnostic marker combinations and their discriminatory values were then retrospectively analyzed for each patient sample (**Table 3-2**). Among individual markers, MUC-1 displayed the highest area under the curve (A_z= 0.82), closely followed by EGFR and HER2. Interestingly, EpCAM, a marker routinely used for circulating tumor cell (CTC) analysis and enrichment (92), showed a lower A_z (0.65). Even the combination of EpCAM and CK18 (the accepted criteria used to identify CTCs in peripheral blood) showed a low A_z (0.66). **Table 3-2** summarizes the diagnostic sensitivity, specificity and accuracy for each marker and combination of markers, along

with their respective optimized μNMR threshold values for malignancy. The highest accuracy for our cohort was observed for a statistically weighted (see Methods) quadruple marker subset (MUC-1 + EGFR + HER2 + EpCAM; 96% accuracy); this was followed closely by weighted triple markers (MUC-1 + EGFR + HER2; 92% accuracy). EpCAM and CK18 achieved an overall diagnostic accuracy of 80%, where a higher sensitivity (84%) was offset by low specificity (50%). The quadruple marker combination correctly diagnosed 48 out of 50 cases as either malignant or benign. Interestingly, both incorrect cases (patients 21 and 42) contained only core biopsy evidence of inflammation, marked by the presence of reactive fibrosis, histiocytes, and other inflammatory cells. It is well appreciated that when the same data set is used to generate a classification rule and to derive diagnostic accuracies the results may be overly optimistic. To reduce this potential bias, we used "leave-one out" cross-validation techniques to estimate prediction accuracies and used the bootstrap method to estimate the standard error for the accuracy estimate. To eliminate any remaining bias, we also employed an independent patient test set.

Table 3-2. The sensitivity, specificity and accuracy of different markers (single or in combination).

Number	Marker	DMR value	Sensitivity (%)	Specificity (%)	Accuracy (%)
Single	MUC-1	0.25	66	83	68
	EGFR	0.20	64	83	66
	B7-H3	0.11	68	67	68
	HER2	0.24	64	100	68
	Ki-67	0.10	68	67	68
	EpCAM	0.21	59	67	60
	Vimentin	0.08	59	67	60
	CK18	0.06	73	50	70
	p53	0.38	41	83	46
Dual	EpCAM + CK18 (unweighted)	0.27	84	50	80
	EpCAM + CK18 (weighted)	0.65	73	67	72
Triple	MUC-1 + HER2 + EGFR (weighted)	1.23	95	67	92
Quad	MUC-1 + HER2 + EGFR + EpCAM (weighted)	1.6	100	67	96

3.3.4 Confirmation in independent test set

To eliminate potential sources of error, data over-fitting and to comply with recently published expert recommendations for proteomic biomarker studies (93), we tested the 4-marker panel in 20 additional patients (**Table 3-3**). μNMR was able to establish correct diagnoses for all 20 patients at an accuracy of 100% and at a 95% confidence interval of 83.2-100%.

Table 3-3. Verification of the diagnostic value for the four-panel markers in an independent test set of 20 patients.

Patient	DMR values					DMR diagnosis	True diagnosis
	MUC-1	HER2	EGFR	EpCAM	Quad		
51	0.17	0.00	0.19	0.02	0.37	Benign	Benign
52	0.00	0.00	0.00	0.00	0.00	Benign	Benign
53	0.00	0.09	0.01	0.06	0.16	Benign	Benign
54	1.35	0.89	4.38	1.83	8.44	Malignant	Malignant
55	8.03	0.49	0.89	2.86	12.27	Malignant	Malignant
56	0.55	0.33	0.24	0.31	1.43	Benign	Benign
57	8.28	0.00	0.60	1.83	10.71	Malignant	Malignant
58	0.21	0.73	0.00	1.11	2.05	Malignant	Malignant
59	2.57	0.67	1.10	2.37	6.70	Malignant	Malignant
60	1.10	0.23	0.59	0.51	2.43	Malignant	Malignant
61	7.62	1.34	1.19	5.28	15.43	Malignant	Malignant
62	1.47	0.00	0.98	1.05	3.50	Malignant	Malignant
63	5.08	0.27	5.15	5.91	16.42	Malignant	Malignant
64	1.35	0.89	3.38	0.00	5.61	Malignant	Malignant
65	2.52	0.99	0.69	1.13	5.32	Malignant	Malignant
66	0.85	0.97	0.27	0.02	2.11	Malignant	Malignant
67	0.00	0.29	0.86	0.60	1.74	Malignant	Malignant
68	2.96	1.97	0.00	1.01	5.94	Malignant	Malignant
69	0.46	0.21	0.06	0.06	0.80	Benign	Benign
70	0.00	0.65	0.00	0.65	1.30	Benign	Benign

3.3.5 Comparison to the standard-of-care

The mean clinical turn around time for conventional pathology, from sample submission to final report, was 3 days for cytology (range 1-8 days) and 4 days for surgical pathology (range 1-11 days). The measurement time for μNMR was typically < 4 hrs. Conventional cytology on FNA specimens was performed in 49 of 50 cases and

was diagnostic in 36 of 49 cases (accuracy 74%; **Table 3-4**). Conventional histology was obtained on all cores and correctly diagnosed 45 cases (accuracy 84%; **Table 3-4**). The remaining results were either non-diagnostic (5 cases) or false negative (8 cases). Thus, μNMR performed consistently better (accuracy 96%; **Table 3-4**) than the current standard-of-care.

Table 3-4. Verification of the diagnostic value for the four-panel markers in an independent test set of 20 patients.

Technique	n	Diagnostic	Nondiagnostic	Misdiagnosis	Sensitivity (%)	Specificity (%)	Accuracy (%)
Fine needle aspirate	49	36	13	11	70	100	74
Core biopsy	50	45	5	8	82	100	84
DMR	50	50	0	2	100	67	96

3.3.6 Other markers

A key determinant of cancer prognosis is the rate of tumor proliferation. In this study, the cell cycle marker Ki-67 was measured to gauge the proliferative index in malignant cells. The proliferate index was found to vary considerably (range: 0-100%) across all patients and across subgroups of patients with the same disease and at similar stages (e.g. colorectal cancer: proliferative index 1-100%; pancreatic ductal adenocarcinoma: proliferative index 3-75%). However, when patients were classified into treatment responders and non-responders, Ki-67 showed statistically significant differences between the groups ($p = 0.0087$). The responders had a mean value of 6% proliferation (range: 0-13; standard error: 3.3) while the non-responders had a mean value of 23% (95% CI: 10-36; standard error: 6.3). We also determined cancer associated leukocyte counts for each FNA sample. However, there was considerable

variability across all samples, non-responders showed significantly higher levels of leukocytes in FNA samples (37.5 ± 25.4 % vs. 28 ± 20.7%). This finding is consistent with earlier reports that an inflammatory signature is indicative of worse prognosis (94-96). Protein levels of p53 also showed a wide variability but were not found to differ significantly between responders and non-responders. Finally, we investigated vimentin as a cancer marker since this intermediate filament protein has been associated with epithelial mesenchymal transition (97), metastases (98) and therapy resistance (99). In this study, vimentin was not found to add any further diagnostic information to that provided by other markers. Instead, we observed that vimentin levels appear to correlate with patient treatment history. Compared to their chemotherapy-naive counterparts, actively or pretreated malignant lesions expressed higher vimentin levels (mean 0.78 ± 0.20 vs. 0.30 ± 0.11; p=0.04).

3.3.7 Variability

Clinicians regard data from a single pathological snapshot as proxies to the intrinsic biology of the tumor at the time of biopsy. However, when such information is used to make significant medical decisions, such as whether to initiate chemotherapy in the neoadjuvant setting (i.e. before surgery), data fidelity and reliability become paramount. We therefore sought to identify the sources contributing to potential sample variability. We initially determined the reproducibility of the μNMR measurements (n=30 samples), and confirmed that repeated measurements of each sample produced similar results (< 0.6% variability overall and < 0.3% for intracellular markers; **Figure 3-6 A**). This finding is remarkable for non-purified, blood-containing samples of cellular protein

biomarkers. However, when different needle aspirates (n=13) were obtained along the identical coaxial needle pass, considerable heterogeneity was observed (**Figure 3-6 B**). While for most extracellular markers, variation from the mean only reached a maximum of 30%, variation for intracellular markers such as p53 (**Figure 3-6 B**) was more pronounced. However, when additional samples were obtained from different regions of the same tumor, even extracellular markers showed mean variabilities of ~90% (**Figure 3-6 C**). Finally, it is important to note that clinical samples are often processed in central laboratories and spend variable amounts of time in transit and in refrigerators before batch processing. To determine how such treatment might affect protein measurements, we stored sample aliquots at 4°C for various amounts of time prior to processing (**Figure 3-6 D**). Surprisingly, we observed a considerable decrease in marker expression over time, with a mean loss of approximately 100% within the first hour after sampling. After 3 hours, marker loss appeared to plateau, when marker expression was down by about 400%. These changes likely reflect differences in protein half-lives as well as degradation by proteases and/or pH drifts in the samples.

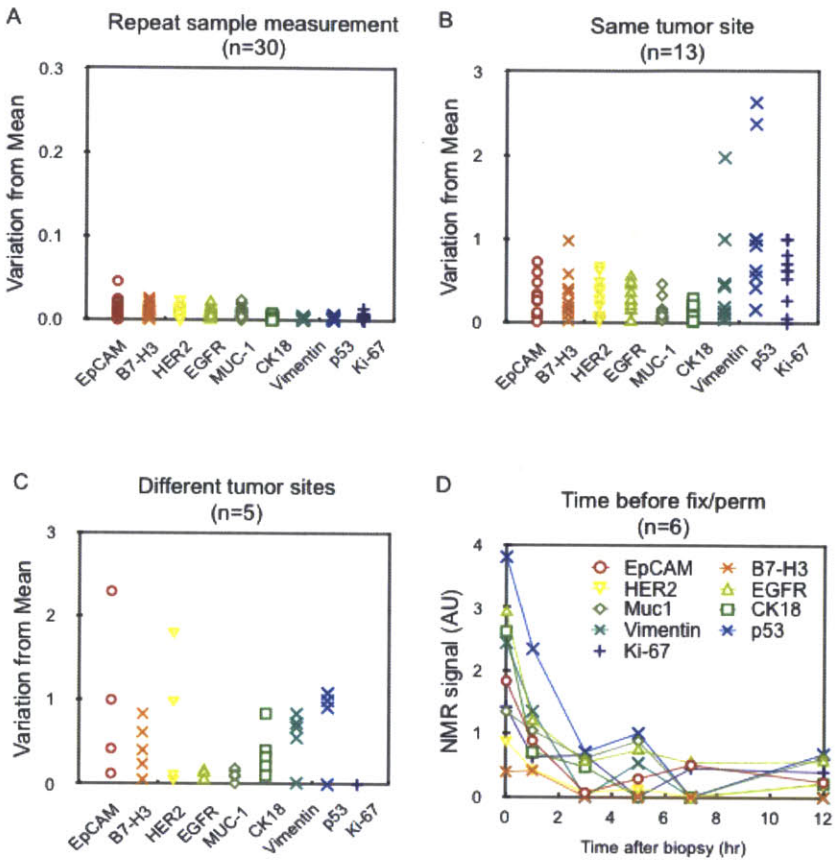

Figure 3-6. Analysis of sample heterogeneity. (A) Repeat measurement of the same samples (note the different scale compared to other graphs). (B) Measurement of repeat FNA samples obtained via the same coaxial needle. (C) Measurement of repeat FNAs from different tumor sites. (D) The effect of time at 4°C before fixation (e.g. during transport to central laboratory facility) on protein measurements. Note the rapid change in expression levels in unfixed samples.

3.4 Conclusions

While results from several studies have indicated that molecular profiling of solid tumors improves treatment stratification (100) and efficacy monitoring (101), failure to detect molecular heterogeneity in cancer patients can lead to underpowered clinical trials (102). However, the availability of serial tumor tissue to make such decisions during treatment is often limited since core biopsies carry procedural risks, are time consuming, and are costly. Moreover, biopsies often yield small amounts of tissue (several mm^3), which allow for only limited analyses. Conventional methods for molecular profiling (immunohistochemistry, flow cytometry or proteomic techniques)

often require considerable cell and/or tissue quantities, both of which are not easily obtained via FNA. These caveats have fueled an intense interest in developing more sensitive technologies for enabling broader profiling of tissue in limited clinical specimens. Recent advances in nanotechnology and device miniaturization have made sophisticated molecular and cellular analyses of scant tumor samples possible, albeit often under well-controlled experimental conditions (27,45,103). Yet, despite the development of various platforms through the NCI's Cancer Nanotechnology Initiative (104-106), only few of these have advanced into clinical feasibility trials (1,87,88,92,107,108).

The current clinical study revealed several unexpected findings. First, we observed considerable expression heterogeneity for all biomarkers across the sample populations. For example, EpCAM, the current marker of choice to define CTCs was only highly expressed in ~60% of cancers and completely absent in ~20%. Second, we observed significant expression heterogeneity along identical and distal biopsy sites within a given tumor lesion. These findings have important implications for both molecular diagnostics and therapeutic drug targeting. Third, we obtained time courses on protein viability that demonstrated rapid decay, informing the need for prompt proteomic and other molecular measurements of human samples. Finally, we show that molecular profiling based on multi-marker diagnostics in a point-of-care setting can have higher diagnostic accuracies when compared to state-of-the-art conventional pathology.

Of the individual markers investigated, MUC-1, HER2, EGFR, and EpCAM provided the highest diagnostic accuracy. Combining these four markers established correct diagnoses in 48 of the 50 patients in the initial cohort, and in all 20 patients in

the independent test set. This accuracy was superior to conventional clinical analysis. In the two misclassified cases, core biopsy showed significant inflammation and an absence of cancer cells. Although not attempted in this particular study, incorporating additional markers (e.g. CD163, CD14, CD16, CD33, and 5B5), which define monocyte, macrophage, and fibroblast populations more accurately, would make characterizing the inflammatory and stromal components of FNAs possible, and could increase specificity (109-112). The current study was specifically designed to include a range of intra-abdominal tumor types so as to simulate the typical clinical referral pattern seen at an interventional service. While peripheral to the central study aims, it is noteworthy that the three and four marker combinations were found to offer similar predictive accuracies, both being superior to EpCAM alone and to conventional cytopathology. While this study was not powered to be specific for particular cancer subsets, it is likely that protein markers could be tailored to recognize specific epithelial (e.g. prostate, lung cancer) or non-epithelial cancers (e.g. melanoma, sarcoma, lymphoma).

With respect to protein stability, we discovered early on that all cancer markers displayed relatively short half-lives once harvested. To date, very limited information has been available on the half-life of protein expression levels in aspirated cancer cells, and marker degradation may be one of the reasons for the lower detection sensitivities reported in some studies. Proteomic studies of freshly harvested nonmalignant cells have demonstrated that up to 40% of protein markers are differentially expressed when *in vivo* to *in vitro* conditions are compared (86). Within the first hour after harvesting, we observed a mean decrease of ~100% in marker expression across the different markers studied (Fig. 9). The magnitude of this effect was unexpected and indicates that

samples either require rapid analysis (e.g. within minutes) or careful preservation using optimal methods, such as those used in all of our clinical samples, to maintain molecular expression integrity.

The μNMR device in its current form (DMR-3) is an advanced prototype specifically designed for clinical operation and has been significantly improved over previous prototypes such as DMR-1 (27) and DMR-2 (30). The DMR-3 system incorporates several new features, notably: a) an array of solenoidal coils for multiplexed detection; b) a disposable, thin-walled sample container, which tightly slides into the coils; c) custom designed and easy to use NMR hardware which automatically tunes measurement settings (NMR frequency, pulse width, and power) to compensate for environmental factors such as temperature fluctuations. Compared to other analytical techniques, the main advantage of μNMR is its capacity for rapid measurements with little interference from blood, i.e., it allows for analyses of non-purified samples. The platform is also versatile and scalable to easily accommodate additional biomarkers of interest, it offers robust portable operation, and is relatively inexpensive compared to conventional histopathology, all key attributes for emerging nanotechnology-based diagnostics. Despite these advances and advantages, we believe that DMR-3 could be further enhanced to maximize clinical utility. We anticipate furnishing the device with more advanced multichannel measurement and microfluidic (e.g. separation) capabilities to facilitate on-chip processing of whole blood samples. Likewise, we are currently exploring additional technologies for combining sensitive μNMR measurements with higher throughput purification chips (87). We are also investigating technologies for the analysis of individual, magnetically tagged cells using

miniature magnetometer sensors. Achieving single cell resolution will enable the diagnostic study of very rare cells, such as CTCs for screening or monitoring cancer recurrence (113,114). Finally, sensitive and detailed analyses of other cell types including immune cells, stem cells or non-epithelial neoplasms could be performed using μNMR, which could thus facilitate the development of additional surrogate endpoints for clinical trials (4,101,115).

We show that the μNMR technology can yield highly sensitive and reproducible data, with implications for enhancing clinical decision making. The method relies on a sophisticated technology rooted in the basic principles of NMR (27) as well as on exploiting advanced nanoparticle targeting strategies (58). Extracting concurrent molecular information from FNAs could minimize the incidence of non-diagnosis associated with existing standards-of-care and even improve diagnostic accuracies. Moreover, this minimally invasive procedure paves the way for repeated tumor samplings at various time points. Neoadjuvant treatment, for example, is a clinically accepted approach where chemotherapy precedes surgical resection. Serially interrogating tumor lesions during treatment would offer multiple windows into its biology and response characteristics. Moreover, the clinical utility of repeated biopsies for such purposes has longstanding precedence in clinical research (116-118). More recently, it has been shown that patients with various treatment refractory malignancies clinically benefit from use of conventional laboratory methods to measure therapy-specific proteins and/or genetic markers in core or surgical tumor biopsies (3). Harnessing the rapid, multiplexed, and sensitive detection attributes of μNMR could enable future molecular profile-directed studies in sample restricted trials.

We envision a number of specific clinical applications not tested here in which μNMR could be particularly useful, namely a) for rapid detection and serial profiling of commonly attained specimens (thyroid FNAs, paracentesis, thoracentesis, peripheral blood, and image-guided or surgical biopsies), b) for repeat treatment assessment ("pharmacodynamics"); or c) for robust and tumor-specific profiling of blood microvesicles (exosomes). We anticipate that this versatile technology will find a wide range of applications in oncology as it enables molecular diagnostics at the bedside, and has the potential for redefining the standard-of-care during diagnostic work up.

Chapter 4

Profiling Ascites Tumor Cells (ATCs) reveals reliable targets for detection using a novel point-of-care microfluidic chip

Part of this chapter is under review (July, 2013):
Peterson, V.*, Castro, C.*, Chung, J., Miller, N., Ullal, A., Castano, M., Penson, R., Lee, H., Birrer, M., Weissleder, R. Ascites tumor cell analyses reveal reliable targets for enrichment and profiling using a novel point-of-care microfluidic chip.

Abstract

Ascites tumor cells (ATCs) represent a potentially valuable source of information for diagnosing ovarian cancer and monitoring its treatment response. Yet, surprisingly little is known about ATC protein expression patterns and trends during treatment in part due to the large number of host cells in ascites that confound analyses. Such challenges call for novel point-of-care diagnostic devices to isolate ATCs and expand the reach of ascites collection beyond palliation. We selected and evaluated 85 putative ovarian cancer protein markers and found that nearly two-thirds were either non-specific for malignant disease or had low abundance. A reduced panel of 31 markers was then tested in a training set of clinical specimens, where we identified four markers (ATC_{dx}) which accurately distinguished malignant from benign cells. This panel was then evaluated prospectively in 47 patients (33 ovarian cancer and 14 control) and noted to maintain its excellent diagnostic performance. We show that ATC_{dx} can sensitively and specifically map ATC numbers and, through its reliable enrichment, facilitate treatment response measurements. In parallel, we developed a novel microfluidic chip platform to leverage our proteomic findings and vastly improve ATC enrichment and detection at the point-of-care. Importantly, our novel platform's small volume requirements and on-chip purification allow for rapid analyses of unprocessed ascites obviating the need for costly and laborious techniques. This proof-of-concept platform should find widespread use for broader ATC enrichment and profiling studies along the bench to bedside continuum and derive further value from otherwise discarded ascites.

4.1 Introduction

Ovarian cancer is the deadliest of gynecologic cancers with fewer than 50% of women surviving at five years following diagnosis (119). Unfortunately, this statistic has changed little over the years and most patients are still treated with a one-size-fits-all approach (120). Such a treatment strategy does not account for the broad genomic and proteomic diversity evident within ovarian tumors. Accurate measurement of detection and response protein markers would be critical to distinguishing effective from ineffective therapies. Despite the current push for biopsy-driven clinical trials, there are no minimally invasive tests or reliable biomarker panels capable of identifying ovarian cancer treatment failures before radiographic evidence of progression. The reasons are likely several-fold including heterogeneity of disease (121), variable expression levels of single biomarkers (122,123), and markers that fail to distinguish malignant from benign disease (124,125). Yet,an expanding pipeline of targeted therapies and increased appreciation for the molecular drivers within ovarian cancers have spawned a number of novel approaches for detection and treatment monitoring; these include the use of circulating tumor cells (126), tumor derived exosomes (127), stem/progenitor cells(128), soluble tumor markers (129,130), as well as the use of genomic (131,132), or proteomic information (133). Lacking, however, are practical yet highly effective point-of-care (POC) platforms that can build on this evolving science to improve upon the currently used biomarkers fraught with limited predictive utility (134).

Ovarian cancer is a peritoneal disease linked with excess fluid accumulation (ascites) that is routinely drained (paracentesis) for symptomatic relief. While often discarded, ascites provides a source of abundant clinical material (135). The precise

cellular composition of ascites tends to vary across patients, the fraction of ascites tumor cells (ATCs) is generally believed to be <0.1% of harvested cells, with the remainder being host cells (37% lymphocytes, 29% mesothelial cells, and 32% macrophages) (135). The hurdle lies in reliably identifying and isolating ATCs from their inflammatory and oftentimes hemorrhagic milieu with high potential for confounding results. Needing to process the large amounts (liters) of malignant ascites routinely collected per patient reflects another procedural step challenging clinical workflow. These factors explain, in part, why the literature on cellular profiling in ovarian cancer ascites remains limited. To help overcome these challenges, we performed targeted proteomic analyses of preclinical specimens and then prospectively in collected human ascites. We identified a four marker panel that readily detected ATCs with excellent sensitivity and specificity. In parallel, we designed a novel, all-in-one microfluidic ATC chip equipped with on-chip purification (i.e. no centrifuge needed) to meet the above mentioned challenges of clinical ascites using conventional approaches. Driven by single cell sensitivity, the chip requires only microliter amounts of unprocessed ascites. We provide proof-of-concept for an easy to operate ATC enrichment platform to promote timely diagnostic and potentially predictive molecular information. This approach is poised to expand the scientific yield of ATC and increase the reach of point-of-care microfluidic strategies into cytotoxic and/or targeted therapy ovarian cancer trials.

4.2 Material and Methods

4.2.1 Patient population and analyses

The study was approved by the Institutional Review Board (IRB), and informed consent was obtained from all subjects. Sixty-five subjects with accumulation of ascitic fluid, and requiring drainage, were enrolled in this study. Forty-six subjects carried a known diagnosis of ovarian cancer (**Table 4-1**) while nineteen subjects were included as controls (e.g. their ascites fluid was as a result of another disease such as cirrhosis or liver failure). Ascites fluid samples were collected from patients per routine in the Massachusetts General Hospital (MGH) Abdominal Imaging and Intervention suites. Two clinicians (C.M.C and R.W.), blinded to the results, reviewed all the documented clinical, imaging, and pathology data obtained from each cancer patient. **Table 4-2** summarizes the different cohorts included in the training set (n=18), validation set (n=47) and serial analyses sets (n=7).

Table 4-1. Characteristics of ovarian cancer patients (n=46).

Characteristic	Number	Percentage
Ovarian cancer patients	46	
Age		
Median	60	
Range	36-85	
Stage		
IC	1	2
IIIC	27	59
IV	18	39
Surgical Debulking		
Optimal	25	55
Suboptimal	6	13
Interval	14	30
None	1	2
Survival (ave. months from collection)		
Alive	14 (26)	30
Deceased	32 (9)	70
Chemotherapy		
Active	21	45
Not yet initiated	25	55
Platinum response		
Sensitive	18	39
Resistant	18	39
Refractory	4	9
Not applicable	6	13
Disease Course		
Response	19	41
Stable	1	2
Progression	24	52.5
Mixed	2	4.5

Table 4-2. Sample numbers of different data sets.

Data set	Definition	Malignant (n)	Benign (n)	Total (n)
Profiling	Profiling of cell lines; no primary patient samples	12	6	18
Training	Validation of markers identified in cell screens	13	5	18
Test	Prospective analysis in patient cohort	33	14	47
Complete	All above patient samples combined	46	19	65
Serial tx	Patients with repeat samples	7	NA	7

4.2.2 Cell culture

The cell lines SKOV3, OVCAR3, A2780, CaOV3, OV-90, ES-2, TOV-112D, TOV-21G, and UWB1.289 were purchased from American Type Culture Collection and grown in media following their suggested protocol. UCI 101 and UCI 107 cell lines were kindly provided by Dr. G. Scott Rose (University of California, CA, USA) and OVCA429 was kindly provided by Dr. David Spriggs (Memorial Sloan Kettering NY, USA). UCI 101, UCI 107, and OVCA429 were grown in RPMI (Cellgro) with 10% fetal bovine serum (FBS), 1% L-glutamine, and 1% penicillin/streptomycin. Mesothelial cells, LP3 and LP9, were purchased from the Corriell Institute for Medical Research and grown according to protocol. NOSE cell lines were derived from ovarian surface epithelium (OSE) brushings cultured in 1:1 Media 199:MCDB 105 (Sigma-Aldrich) with gentamicin (25 µg/ml) and 15% heat-inactivated serum. TIOSE4 and TIOSE6 cell lines were obtained from transfection of hTERT into NOSE cells maintained in 1:1 Media 199:MCDB 105 with gentamicin (25 µg/ml), 15% heat-inactivated serum, and G418 (500 µg/ml) (136). Cells were cultured under standard conditions at 37°C in a humidified incubator containing 95% room air and 5% CO_2 atmosphere. When the cells reached approximately 90% confluence, they were trypsinized to remove the cells from the culture flask. Medium was then added, the cells were spun down (300 x g for 5 minutes) and the supernatant

was removed. The cells were then fixed following the same protocol as used for clinical samples; namely Lysis/Fix buffer (BD Phosflow Lyse/Fix Buffer) was added to the cells for 10 minutes at 37°C, before being washed twice with 5 ml SB+ (phosphate buffered saline with 2% bovine serum albumin/BSA). The cells were aliquoted into tubes (~$1x10^6$ cells/ml) and stored at -20°C until labeling. The cells were then labeled following the same protocol used for clinical samples, with the exception that calretinin and CD45 antibodies were not added to each sample.

4.2.3 Bulk ascites processing for more extensive profiling

Clinically obtained ascites samples were transferred into 2 - 4 separate 225 ml conical bottom tubes (BD Falcon) and centrifuged at 300 x g for 5 minutes (Eppendorf Centrifuge 5810R). The supernatant was then removed, leaving the cell pellet undisturbed. The remaining ascites fluid was added to the tubes and the centrifugation and aspiration step was repeated until all the fluid was processed. The cell pellet in each tube was then resuspended in SB+ and transferred to a smaller 50 ml tube. The cells were spun down at 300 x g for 5 minutes and the supernatant was aspirated. After vortexing, 40 ml of pre-warmed Lysis/Fix buffer (BD Biosciences) was added and the sample was incubated on a shaker at 37°C for 10 minutes. If there were visual clumps present before the fixation step, collagenase (Sigma Aldrich) was added at 0.2 mg/ml in PBS and the sample incubated on a shaker for 30 - 60 minutes at 37°C. The cells were then washed with SB+ before proceeding to the lysis/fix step (described above). After the lysis/fix step, the cells were centrifuged at 400 x g for 3 minutes and the supernatant

was removed. This was followed by two washes with 5 ml of SB+. The supernatant was removed after the final wash and the cells were resuspended in 1 ml of SB+.

4.2.4 CD45 Purification Step

Cells were counted with the Countess™ Cell Counter (Life Technologies) and adjusted to a concentration of approximately 2 x 10^7 cells/ml. CD45 antibody (Biolegend, H130) was added (0.5 µl/10^6 cells) and incubated for 1 hour, before washing twice with 5 ml SB+. The supernatant was removed and Anti-Mouse IgG1 magnetic beads (80 µl per 10^7 cells , Miltenyi Biotec) were added along with SB+ (20 µl per 10^7 cells). The reaction was incubated for 15 minutes at 4°C and was followed by two washes (2 ml per 10^7 cells) with SB+. The remaining sample was then resuspended in 1 ml of SB+. Magnetic separation columns (LS, Miltenyi Biotec) and the QuadroMACS separator were used for negative selection following suggested protocols. Pre-separation filters (Miltenyi Biotec) were used to remove any clumps or debris from the clinical specimens to prevent obstruction of the column. The maximum amount of cells used in each column was 1x10^8. The sample was added to the column and was washed three times with 3 ml of SB+. The CD45- cells that passed through the column were subsequently collected into a 15 ml tube and centrifuged (400 x g, 3 minutes); the supernatant was removed and the cells were resuspended in SB+. Cells were then counted and aliquoted into tubes at approximately ~1x10^6 cells/ml, before being stored at -20°C until labeling.

4.2.5 Cell Labeling

CD45 depleted cells stored in the -20°C freezer were thawed. The cells were then centrifuged at 400 x g for 3 minutes and the supernatant removed. Perm buffer (PW+: BD perm/wash with 2% BSA), was added and the cells were aliquoted into cluster tubes (Costar). The appropriate antibody mixture of calretinin and CD45 was added (See **Appendix A**; calretinin: Mouse Dako DAK-Calret 1 or Rabbit Invitrogen DC8; CD45: Rat Abcam YTH24.5 or Mouse Biolegend H130). The specific antibody for the biomarker of interest was then added (**Appendix A**). The final reaction volume was 150 µl. This primary reaction was vortexed and incubated for 1 hour before 0.5 ml PW+ was added to each sample and the cells spun down at 400 x g for 3 minutes. The supernatant was removed and the cells vortexed and washed with 0.5 ml PW+. After centrifugation (400 x g, 3 minutes), the supernatant was aspirated and the appropriate secondary antibodies were added (**Appendix A;** Anti-Mouse FITC Abcam (1:300); Anti-Rabbit APC Abcam (1:300); Anti-Rat PeCY7 Biolegend (1:300)). The final reaction volume was 150 µl. The samples were vortexed and incubated on ice for 1 hour. Cells were then washed twice with 0.5 ml PW+. Samples analyzed by flow cytometry the same day were kept on ice under aluminum foil. Samples run the following day were lightly fixed (BD Phosflow Fix Buffer (1:2)) for 10 minutes at 37°C and then washed with SB+. After washing, DAPI was added to the samples at a ratio of 1:500 (Fxcycle stain, Invitrogen) 30 minutes before analysis by flow cytometry. Antibody information (such as clone and company) for all markers is included in **Appendix A**.

4.2.6 Flow Cytometry

Fluorescently labeled samples were analyzed using an LSRII flow cytometer (Becton Dickinson). FlowJo software was used to gate on: singlets using DAPI staining, then Calret+, CD45+, and CD45-/Calret- cell populations in the clinical samples. The mean fluorescent intensity (MFI) for each marker of interest was then determined for each of these three populations. The background was determined by staining with the secondary antibody only (no primary). The signal-over-background was then calculated (λ= Signal/Background-1) and plotted in the heat maps using GENE-E software (Broad Institute). Each marker was placed into 4 categories on the following criteria: 1) 'Unique Malignant' (if an ovarian cancer sample had λ>1.5 and all benign samples had λ< 1.5); 2) 'Ubiquitous' (if an ovarian cancer sample and a benign sample had λ>1.5); 3) 'Benign' (if both an ovarian cancer sample and benign sample had λ<1.5); and 4) 'Absent' (if both ovarian cancer and benign samples had $\lambda \leqq 1.5$). Heatmaps of clinical samples were plotted on a log scale and grey signifies data that was not determined.

4.2.7 Statistical analysis

Receiver operating characteristic (ROC) curves were constructed for the five most highly expressed cancer markers relative to benign mesothelial cells: EpCAM, CA19-9, CD24, CD56, and TAG-72 in the training set (**Figure 4-1**). For each marker sensitivity versus (1 − specificity) was plotted and the values of area under the curve (AUC) were computed using the trapezoidal rule. The empirical ROC curves were smoothed by applying the binormal fitting model. An AUC of 0.5 was used to indicate that the test shows no difference between the two groups, whereas an AUC of 1.0 was

used to indicate that the test gives a perfect separation between the groups. We defined the optimal cutoff value for identifying malignant status as the point on the ROC curve with the minimal distance between the 0% false-negative and the 100% true-positive rate. Statistical analysis was performed using the R-package (version 3.0.1). Using standard formulas, we calculated sensitivity, specificity, and accuracy.

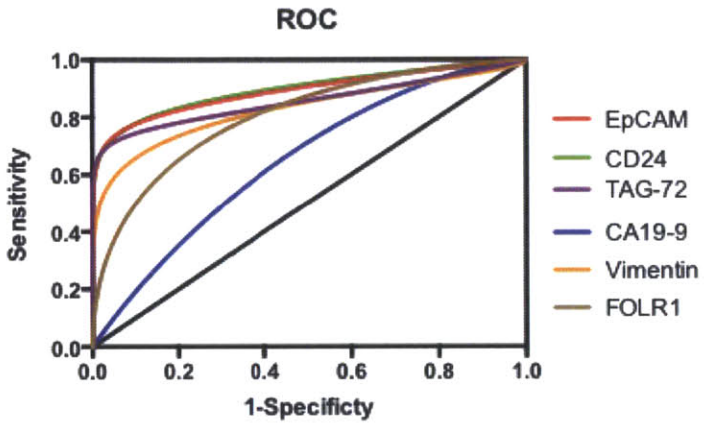

Markers	AUC	Optimal Cutoff level	SE	95% CL
EpCAM	0.92	0.40	0.074	0.778 to 1.068
CA19-9	0.59	1.57	0.121	0.355 to 0.828
CD24	0.92	0.81	0.074	0.778 to 1.068
TAG-72	0.82	0.49	0.096	0.635 to 1.010
FOLR1	0.75	1.65	0.099	0.551 to 0.940
Vimentin	0.86	2.20	0.078	0.705 to 1.011

Figure 4-1. ROC analyses of training set. ROC curves were plotted for individual markers using the 13 OvCA and 13 benign samples of the training set (top). The area under the curve (AUC) and the optimal cutoff level were calculated and are summarized in the bottom table. The cutoff values were then used to determine the sensitivity, specificity, accuracy of each individual marker and the V3 and ATC_{dx} panel.

4.2.8 ATC device fabrication

Microfluidic single cell capture arrays were fabricated in polydimethylsiloxane (PDMS; Dow Corning) using soft lithography (39,137). The microfluidic device was designed to contain approximately 5,000 capture sites ranging in size from 15-40 μm (**Figure 4-2**). Three layers of epoxy-based photoresist were patterned on 4" silicon wafers as a mold using conventional photolithography. The first SU8 2015 (Microchem) layer defined a 15 μm gap height in the capture sites for the 15 and 20 μm cells. Before developing unexposed SU8, the second SU8 2015 layer was coated and aligned to the channel structure for the 15 and 20 μm cell capture sites. This layer also defined the gap height (30 μm) for the 30 and 40 μm cell capture sites. Finally, another 30 μm-thick SU8 2025 was applied for the 30 and 40 μm cell capture structures. All unexposed SU8 photoresist layers were then developed in the SU8 Developer (Microchem). The mold with the channel and cell capture patterns was silanized with a vapor of trimethylchlorosilane (TMCS, Sigma), and was cast with 3 mm-thick PDMS prepolymer. After curing, the PDMS layer was peeled off and an inlet and an outlet were punched out. The prepared PDMS chip was then bonded (not permanently) to a glass slide. The chip thus remained detachable for easy recovery of cells after purification and imaging to enable further molecular profiling of cells.

A

Total Capture Sites	4925
Dimension of 40 µm Capture Sites	# of capture sites: 495 L = 580 W_1 = 60 H_1 = 60 L_1 = 100 W_2 = 60 H_2 = 30 L_2 = 5 W_3 = 120 L_3 = 60 W_4 = 40
Dimension of 30 µm Capture Sites	# of capture sites: 1190 L = 480 W_1 = 45 H_1 = 60 L_1 = 100 W_2 = 50 H_2 = 30 L_2 = 10 W_3 = 100 L_3 = 40 W_4 = 25
Dimension of 20 µm Capture Sites	# of capture sites: 1490 L = 430 W_1 = 35 H_1 = 30 L_1 = 100 W_2 = 40 H_2 = 15 L_2 = 10 W_3 = 40 L_3 = 30 W_4 = 20
Dimension of 15 µm Capture Sites	# of capture sites: 1750 L = 340 W_1 = 25 H_1 = 30 L_1 = 100 W_2 = 25 H_2 = 15 L_2 = 5 W_3 = 50 L_3 = 20 W_4 = 7

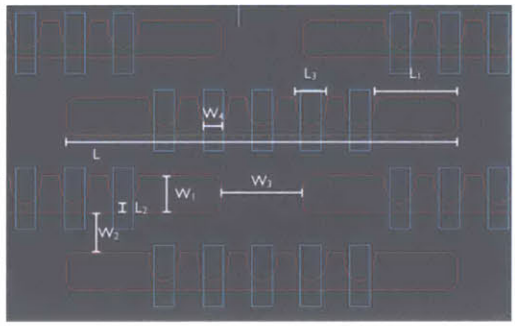

B

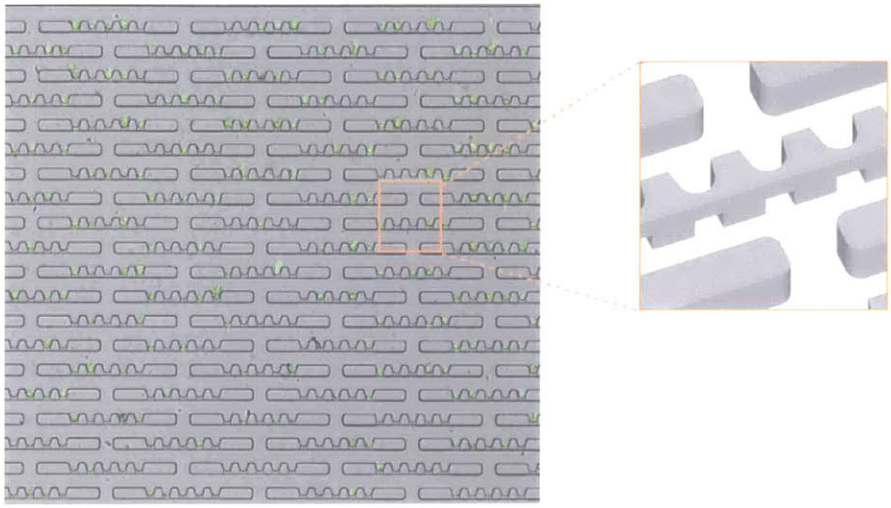

Figure 4-2. ATC chip design and measurements. (A) The layout of the ATC chip with 4 differently sized wells (n = 4,925) for cell capture. (B) An example of captured cells (green represents DAPI staining) on micro-wells.

4.2.9 Processing cells through the ATC chip

For on-chip enrichment and staining of ATCs, approximately 100 µl of ascites fluid was added to the inlet of the chip (**Figure 4-3 A**). Then an antibody cocktail of the following antibody conjugates was added: Calretinin-Biotin (Invitrogen, Rabbit), CD45-Biotin (Abcam, Rabbit), EpCAM-FITC (Dako, Mouse), Vimentin-RITC (Abcam,Mouse). This cocktail was incubated for 15 minutes. Then streptavidin-coated magnetic particles (R&D) and Anti-Rabbit Dylight 650 (Abcam) were added followed by a 15 minute incubation (**Figure 4-3 B**). A magnet was then placed under the inlet and the non-magnetically labeled cells were passed through the microchip (**FIgure 4-3 C**). Three

washes of 100 µl SB+ with DAPI (4',6-diamidino-2-phenylindole; Invitrogen, 1:500) were then passed through the microchip. Captured ATCs were imaged using the DeltaVision screening system (Applied Precision Instruments) and analyzed using ImageJ software (version 10.2) (**Figure 4-3 D**).

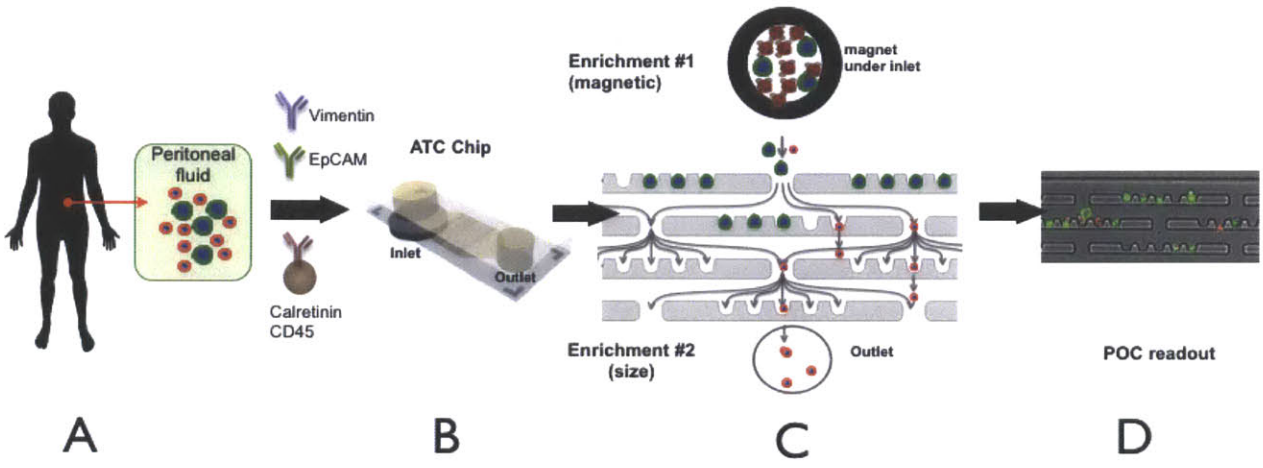

Figure 4-3. Schematic of on-chip purification and labeling. (A) First, ascites fluid is collected from the patient which contains malignant cells amongst aninflammatory milieu of host cells. (B) Ascites cells are added to the chip followed by an antibody cocktail (calretinin-Biotin, CD45-Biotin, EpCAM-FITC, Vimentin-RITC). Then streptavidin-coated magnetic particles and Anti-Rabbit Dylight 650 bind to the rabbit biotinylated calretinin and CD45 antibodies. (C) A magnet under the inlet allows the non-magnetically labeled malignant cells to pass freely through the microchip while the benign cells are bound to the magnet. The four different size microwells (40, 30, 20,15 um) allow for capture of the malignant cells while allowing for the typically smaller leukocytes to pass through the device. (D) The ATCdx signature (EpCAM+ and/or Vimentin+/Calretinin-/CD45-) can then be imaged to determine number of ATCs.

4.3 Results and Discussion

4.3.1 Experimental approach

Figure 4-4 summarizes the experimental approach. Initially, we began by surveying the literature (128,138-146) and scientific databases (147) to identify subsets of putative diagnostic markers of ovarian cancer, mesothelial, and other host cells, as well as mechanistic markers of treatment response (139,140,148,149).

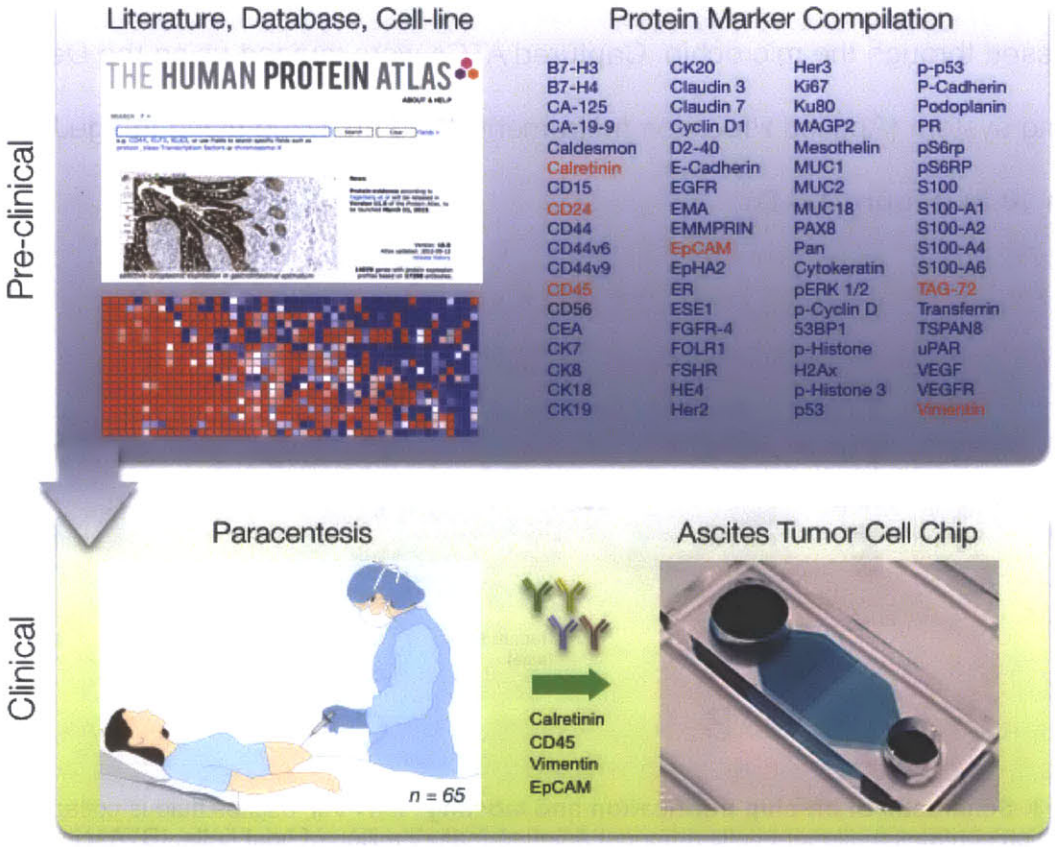

Figure 4-4. Schematic approach. A total of 85 putative ovarian cancer protein markers were identified through literature, database and other screens (top left). Markers were tested in 12 ovarian cell lines (**Figure 4-5**) and a subset examined in ascites from human patients (**bottom left; n=65; Figure 4-6 and 4-7**). A microfluidic chip (**Figure 4-3**) was developed for point-of-care analysis (bottom right).

A total of 85 commercially available and validated antibodies were selected and tested in 12 ovarian cancer cell lines (OV-90, OVCAR3, SKOV3, ES2, OVCA429, CaOV3, UC101, UC107, TOV21G, TOV112D, A2780), two mesothelial cell lines (LP9, LP3), two benign ovarian cell lines (TIOSE4,TIOSE6), and in lymphocytes and neutrophils (**Figure 4-5**). From this data, 31 markers were identified and profiled in a training set of human ascites collected under an Institutional Review Board (IRB) approved protocol (**Figure 4-6**). Based on these findings, we then sought to establish a reliable and manageable protein marker panel that could be adapted to POC diagnostic

testing via microfluidic devices, such as the ATC chip described here. Altogether, we accrued a patient cohort involving 65 patients (n=46 OvCA (**Table 4-1**), n=19 benign) of which 18 samples were used in a training set and 47 samples were used in a test set (**Table 4-2**). In addition, serial samplings were feasibly obtained on a subset of patients (n=7) following therapy; those temporal samples were not included in the training or test portions of the study. Control samples included ascites collected from patients with end-stage liver disease or advanced heart failure without known malignancy.

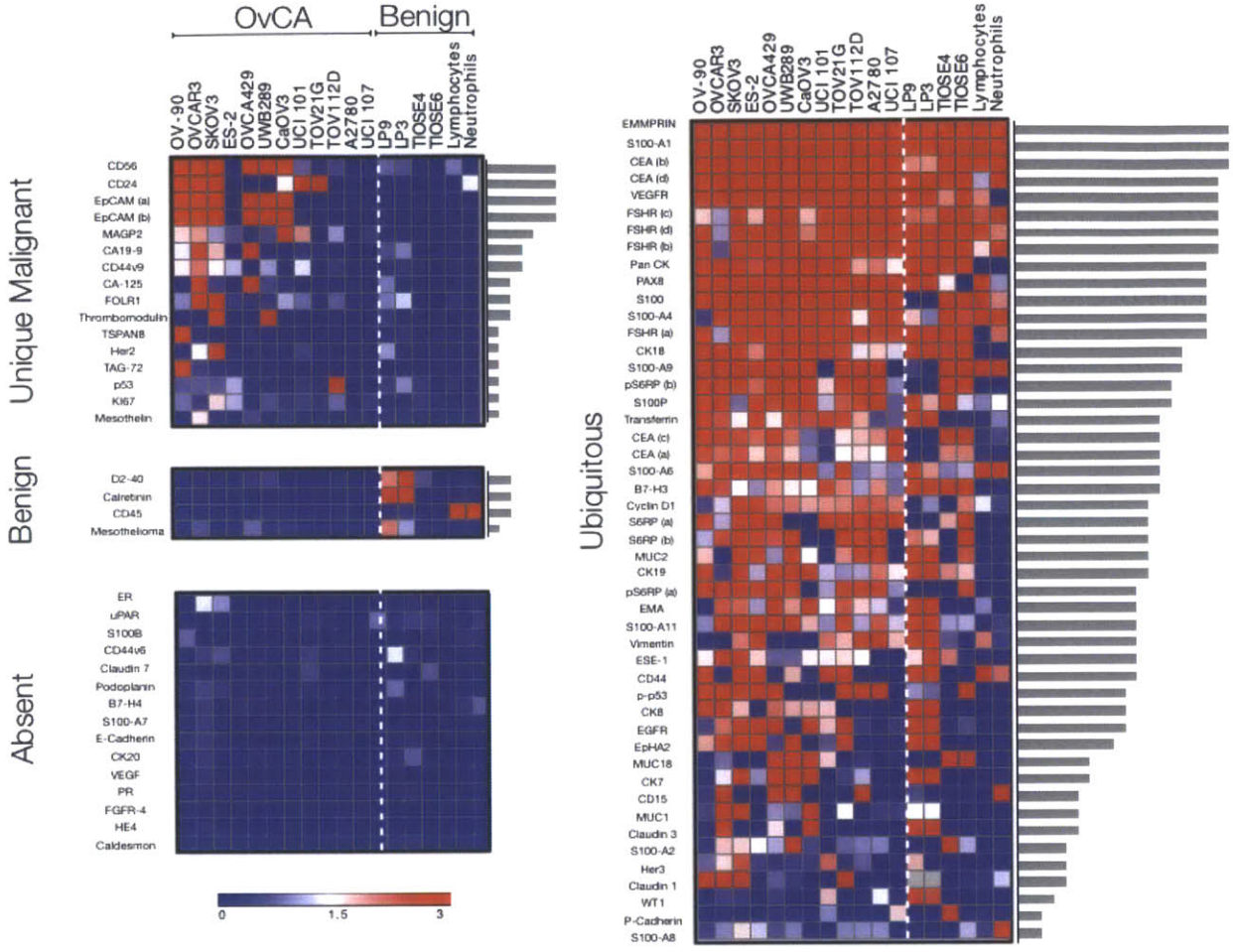

Figure 4-5. Profiling of cancer cell lines. Twelve different ovarian cancer (OvCA) cell lines, and six benign cell lines (two mesothelial cell lines (LP9, LP3); two benign ovarian cell lines (TIOSE4,TIOSE6); primary human lymphocytes/neutrophils) were tested for their expression levels (λ=signal/background-1) of putative diagnostic protein markers using flow cytometry. For each marker the frequency of cell lines with λ >1.5 (red) are shown on right hand side of the heat map (grey bar) and are rank-ordered by abundance. The data is categorized into 4 subgroups: i) markers present in malignant cells (Unique Malignant; top left), ii) markers in malignant and benign cells (Ubiquitous, right), iii) markers in benign cells only (Benign; middle left), and iv) markers absent in both cell types (Absent; bottom left). This dataset was used to identify markers for subsequent analysis of primary human samples (**Figure 4-6**). Parenthesis represents different antibodies used for the same marker (**Appendix A**). The CD56 antibody (clone MOC-31) used in this screening was found to cross react with EpCAM and therefore was not used in clinical sample profiling.

4.3.2 Unique marker expression in a training set of human ascites samples

The training set consisted of 19 clinical patients (13 ovarian cancer, 6 non-ovarian cancer). First, the samples were purified from CD45 positive cells using magnetic separation. Then multicolor flow cytometry was performed to determine marker expression levels in calretinin positive mesothelial cells (138) and calretinin/ CD45 negative cells (**Figure 4-6 A**). Markers were categorized into four general subgroups based on expression levels: i) markers unique to malignant cells; ii) markers present in malignant and benign cells; iii) markers present in benign cells only; and iv) markers with low expression levels in either cell type (**Figure 4-6 B**, see Methods for details). The clinical performance of the markers were determined by performing receiver operating characteristic (ROC) analyses (**Figure 4-1**). The ROC curves were used to calculate optimal cutoff values for individual markers and subsequently the sensitivity, specificity, and accuracy for each marker.

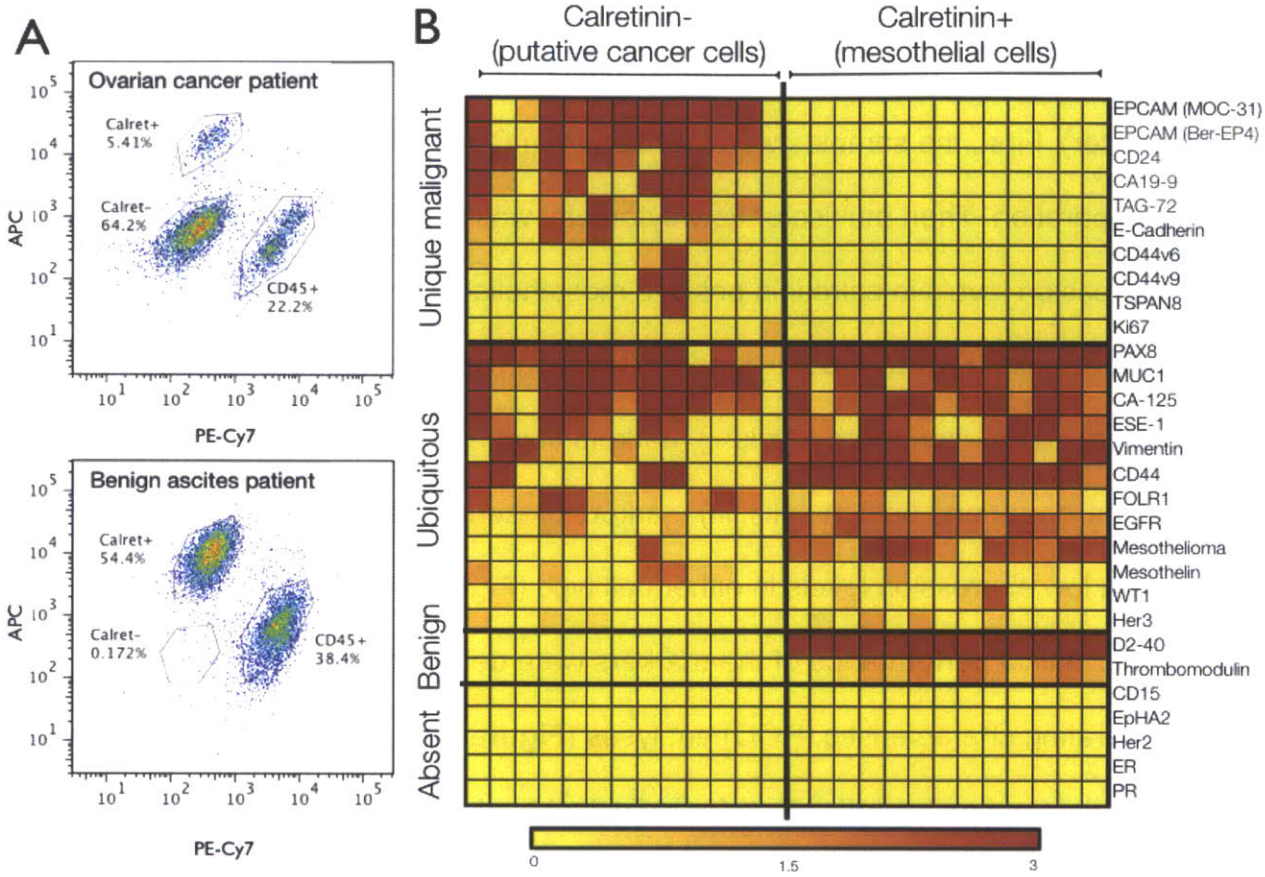

Figure 4-6. Profiling of primary human samples in training set. (A) Multicolor flow cytometry was used for gating of mesothelial (calretinin+), leukocytes (CD45+), and CD45/Calret- cells. (B) A subgroup of 31 markers identified in the cell line screen (**Figure 4-5**) were subsequently tested in a training set (n=19). The data are rank-ordered by abundance (yellow = lowest; red = highest). The markers were placed into four different categories: unique malignant, overlapping markers (Ubiquitous), benign, and absent using cutoffs described in the methods section. The three OvCA patients with lowest EpCAM expression levels had the highest vimentin expression levels suggestive of epithelial to mesenchymal transition (EMT). This training set led to identification of the ATC_{dx} panel where malignancy is defined by either having an EpCAM+ and/or V3+ (Vimentin+/Calretinin-/CD45-) signature. Heatmap values are the log ratio of the fluorescent signal over the ctrl (λ=Sig/Ctrl-1) where the ctrl is the secondary antibody without the primary antibody.

The markers unique to cancer cells with the highest sensitivity were EpCAM, CA19-9, CD24, and TAG-72 (**Table 4-3**). Markers that were non-specific and expressed in both cancer and mesothelial cells included vimentin, MUC1, CD44, CA-125, FOLR1, WT1 and EGFR. Markers unique to mesothelial cells included D2-40, and thrombomodulin. Noteworthy was the low sensitivity of FOLR1 (69.2%) and CA-125 (53.8%). FOLR1 has been often cited in literature as a promising therapeutic target

(150,151) and CA-125 is the most frequently used biomarker for ovarian cancer detection (152). Also of note, the three ovarian cancer patients with the lowest EpCAM expression level had the highest vimentin levels suggestive of epithelial to mesenchymal transition (EMT); their median survival was 5 months (range 1-8 months). It is thought that during EMT, epithelial cancer cells undergo biochemical changes resulting in a mesenchymal cell phenotype which enhances migratory capacity, invasiveness, and resistance to apoptosis (97,153). Coupling current understanding of EMT (154) with our training set profiling data allowed us to identify an ascites-derived tumor signature termed ATC_{dx} referring to cells that are either EpCAM+ and/or V3 positive (Vimentin+/Calretinin-/CD45-). This ATC_{dx} panel had higher sensitivity, specificity, and accuracy then any individual marker alone and was able to correctly identify all 13 ovarian cancer samples in the training set (**Table 4-3**).

Table 4-3. Sensitivity, specificity, and accuracy of different protein markers in the training set.

Markers	Sensitivity(%)	Specificity(%)	Accuracy (%)
EpCAM	92.3	100.0	96.9
CA19-9	46.2	100.0	78.1
CD24	92.3	94.7	93.8
TAG-72	76.9	100.0	90.6
FOLR1	69.2	78.9	75.0
V3 panel: (Vim+/Calret-/CD45-)	23.1	100.0	68.8
ATC_{dx} (EpCAM+ and/or V3+)	100.0	100.0	100.0

4.3.3 Prospective ATC profiling in a test set of human ascites samples

After identifying a promising ATC marker signature (ATC_{dx}), we subsequently investigated its diagnostic performance in a blinded prospective study (**Figure 4-7**). Using a test set of 47 patients (n=33 OvCA, n=14 benign), we were able to demonstrate high sensitivity and specificity using ATC_{dx}. Namely, the presence or absence of ATC_{dx} correctly identified all 33 ovarian cancer patients and all 14 benign ascites samples (**Figure 4-7 A**). In patients with sufficient cell numbers, the five markers with the highest sensitivity in the training set were evaluated in the test set. The cutoff values determined from ROC analyses (**Figure 4.1**) in the training set were applied to the test set (**Figure 4-7 B**). The sensitivity, specificity, and accuracy of these individual markers were determined (**Table 4-4**) where EpCAM had the highest sensitivity (93.9%) and accuracy (95.7%) followed by CD24 (sensitivity=85.7%, accuracy=94.9%). Adding V3 (Vimentin+/Calretinin-/CD45-) to EpCAM (ATC_{dx} panel) increased sensitivity and accuracy to 100%.

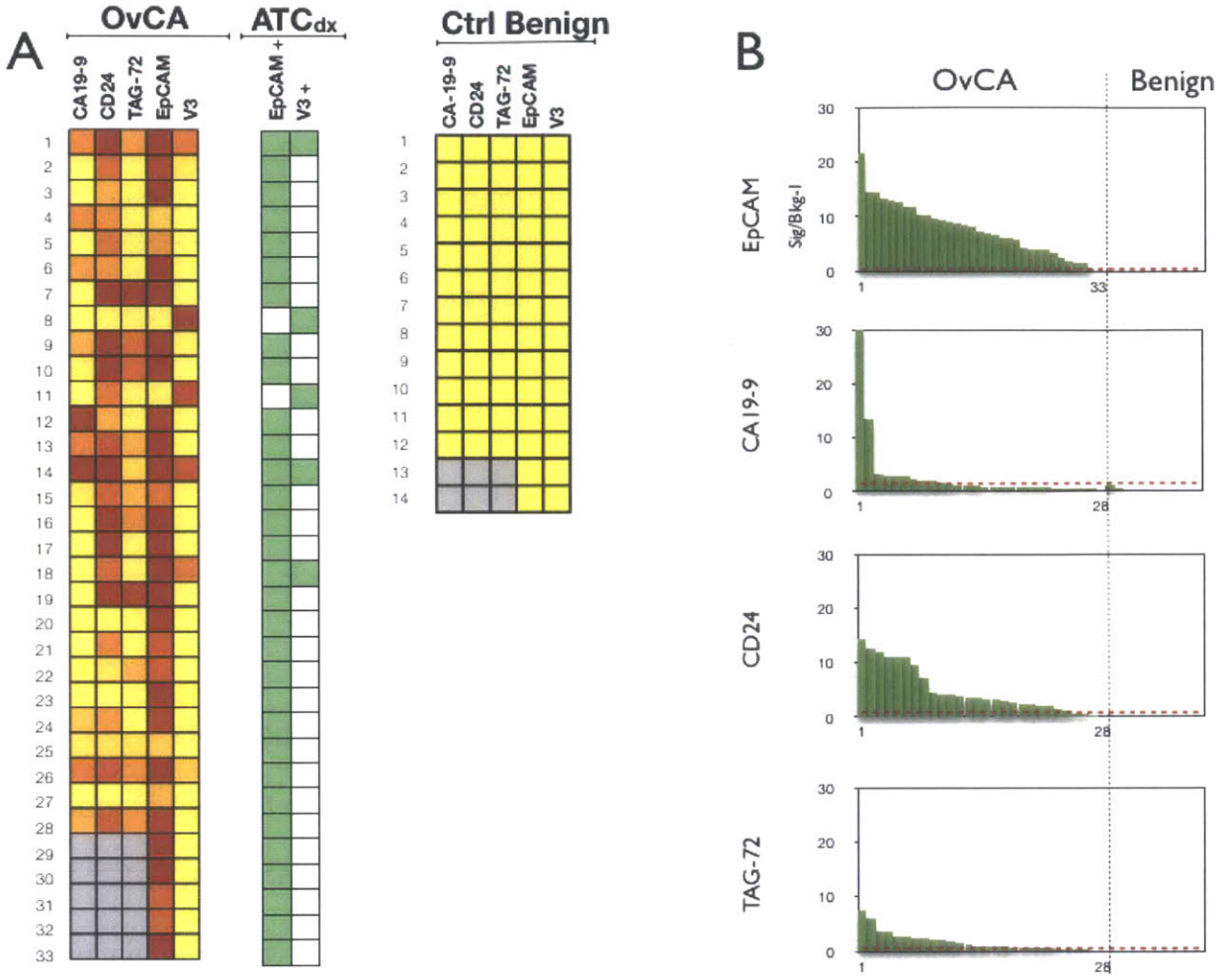

Figure 4-7. Prospective testing of ATC marker panels in 47 patients. (A) Ascites samples were tested for the presence of 6 individual markers in 33 ovarian cancer patients (left) and 14 controls (right). EpCAM alone was positive in 31 samples. By using the V3 marker set (Vimentin+/Calretinin-/CD45-) and EpCAM together (ATC_{dx}), all 33 samples were correctly identified (green heat map). ATCs were identified in malignant samples, but not in benign, samples. Grey squares represent data not measured due to insufficient number of cells for flow cytometry. Color scale is same as Fig. 3. (B) Waterfall plots of the individual markers profiled in the test set. Dotted red lines represent the optimal threshold values determined from ROC analyses performed on the training set.

Table 4-4. Sensitivity, specificity, and accuracy of different protein markers.

Validation set (n = 47)						
Marker	**EpCAM**	**CA19-9**	**CD24**	**TAG-72**	**V3**	**ATCdx**
Sensitivity	93.9	35.7	85.7	78.6	15.6	100.0
Specificity	100.0	100.0	100.0	100.0	100.0	100.0
Accuracy	95.7	53.8	89.7	84.6	41.3	100.0

4.3.4 Serial testing to measure treatment response in individual patients

A major application of our POC approach would be to leverage the use of readily accessible (but otherwise discarded) ascites as an abundant source of ATCs for treatment monitoring through serial analyses. **Figure 4-8** exemplifies this potential using ascites collected and profiled from a single patient over a 14 week treatment period. The patient was initially treated with cytotoxic agents (Carboplatin and Paclitaxel; weeks 2 and 5) but was transitioned to anti-angiogenic therapy (Bevazucimab/Avastin®; week 7) due to disease progression. ATC numbers were initially observed to decrease steadily during treatment response, only to increase when disease progression occurred. Avastin attenuated the increase in ATC burden concurrent with patient's improved clinical symptoms.

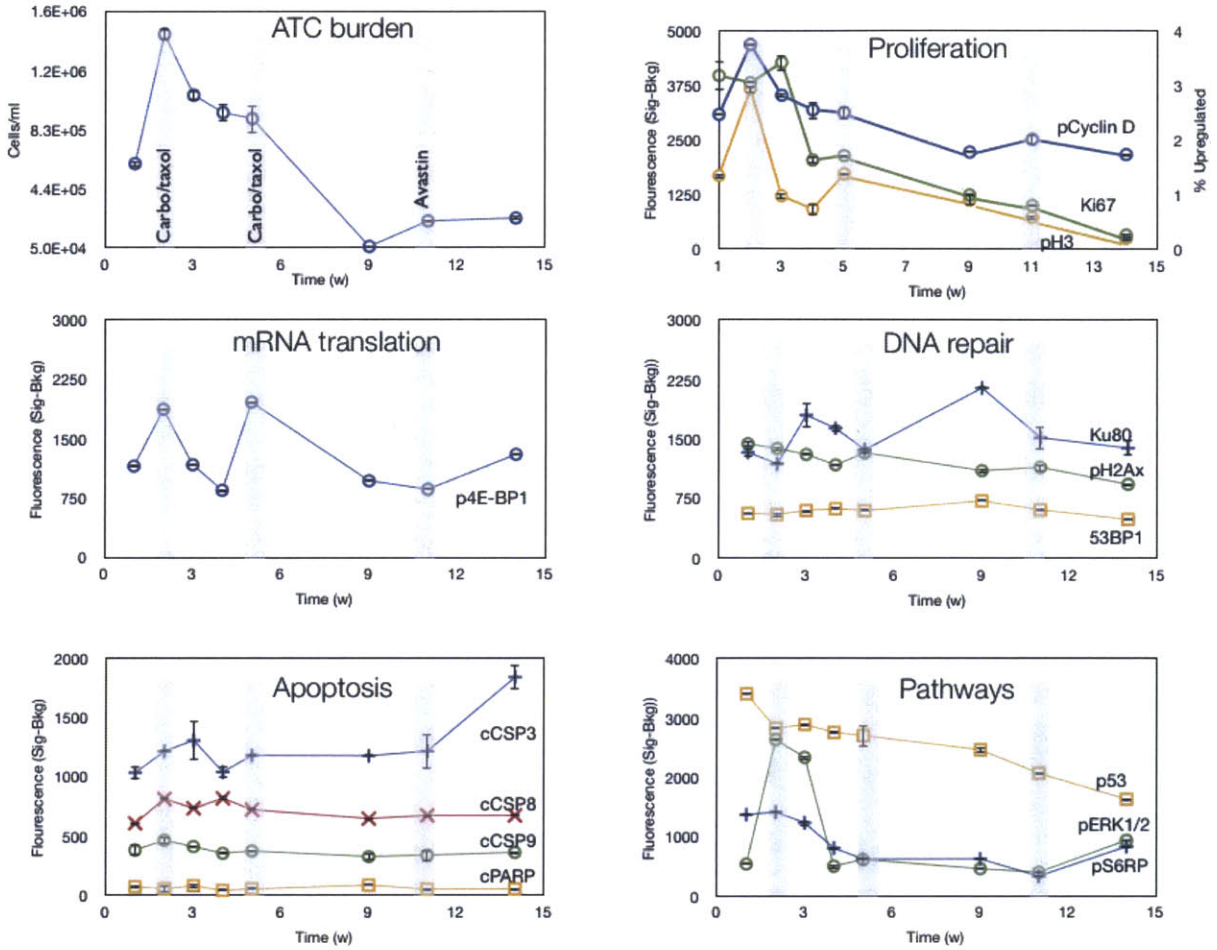

Figure 4-8. Serial analysis of ATCs. ATCs were obtained serially from a single patient over a 14 week treatment cycle. Carboplatin and Paclitaxel (Taxol®) were given in weeks 2 and 5, and Bevazucimab (Avastin®) was given in week 11. The number of ATCs were measured over the course of treatment (ATC burden) using ATCdx. Additionally, protein markers related to biological processes such as proliferation (Ki67, pH3, pCyclinD), mRNA translation (p4E-BP1), DNA repair (Ku80, pH2Ax, 53BP1) apoptosis (cleaved CASP3, cleaved CASP8, cleaved CASP9, cleaved PARP) and pathway inhibition (pS6RP, p53, pERK) were also measured. This demonstrates that molecular profiling of ascites can be used as a tool to monitor treatment response over the course of therapy. All samples were stained with DAPI, Calretinin, and CD45 antibodies and gated to exclude doublets, mesothelial cells, and leukocytes respectively. Data are expressed as the average of the mean fluorescent intensity +/- SEM.

ATC analysis could also be used for early detection of treatment response through the profiling of protein markers related to biological processes such as apoptosis (cleaved CASP3, cleaved CASP8, cleaved CASP9, cleaved PARP), proliferation (Ki67, pH3, pCyclinD), DNA repair (Ku80, pH2Ax, 53BP1), mRNA translation (p4E-BP1) and/or pathway inhibition (pS6RP, p53, pERK). As expected, the

proliferation markers Ki67, pH3, and pCyclinD had a decreasing trend matching that of the ATC numbers. After each Carboplatin/Taxol administration, the levels of the growth pathway markers p4E-BP1, pERK, and pS6RP were reduced and stable, but upon switching to single agent Avastin, the levels of these markers increased. In this clinical example, the data suggests that resuming cytotoxic therapy (which had maintained pathway inhibition) alongside Avastin treatment might have attenuated the patient's eventual clinical decline. Indeed, recent late-phase clinical trial data have reported progression-free survival advantages when cytotoxic and antiangiogenic strategies are combined in ovarian cancer (155).

4.3.5 Differentiating responders from non-responders

Using an expanded set of mechanistic markers (**Figure 4-9**), we compared the profiles of treatment responders with non-responders (based on tumor burden, as determined by imaging or clinical course; **Table1**). The panels indicate that the two groups could be readily distinguished based on ATC molecular profiles. Moreover, these profiles could be potentially useful for providing additional biological insight into the drivers of treatment response or disease progression. For example, unlike in treatment responders, levels of pS6RP and p4E-BP1 (readouts of the phosphatidylinositol 3 / PI3 kinase pathway) remained elevated after therapy in the non-responders. This is consistent with previous findings that have associated activated PI3 kinase signaling with chemoresistance in advanced ovarian cancer (156).

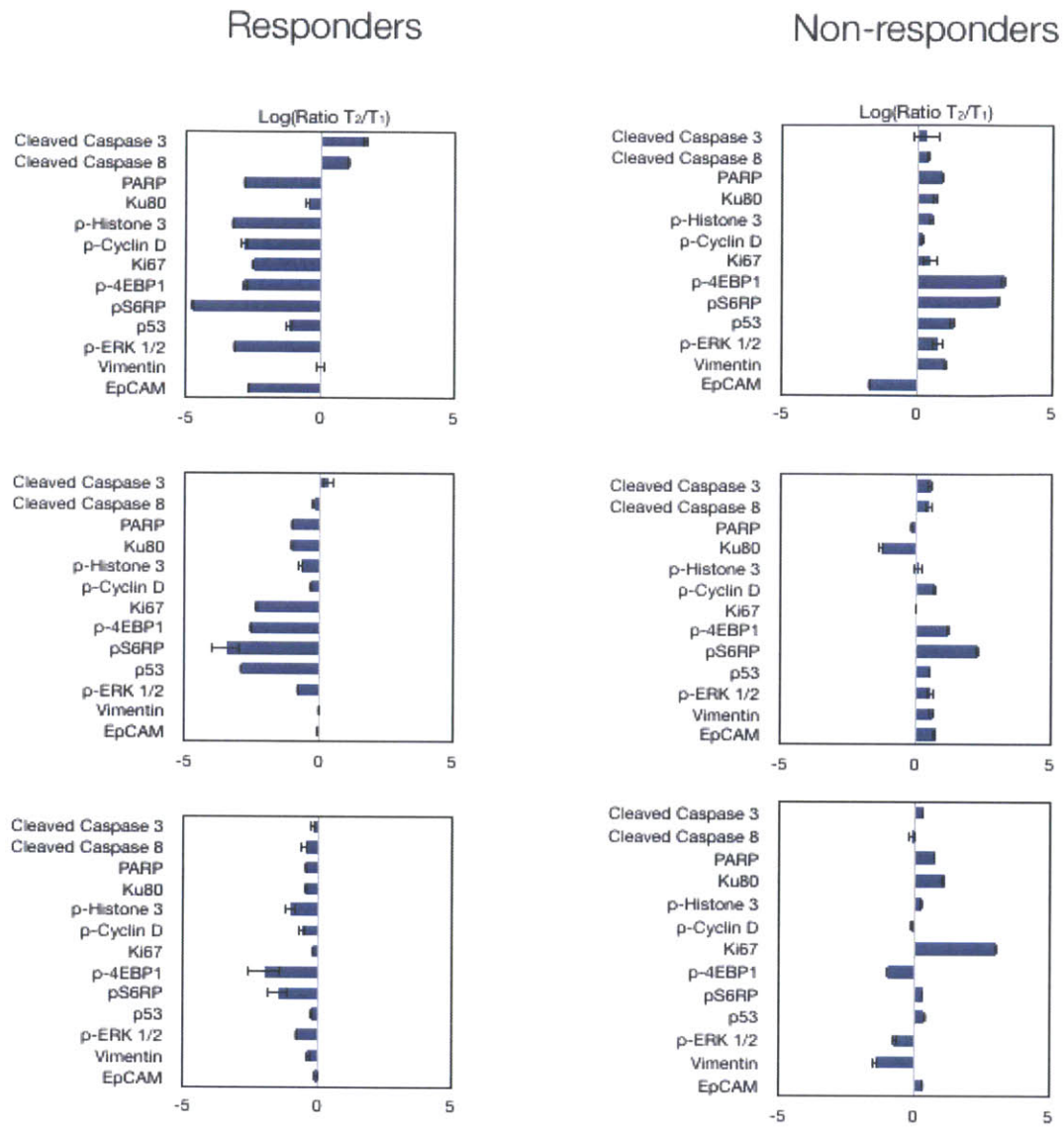

Figure 4-9. Predictive ATC markers of treatment response. Key treatment response markers are plotted for 6 patients who were analyzed serially and either responded to treatment (left) or progressed (right). Responders typically have proliferation (Ki67, pH3, pCyclinD), mRNA translation (p4E-BP1) and protein translation (pS6RP) markers downregulated compared to the non-responders. Each marker was measured in duplicate for each time point and the error bars represent the SE.

4.3.6 Ascites specimen cellular composition

The total cell and ATC count in ascites specimens was determined for each of the 65 patients (n=46 OvCA, n=19 Ctrl, **Figure 4-10**). The mean total cell number (host cells and ATCs) for the 65 patients was $1.2x10^5$ cells/ml (median: $4.1x10^4$; range: $3x10^3$ to

$1.5x10^6$; SEM: $2.7x10^4$) and similar (p-value>0.05) in both the 46 OvCA (mean: $1.5x10^5$, median: $6.8x10^4$, range: $1.6x10^3$ to $1.5x10^6$, SEM: $3.5x10^4$) and 19 control samples (mean: $6.7x10^4$, median: $3.2x10^4$, range: $3.1x10^3$ to $5x10^5$, SEM: $2.6x10^4$). ATCs were identified in all 46 ovarian cancer patients (mean: $2.7x10^4$, median: $2x10^3$, range: $1.5x10^1$ to $6x10^5$; SEM: $1.4x10^4$). The relative ATC abundance values informed us of the diagnostic and enrichment needs of a POC microfluidic diagnostic system (e.g. in 30% of patient samples, ATCs made up <1% of the total cell population).

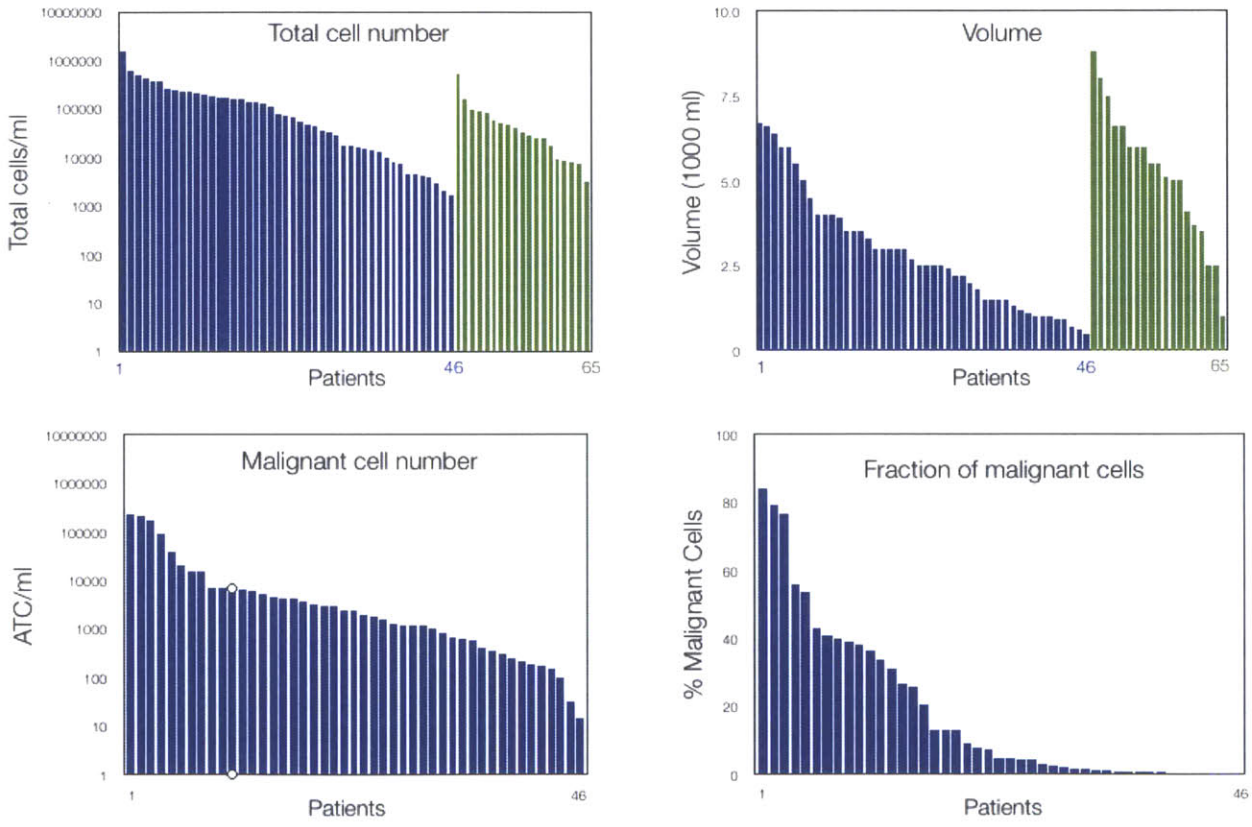

Figure 4-10. Ascites cellular composition and volume. Ascites samples from 65 patients with (blue; n=46) or without (green; n=19) ovarian cancer were analyzed for total cell number (top left), malignant cell number (bottom left; ATCs), cell volume (top right) and fraction of malignant cells compared to total cells (bottom right). Viable cells were counted using trypan blue staining and the Countess cell counter (Invitrogen). Malignant cell number were determined using ATCdx via flow cytometry. Data are plotted as waterfall plots.

4.3.7 ATC enrichment and detection using a point-of-care microfluidic chip

Not unlike clinical reality, many of the ascites samples contained large clumps and extracellular debris. The device was therefore designed with a miniature filter (70 μm) at the inlet to prevent downstream clogging and capture sites descending in size from 40 to 15 μm (**Figure 4-11 A**). The differently sized capture sites were designed to take into account the heterogeneity of ATC size. Typically, the 40 μm microwells captured clusters of cells whereas single cells were captured in the 20 and 15 μm sized microwells. This facilitated easy visualization of the differently sized cell populations.The microfluidic chip was designed to enrich ATCs through negative selection of host cells (**Figure 4-2**). Notably, benign cells are labeled with magnetic particles and captured or anchored into place by a magnet situated under the device inlet. A second separation is performed based on cell size where the relatively larger ATCs are captured by the differently sized microwells (ranging from 15-40 μm) while the smaller unencumbered leukocytes pass through the chip. This two step on-chip purification approach yielded an approximate 60-fold ATC enrichment.

The ATC chip was intentionally designed to be optically transparent so that cells captured in micro-wells can be stained on-chip and visualized with a charge-coupled device (CCD) or microscope setup. **Figure 4-11** illustrates a representative example of ATC_{dx} based staining of ATCs (green), and CD45/Calretinin staining of mesothelial and host cell staining (red). Compared to conventional flow cytometry needs (~10,000 cells), the ATC chip affords reduced sample size requirements due to its single cell detection capabilities. For example, an ovarian cancer patient harboring 15 ATCs/ml, would require > 0.5 L of ascites processing for flow cytometry compared to only ~100 μl for on-

chip processing. Moreover, this microfluidic chip is easily fabricated using soft lithographic techniques (39,137) with very inexpensive materials such as PDMS, providing a practical and affordable alternative to flow cytometry.

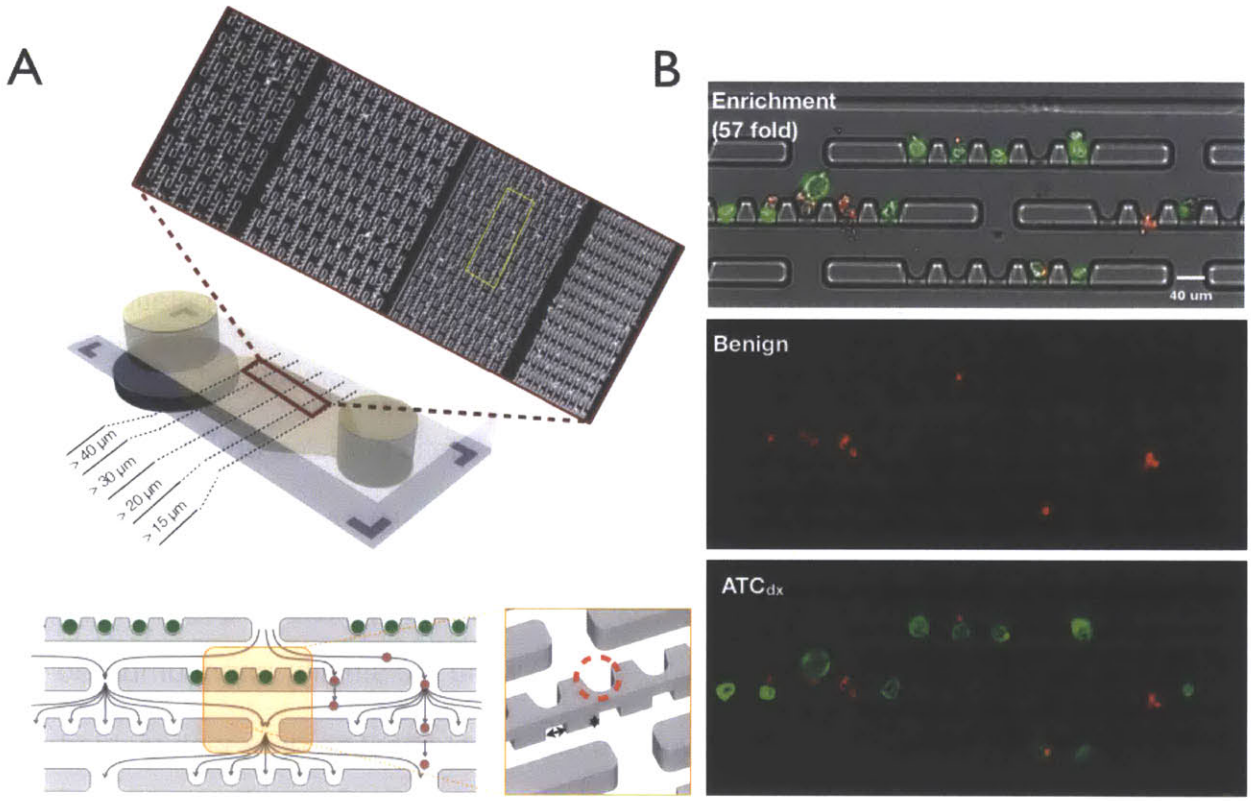

Figure 4-11. Design of microfluidic chip for ATC analysis. (A) A microfluidic chip, containing multiple and differently sized cell capture scaffolds, was designed for high fluid throughput (see **Figure 4-1** for details). The chip was designed to be optically transparent so that staining could be performed directly on-chip. (B) Using this device, ATCs were enriched by 57-fold, and each well was capable of capturing either one cell or clusters of cells. Staining for EpCAM (green) and CD45/Calretinin (red) for benign host cells is shown. ATCs appear larger and do not overlap with host cells.

4.4 Conclusions

Three objectives motivated this study: 1) to profile an extensive set of validated and putative protein biomarkers of ovarian and other epithelial cancers, mesothelial cells, and host cells using gold standard methods on cell lines and prospectively collected human ascites; 2) to identify a reliable ovarian ATC diagnostic panel from our

profiling work and most importantly; 3) devise a novel microfluidic chip leveraging the panel to achieve superior ATC isolation and profiling while obviating the need for centrifuging copious amounts of ascites or employing bulky equipment. We used over 100 commercial antibodies to investigate 85 targets, and analyzed a total of 65 ascites samples from both ovarian cancer and non-cancer patients. We identified a reliable panel of diagnostic markers (ATC_{dx}) with high sensitivity and specificity. Coupled to our practical and inexpensive microfluidic device intended to shift detection and profiling from core laboratories into the point-of-care, we demonstrate superior ATC enrichment (~60 fold) using on-chip purification and only microliter amounts of ascites.

Recent studies have reported on the presence of an accessible and proximal pool of tumor cells within ascites that possess some or most of the characteristics of the primary tumor (135). Studies have also shown that these cells can be preserved and used for broader molecular and functional analyses (157). While smaller series have identified some common target proteins, they have i) often reported conflicting results regarding their relative expression levels (133,158), ii) relied solely on EpCAM for enrichment (156), or iii) failed to compare protein levels in cancerous versus non-cancerous ascites. To our knowledge, the current study introduces one of the larger ATC-focused profiling datasets, highlighting emerging and established diagnostic and mechanistic protein markers.

The profiling data obtained in this study showed unexpected ATC expression levels for various markers. For example, we found low levels of certain markers that have been gaining traction as drug targets (EphA2 (146,159-161)), or that have been touted as specific for (CA-125, FOLR1 (150)), or overabundant in (mesothelin (162))

ovarian cancer. As expected, we found high expression levels of EpCAM, CD24, and TAG-72 in cancer patients, consistent with previous reports (141,163-167). In contrast, levels of calretinin (168,169) and D2-40 (169) were high in mesothelial cells but not in ovarian cancer cells, and thus served as convenient distinction markers. MUC1, EGFR, PAX8, and ESE-1 displayed mixed expression levels that were non-specific.

While the current study is among the most comprehensive of its type, there were some limitations. Firstly, the list of proteins, while lengthy, was not exhaustive. Yet, as a means to deliver a manageable diagnostic set for microfluidic chip testing, it suited study purposes. Secondly, only commercially available antibodies were tested since our intention was to leverage our screening findings for eventual and feasible widespread testing using our POC device. It is possible that certain research antibodies might have resulted in higher and more specific binding, but this would need to be tested in additional data sets beyond the scope of the current study. Thirdly, despite screening a number of available antibodies (**Appendix A**), we were unable to identify reliable antibodies for FSHR (follicle-stimulating hormone receptor), a target implicated in ovarian cancer (170-173) (**Figure 4-5**). We thus abandoned current efforts due to low specificity but FSHR nevertheless remains a marker of interest that needs exploration. Ultimately, by integrating the microfluidic aspects of the ATC chip presented here with other forward-thinking platforms, the breadth and depth of ATC analyses could be significantly expanded. We expect to test both the identified marker panels and ATC chip in larger prospective patient cohorts across multiple institutions.

In addition to screening and treatment monitoring, rapid and reliable bedside analyses using ATC_{dx} and devices such as our ascites microchip offer the potential for

improving intraperitoneal (IP) therapy. Namely, ovarian cancer is unique in that IP delivery of chemotherapy has demonstrated survival advantages (174). However, its success can be severely compromised by untoward side effects. Thus, early signals of efficacy could help inform the risk-benefit assessment of whether to continue therapy. Irrigation of the peritoneal space with saline prior to each IP chemotherapy infusion could be used to provide samples for potential ATC analysis, to track their counts and/or interrogate them further for pharmacodynamic readouts. Moreover, similar strategies to the one reported could be used to translate experimental, yet potentially effective, therapies such as heated intraperitoneal chemotherapy (HIPEC) (175) to the clinical forefront. In sum, by incorporating mechanistic biomarkers, our microfluidic chip approach could become a convenient strategy for mapping ATC numbers and pharmacodynamic readouts at the point-of-care, effectively extending paracenteses from palliative methods into a valuable means to explore their potential for gauging response. Leveraging this additional tumor source could help expand the clinical strategies needed for paradigm shifts in patient oriented research (176).

Chapter 5

Multiplexed DNA Barcode Protein Assay for Molecular Profiling Cancer Cells

Parts of this chapter are under review (2013):
Ullal, A.*, Peterson, V.*, Agasti, S., Tuang, S., Juric, D., Castro, C., Weissleder, R. Single cell protein profiling for cancer detection and treatment.

Abstract

Immunohistochemistry-based diagnoses use a limited number of protein stains to identify cancer cells. Genomic analysis can detect thousands of genes but cannot estimate functional protein levels. Here, we introduce a technology that analyzes dozens to hundreds of proteins in single cells harvested from clinical samples. The method relies on DNA-barcoded antibody sensing: DNA fragments are photo-cleaved following binding and then detected at the single-cell level. We used this approach to first identify ~90 proteins in cells from patients with primary solid tumors and then map their existing heterogeneity at the protein level. This exceptionally specific method was reproducible in cell lines and identified pathway responses to molecularly targeted therapeutics. In clinical samples, the method was able to predict drug response by profiling samples from scant fine-needle aspirates. The mapping technique combines specificity and ease of use to offer a powerful tool for understanding primary human cancers and host cells and for designing future clinical trials.

5.1 Introduction

An increasing number of biopsy-driven cancer trials rely on data collected at two extremes: a) genomic analyses revealing driver oncogenes and specific mutations (5) and b) a limited number of hand-picked protein biomarkers intended to serially monitor cellular responses (177,178). Variable protein levels within tumors and between patients can directly affect drug pharmacodynamics, including the extent to which drugs engage their targets, trigger alternative molecular pathways, and induce tumor cell death or resistance (10). Despite appreciation for the biological relevance of variable protein levels, tools to profile the landscape of key protein networks in clinical biopsies such as fine needle aspirates (FNA) are limited. Proteomic analyses by mass spectrometry remains technically challenging in the clinical setting, and the scant amount of material often evident with minimally invasive biopsies - enablers of serial testing - precludes broader analysis by conventional approaches such as immunohistochemistry (179).

We sought to develop a method that circumvents the limited throughput and loss of material associated with the above methods. We initially considered emerging approaches such as mass cytometry (180) and multicolor spectral deconvolution (181), on-chip proteomic labeling (182) and iPCR (183,184) but these methods either required larger samples or lacked the multiplexing capacity to adequately analyze clinical samples harvested by FNA. Our approach interrogates cells by tagging antibodies of interest with a small DNA barcode. Because we required a release strategy for the unique DNA tag, we developed a stabile photocleavable linker that cleaves at certain wavelengths and shows 3-fold higher release over commercially available disulfide

linkers. Our method relies on capturing released DNA fragments and analyzing their numbers per cell. We were particularly interested in ultimately processing hundreds of proteins simultaneously in few cells. qPCR proved reliable, but its amplification steps introduced bias and prolonged processing time, while its sequencing was not cost-effective. We thus opted for fluorescent barcoding technology that hybridized to 70-mer 'alien' sequences (185). This platform (NanoString Technologies) has been validated to quantitatively measure femtomolar amounts of DNA and RNA but had not been extended to measuring proteins within cells and/or clinical samples.

5.2 Materials and Methods

5.2.1 Cell lines

Validation experiments were performed in the following cell lines, which were purchased from the American Tissue Culture Collection (ATCC): SKOV3, ES-2, MDA-MB-231, MDA-MB-436, A431 and HT1080. Cells were passaged in DMEM (Cellgro) or RPMI (Cellgro) as recommended by ATCC. TIOSE6 cell line was kindly provided by Dr. Michael Birrer (Massachusetts General Hospital, Boston, MA, USA). NOSE cell lines were derived from ovarian surface epithelium (OSE) brushings cultured in 1:1 Media 199:MCDB 105 (Sigma-Aldrich) with gentamicin (25 µg/ml) and 15% heat-inactivated serum. TIOSE6 cell lines were obtained by transfecting hTERT into NOSE cells maintained in 1:1 Media 199:MCDB 105 with gentamicin (25 µg/ml), 15% heat-inactivated serum and G418 (500 µg/ml) (136). After trypsinization, cells were immediately fixed with 1x Lyse/Fix buffer (BD Bioscience) for 10 minutes at 37°C and then washed twice with SB+ (phosphate buffered saline with 2% bovine serum albumin/

BSA). The cells were aliquoted into tubes (~1x10^6 cells/mL) and stored at -20° C until labeling. Biological replicates were seeded in different wells and collected separately. Cultured cells were processed and stored under the exact same conditions as clinical samples. A total of 276 samples were prepared and analyzed independently via the barcoding method.

5.2.2 Clinical samples

The study was approved by the Institutional Review Board, and informed consent was obtained from all subjects. Fourteen minimally invasive procedures were performed on the 10 enrolled patients. Six patients had primary lung adenocarcinomas, and the 4 patients undergoing PI3K inhibitor treatment with repeated biopsies had carcinomas of varying origins in the abdomen, all with underlying PI3K mutations. All pre-treatment biopsies were collected in the week before the first cycle of treatment. All post-treatment biopsies were collected after a cycle was completed, typically after several weeks to months. Image-guided fine needle aspirates using a 22 G needle were obtained prior to routine core biopsies. Correct needle location was confirmed by CT imaging and real-time read-out by cytopathology. FNA samples were processed immediately by centrifugation and removal of excess PBS. If there were visual clumps present before the fixation step, collagenase (Sigma Aldrich) was added at 0.2 mg/ml. Cells were fixed with Lyse/Fix buffer (BD Biosciences) for 10 min at 37°C and washed twice with SB+. All centrifugations were performed at 300 x g for 5 minutes. Clinical samples were stored at -20°C. A total of 24 samples were prepared and analyzed independently via the barcoding method.

5.2.3 Drug treatments

To test the effect of drug treatment on protein expression levels, cell lines were treated with a number of different chemotherapeutic or molecularly targeted drugs. A431 cell lines were dosed with gefitinib (Selleck Chemicals) in media with 1% DMSO overnight at a concentration of 10 μM. The triple negative breast cancer MDA-MB-436 cell line was dosed with the PARP inhibitor Olaparib (10 μM in 0.1% DMSO in media), Cisplatin (10 μM, 1% HBSS in media), PI3K/mTOR inhibitor PKI-587 (100 nM, 0.1% DMSO/media) and the EGFR inhibitors Cetuximab (75 μg/ml in media) and Gefitinib (10 μM in 0.1% DMSO/media). All molecularly-targeted agents (PKI-587, Cetuximab, Gefitinib) were applied overnight. DNA-damaging agents Olaparib and Cisplatin were applied to cells for 3 days. Changes in protein expression levels were compared to media controls under identical conditions but without drug treatment.

5.2.4 Flow cytometry

Flow cytometry was used to validate protein expression levels in bulk samples. Fixed cells stored at -20°C were thawed then permeabilized with a saponin-based buffer, PW+ (1X Perm/Wash PhosFlow Buffer, BD Biosciences, with 2% BSA). Approximately 200,000 cells per tube were incubated with primary antibodies for 1 hr at either 1μg/ml or the appropriate dilution as recommended by Cell Signaling for flow cytometry applications. A complete list of primary antibodies is shown in Table S1. After one wash with PW+, the appropriate secondary antibodies were applied targeting mouse, human or rabbit IgG. The specific secondary antibodies used were Anti-rabbit IgG (H+L) F(ab')2 Fragment Alexa Fluor® 647 Conjugate (Cell signaling, #4414), Anti-mouse IgG (H+L) F(ab')2 Fragment Alexa Fluor® 647 (Cell signaling, #4410) and Anti-

human FITC (Abcam, ab98623). Expression levels for each protein were then calculated by normalizing the geometric mean from each antibody with the appropriate control IgG. These values were then correlated to the expression values derived from the DNA barcoding technique.

5.2.5 Synthesis of photocleavable DNA-antibody bifunctional linker

Compound 1 (**Figure 5-1**, 0.100 g, 0.334 mmol) was dispersed in 5 ml of dry Dichloromethane (DCM) in a round bottom flask under argon atmosphere. The flask was cooled to 0 °C by placing it on an ice bath. 2-(1H-Benzotriazole-1-yl)-1,1,3,3-Tetramethyluronium hexafluorophosphate (HBTU) (0.139 g, 0.368 mmol) and Triethylamine (TEA) (109 μl, 0.835 mmol) were added to the solution. The reaction mixture was stirred at 0 °C for 5 min, and N-(2-aminoethyl)maleimide trifluoroacetate salt (0.093 mg, 0.368 mmol) was subsequently added. After stirring at 0 °C for 15 min, the reaction mixture was allowed to equilibrate to room temperature while being stirred for 18 hours. After the reaction mixture was diluted with DCM (45 ml), the organic phase was washed with water (2x) and sat. NaCl solution (1x), then dried over sodium sulfate. The organic layer was concentrated under reduced pressure and charged to a SiO_2 column (eluent: 100% DCM to 3% methanol in DCM, v/v) for purification. The yield of compound 2 was approximately 60%. ^{1}H NMR (400 MHz, CD_3OD): 7.58 (s, 1H), 7.37 (s, 1H), 6.77 (s, 2H), 5.44 (q, ^4J = 6 Hz, 1H), 4.03 (t, ^3J = 6.4 Hz, 2H), 3.94 (s, 3H), 3.61 (t, ^3J = 5.6 Hz, 2H), 3.35 (t, 2H, overlapping with the solvent residual peak), 2.32 (t, ^3J = 7.2 Hz, 2H), 2.05 (m, 3H), 1.46 (d, ^2J = 6.4 Hz, 3H). MS (electrospray ionization mass spectrometry: ESI-MS) calculated: 421.15, found: 466.18 $\{M+HCOO\}^-$.

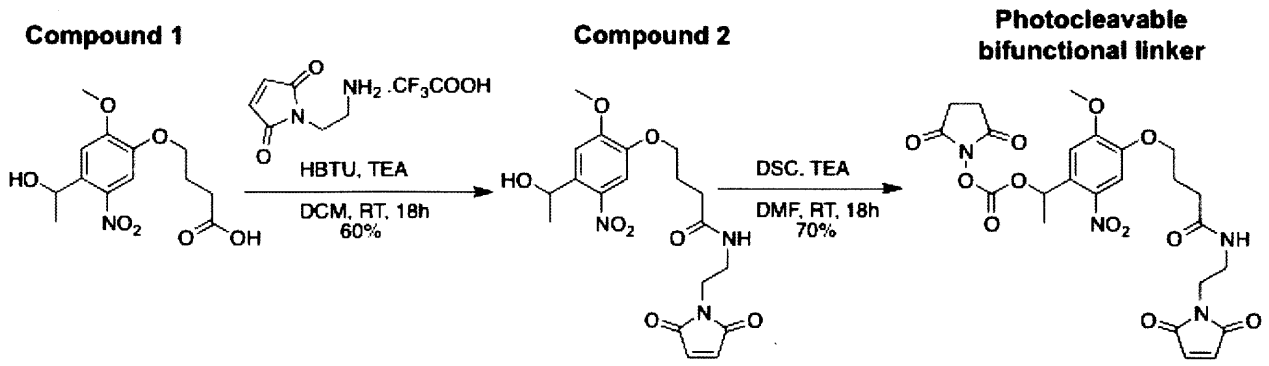

Figure 5-1. Synthesis of photocleavable bifunctional linker.

Compound 2 (0.010 g, 0.024 mmol) was dissolved in anhydrous dimethylformamide (DMF) (1 ml). N,N'-disuccinimidyl carbonate (DSC, 0.018 mg, 0.071 mmol) and TEA (12.5 μl, 0.096 mmol) were successively added to the solution. The reaction mixture was stirred at RT for 18 hours. The reaction mixture was directly loaded onto a C18 reverse phase column for purification (eluent: 5% acetonitrile in water to 95% acetonitrile in water, v/v). The yield of the photocleavable bifunctional linker product was approximately 70%. ^{1}H NMR (400 MHz, $CDCl_3$): 7.63 (s, 1H), 7.05 (s, 1H), 6.67 (s, 2H), 6.48 (q, ^4J = 6.4 Hz, 1H), 6.03 (br, 1H), 4.08 (t, ^3J = 5.8 Hz, 2H), 4.02 (s, 3H), 3.68 (m, 2H), 3.45 (m, 2H), 2.79 (s, 4H), 2.36 (t, ^3J = 7 Hz, 2H), 2.15 (m, 3H), 1.75 (d, ^2J = 6.4 Hz, 3H). MS (electrospray ionization mass spectrometry: ESI-MS) calculated: 562.15, found: 607.22 $\{M+HCOO\}^-$.

5.2.6 DNA-Antibody conjugations

Antibodies listed in **Appendix B** were conjugated to specially designed alien DNA sequences derived from the potato genome (**Appendix C**). The 70mer sequence length was selected for optimal hybridization with the NanoString capture and reporter

probes. Other sizes were tested as well. Shortening sequence length tended to improve signal but reduce hybridization capability. For example, though 50 mer sequences gave relatively higher signals when compared to controls, 30mer sequences did not reliably hybridize. Thus, we selected 70mer sequences for reliable hybridization.

Antibodies (**Appendix B**), purchased from commercial sources, were initially purified from BSA and/or other contaminants using either a Zeba spin column or a MWCO filter. Antibodies were then incubated with photocleavable bifunctional linker in PBS (containing 5% DMF and 10 % 0.1 M $NaHCO_3$) at RT for 1.5 h. Afterwards, excess reagents were removed from maleimide-activated antibodies using a Zeba spin column (7 K MWCO, eluent: PBS).

Thiol-modified DNA oligos (from Integrated DNA Technologies) were reduced using dithiothreitol (DTT, 100 mM) in PBS (1mM EDTA, pH 8.0) for 2 h at RT. The reduced DNA oligos were then purified using NAP-5 column (GE Healthcare), with de-ionized water as the eluent. The fractions containing DTT (determined using the microBCA assay) were discarded. The remaining reduced-DNA fractions were pooled and concentrated using a 3 K MWCO Amicon filter (Milipore).

The maleimide-activated antibodies were incubated with the reduced DNA oligos in PBS solution. In a typical conjugation process, 15 molar excess of DNA oligos were incubated with maleimide-activated antibodies. The conjugation reaction was allowed to proceed for 12 hours at 4℃. DNA barcode-antibody conjugates were purified using a Millipore 100 K MWCO centrifugal filter followed by 3 washes with PBS. After the antibodies were mixed, a final purification of excess DNA was conducted using using Protein A/G coated magnetic beads (Pierce/Thermo Scientific). The commercial protocol

from Thermo for magnetic separation was only slightly modified to use a TBS/0.1% Tween wash buffer and a gentle Ag/Ab elution buffer (Thermo Scientific). Three elutions were performed for 20 minutes each. Then antibodies were exchanged into pure TBS using a Zeba desalting column (7 K MWCO).

5.2.7 Antibody storage and characterization

Antibodies were aliquoted and stored at concentrations of 0.25 mg/ml in PBS with BSA (0.15 mg/ml) at -20 °C, with adequate usage for at least twelve experimental runs (the number of runs on each NanoString cartridge) to avoid freeze-thaw cycles. Various other storage methods were tested, including glycerol or 4 °C storage, but aliquoting and freezing showed the most consistent, high-fidelity storage for up to 9 months. Antibody concentrations were determined via microBCA assay (Thermo Scientific) using a microplate assay. DNA concentrations were also independently determined using the Qubit ssDNA kit (Invitrogen) to quantify the relative number of DNA per antibody. To achieve relative DNA/Ab measurements with higher sensitivity across the cohort of antibodies, we used the NanoString platform to add antibody cocktails under two conditions: 1) "Control": antibodies were added in their native forms with DNA still attached, and 2) "Released DNA":antibodies were treated with proteinase K and photocleaved. Under the control condition, the DNA was still attached to the antibody and thus could not simultaneously bind to the NanoString assay's reporter and capture probe. The difference in DNA readings between these two measurements thus revealed the relative number of DNA per antibody. This difference was divided by the isotype control measurement to account for possible inherent experimental error in protein concentration and/or antibody isolation (**Figure 5-2**).

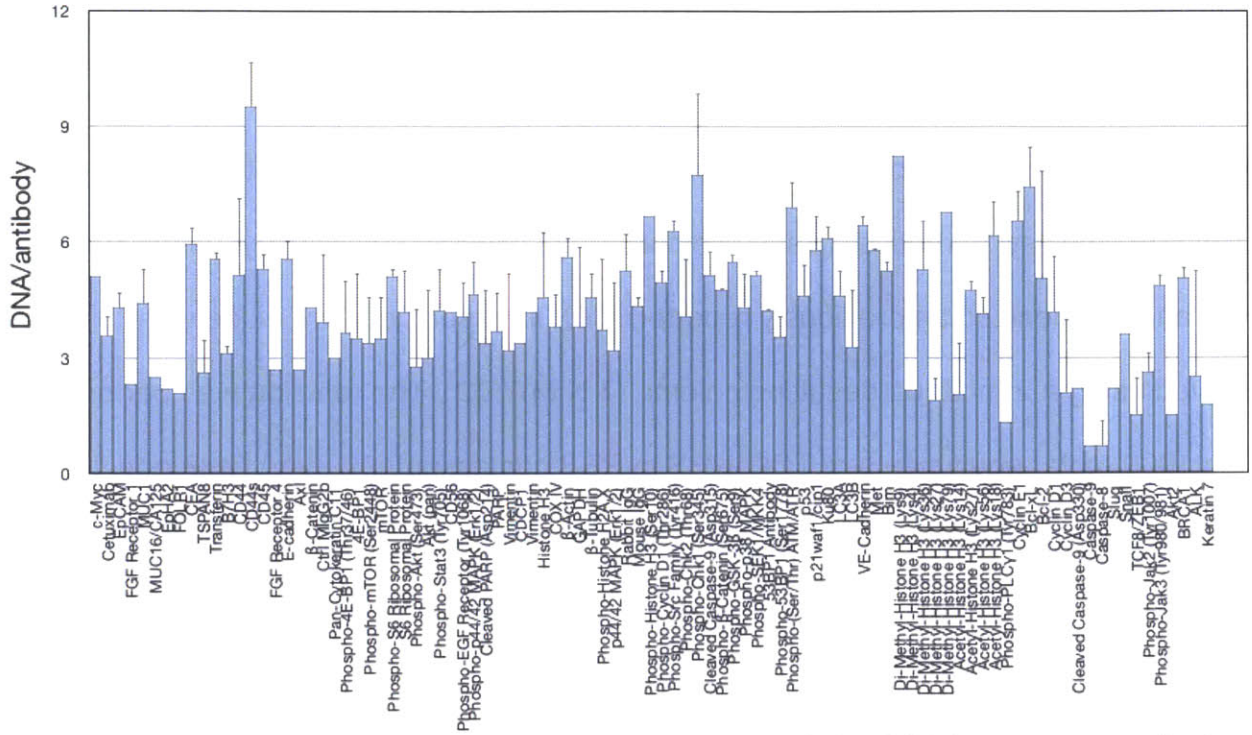

Figure 5-2. DNA per antibody for each conjugate. The number of alien DNA fragments per antibody was measured by NanoString method (shown in graph) and independently confirmed by ssDNA quantification and Qubit protein measurement. On average there were 3-5 DNA fragments per antibody.

5.2.8 Linker optimization

Three alternative methods of conjugating antibodies to DNA via a cleavable linker were evaluated using the general procedures. In the first method, an amine to sulfhydryl linker, sulfosuccinimidyl 6-{3´(2-pyridyldithio)-propionamido} hexanoate (sulfo-LC-SPDP, Thermo Scientific), was reacted with the antibody in PBS-EDTA at 50 molar excess and aged for 1 hour at room temperature. At the end of the reaction, excess sulfo-LC-SPDP was removed using a Zeba desalting column (7 K MWCO). During the antibody reaction, the thiolyated DNA was reduced with DTT and purified via a NAP-5 column, as previously described in the antibody conjugation section. Once excess sulfo-LC-SPDP was purified using a Zeba column, the antibody was reacted with the reduced thiolyated

DNA (~15 molar excess) overnight at 4°C. The final antibody-DNA conjugate was purified by size separation using Amicon filters (100 K MWCO) followed by 3 washes with PBS.

In the second method, antibodies were modified with (E)-Cyclooct-4-enyl 2,5-dioxopyrro-lidin-1-yl carbonate (trans-cyclooctene N-hydroxy-succinimidyl ester; TCO-NHS) and synthesized as previously reported (66). If present, sodium azide was removed using a 2 ml Zeba desalting column (7 K MWCO). The reaction was performed using 1000 molar equivalents of TCO-NHS in PBS containing 10% (v/v) DMF and 10 mM sodium bicarbonate for 4 hours at RT. At the same time, a photocleavable Tz-NHS was reacted with an amine group on the 5' end of the 70 mer DNA strand (15 molar excess) for 4 hours at RT. After the reactions concluded, the Ab-TCO conjugate was purified using a Zeba column (7 K MWCO), and the DNA-Tz conjugate was purified usinga 3 K MWCO Amicon filter followed by three washes with PBS. Next, the TCO-Ab and Tz-DNA were combined via click chemistry (66) for two hours at RT. The final antibody-DNA conjugate was purified by size separation using Amicon 100 K MWCO filters followed by 3 washes with PBS.

In the third method, the photocleavable bifunctional linker (**Figure 5-3**) reacted (10 molar excess) with the amine group on the 5' end of the 70 mer single stranded DNA (IDT) for 4 hours at RT. Three hours after the DNA reaction began, the antibody was reacted with 2-iminothiolane (Traut's reagent, 10 molar excess,Thermo Scientific) to convert amine groups to sulfydryl (-SH) groups in PBS with 2 mM EDTA for 1 hour at RT. When the reactions concluded, the thiolated antibody was separated from excess Traut's Reagent using a Zeba desalting column (7 K MWCO) that had been equilibrated

with PBS containing 2 mM EDTA. The excess PC bifunctional linker was purified from the DNA with an Amicon filter (3 K MWCO). Then the antibody-SH and the DNA-PC-linker (~15 molar excess) were reacted overnight at 4°C. The final antibody-DNA conjugate was purified by size separation using Amicon filters (100 K MWCO) followed by 3 washes with PBS.

The three UV-cleavable Ab-DNA linker methods were compared by first labeling A431 cells with EGFR and EPCAM DNA conjugates and then determining which method resulted in the highest signal to noise ratio (SNR) via NanoString. The antibody-conjugation with the bifunctional photocleavable linker described in **Figure 5-3** gave the highest SNR. This antibody-conjugate was then compared to the antibody-DNA conjugate containing the DTT cleavable disulfide bond. SKOV3 cells (5x10^5 cells) were labeled with Herceptin-DNA conjugates (1 ug). After 30 minutes the cells were spun down at 400 x g for 3 minutes, and the excess Herceptin was removed with two SB+ washes. The Herceptin-DNA conjugate with the disulfide linker was then cleaved by adding DTT (50 mM) for 15 minutes at 37 °C. At the same time, the Herceptin-DNA conjugate with the photocleavable linker was exposed to UV light (wavelength) for 15 minutes. After the 15-minute cleavage step, the cells were spun down at 400 x g for 5 minutes, and the supernatant was removed. The DNA in the superantant was measured using the single-stranded Qubit assay to determine the amount of DNA cleaved from the antibody. The UV photocleavable linker had 2.4 fold more DNA than the disulfide linker.

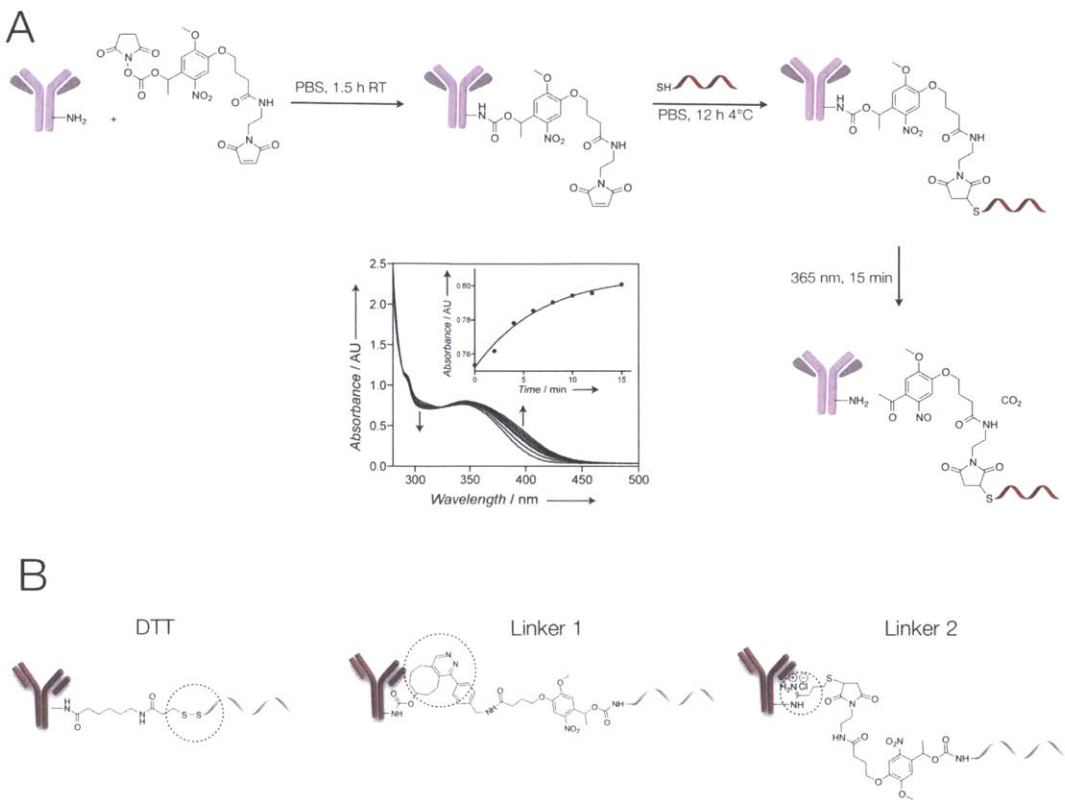

Figure 5-3. Scheme of DNA-antibody conjugation. (A) DNA and antibodies were linked through a photocleavable bifunctional linker. The linker was first reacted with the amine groups on the antibody for 1.5 hr at RT. After excess small molecule was removed, thiolated DNA was added at 10x excess to the antibody-linker mix. The final antibody-DNA chimera was purified via both size separation and IgG specific pulldown. DNA could subsequently be released most efficiently by photocleavage at a specific wavelength (365 nm) as shown across a number of wavelengths. A time course of the photocleavage reaction indicates that maximal release is reached within 15 min. (B) Alternative linker strategies were investigated but not pursued further due to their reduced cleavage efficiency (DTT; linker 1: tetrazine-trans-cyclooctene click chemistry; linker 2: Traut's reagent and the photocleavable bifunctional linker). Linker cleavage was tested by measuring released DNA via NanoDrop and directly on the NanoString platform. The optimized photocleavable linker had a 2.4x greater signal compared to DTT, and over 10x more signal than linker 1 or 2.

5.2.9 Lysis optimization

Four different lysis conditions were evaluated to determine which was the most efficient (**Figure 5-4**): 1) Proteinase K with buffer PKD (Qiagen) and UV; 2) Proteinase K with buffer ATL (Qiagen) and UV; 3) ATL buffer with UV and 4) UV. When UV cleavage was combined with Proteinase K and ATL buffer lysis, assay sensitivity improved and signal increased by approximately 20%.

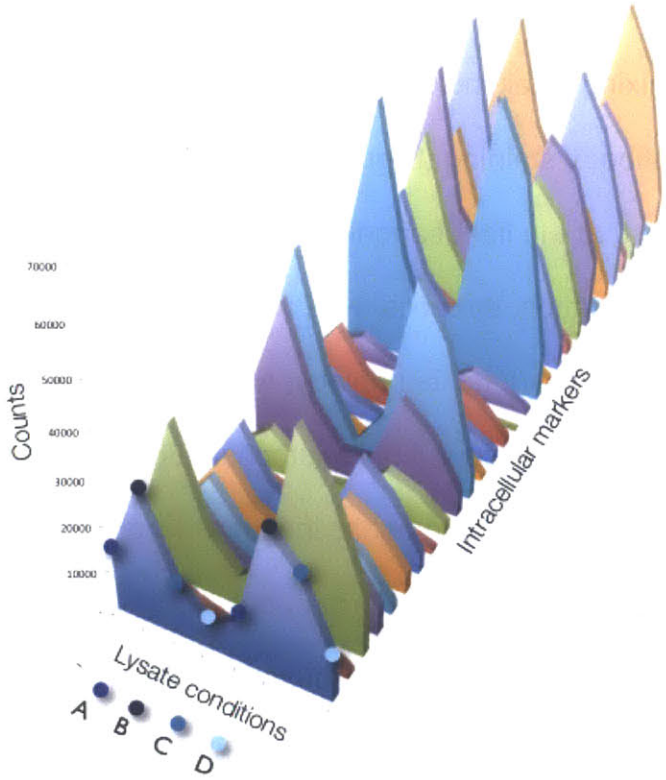

Figure 5-4. Optimizing lysis and blocking methods. Four different lysis and blocking methods (A-D) were used to recover DNA from labeled cells. Lysate conditions included A) Proteinase K + PKD lysis buffer, B) Proteinase K + ATL lysis buffer, C) ATL lysis buffer alone and D) UV cleavage alone (no cell lysis). The lysate conditions were tested in duplicate (x-axis) measuring DNA signal (y-axis) and different intracellular proteins (z-axis). The best reaction condition was method B (Proteinase K + ATL lysis buffer). Using method B with a photocleavage yielded an additional 20% increase in signal.

5.2.10 Antibody staining and DNA collection for protein profiling

Prior to cell staining, antibodies were pooled into a cocktail with TBS, 0.1% tween and 0.2 mg/ml cysteine (to avoid DNA cross reaction with other antibodies). Tubes were coated with serum blocking buffer overnight to prevent samples from non-specifically binding to tube walls. Cells were then incubated for a minimum of one hour with a blocking buffer at 37°C: 10% v/v Rabbit serum (Jackson Immuno Research Labs, 011-000-120), 2% BSA, 1 mg/ml SS salmon sperm DNA (Sigma Aldrich,D7656), 0.2 mg/

ml Cystiene (Sigma Aldrich), 20x Perm (BD Bioscience) or 0.1% Tween 20 (Sigma Aldrich), all in PBS to minimize non-specific antibody or DNA binding. The antibody cocktail was then added to the fixed and permeabilized cells and incubated for one hour at RT with intermittent mixing. Staining with a large number of antibodies was comparable to single-antibody staining (**Figure 5-5 B**) or smaller numbers of markers. We also tested to ensure that the light saponin-based permeabilization did not affect antibody binding. After incubation, the cells were washed with PW+ with 0.05 mg/ml of DS sheared salmon sperm DNA (Life Technology, AM9680). Either two 15 mL washes in 15mL tubes or four 1.5 mL washes in 1.7 mL microcentrifuge tubes were performed. Blocking and wash steps were critical to achieving low background even with femtomolar detection. All washes were performed on ice. Labeled cells could then be counted and selected for lysis/proteinase K/photocleavage to release the DNA. Lysis buffer was used on 10 µL of cells (with up to 50,000 cells), 34.2 µL of ATL lysis buffer (Qiagen) and 5.8 µL of Proteinase K (Qiagen). This reaction proceeded at 56°C for a minimum of 30 minutes. Photocleavage was then performed using long UV wavelength light for 15 minutes. This resulted in a cell-lysis mix with released DNA. Samples were spun down at 14,000 x g for 10 minutes. Supernatant was collected, and serial dilutions were performed in nuclease-free water (Invitrogen, AM9937) to collect DNA equivalent to 50-100 cells to avoid saturating the read-out cartridge (NanoString). This amount resulted in cartridge binding densities within the linear range of quantitation. Binding densities in the lower range (.05- 0.2) were still linear and gave consistent protein profiles comparable to those in the higher range (1.5-2.5). At lower binding densities (for

example single cells), the majority of markers could be measured, with the exception of low expression markers with weaker antibodies (pJAK2, pChk2).

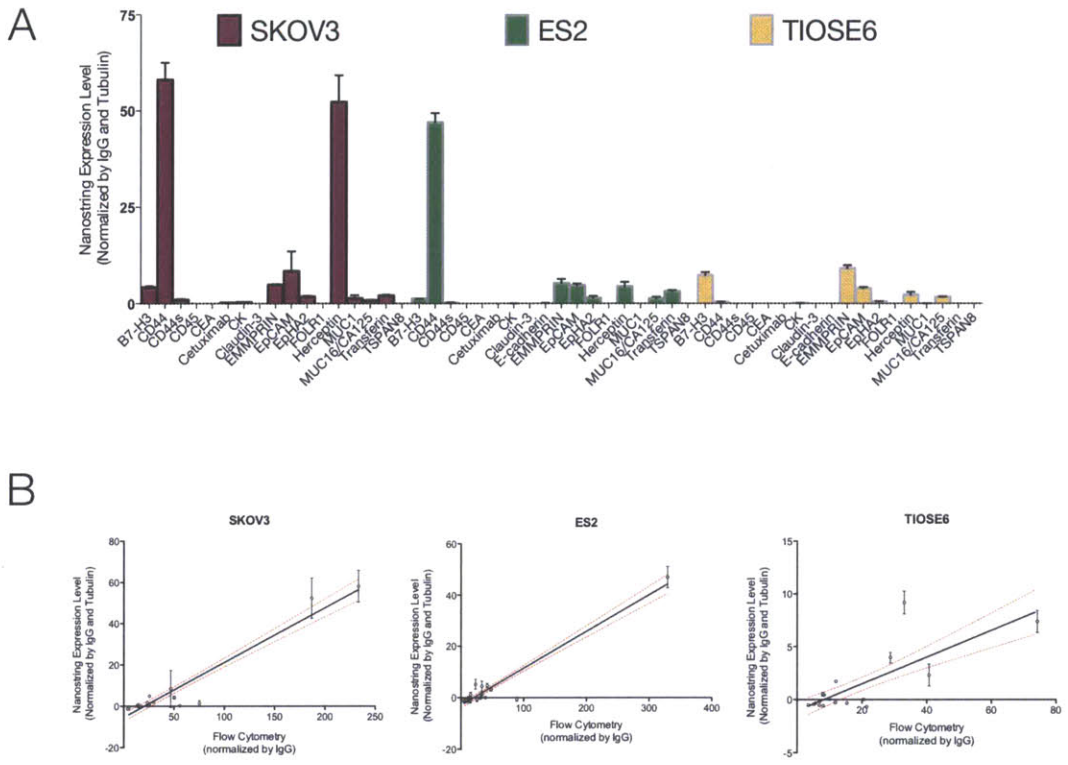

Figure 5-5. Correlation to Flow Cytometry. (A) Bulk cell analysis from DNA barcoding shows high cancer antigen presence in ovarian cancer cell lines SKOV3 (high CD44, Her2) and ES2 (high CD44) but low cancer marker expression in benign ovarian epithelial cell line TIOSE6. (B) Results for each marker (y axis) correlate linearly with high, significant correlations for all three cell lines (SKOV3: Pearson R = 0.96, $r^2 = 0.89$, p <.0001; ES2: Pearson R = 0.96, $r^2 = 0.91$, p <.0001; TIOSE6: Pearson R = 0.78, $r^2 = 0.60$, p <. 0001). In addition, profiling on SKOV3 and ES2 cell lines with DNA-conjugated antibodies, showed high correlation to profiling with unmodified antibodies (SKOV3: Pearson R = 0.93, $r^2 = 0.92$, p<.0001; ES2: Pearson R = 0.85, $r^2 = 0.72$, p<.0001).

5.2.11 Fluorescent read-out

All capture and fluorescent probes were obtained from NanoString Technologies to be compatible with its commercially available Prep/Analyzer station (nCounter Analysis System). Commercial protocols for hybridization and detection from the DNA lysis sample were followed. A total of 276 sample runs were performed for optimization

(n=132), cell line measurements (n = 96), clinical sample measurements (n=24) and single cell measurements and optimization (n=36).

5.2.12 Single cell isolation and processing

After antibody staining, single cells were picked using a micromanipulator. Cells were stained with Hoechst 3342 (Molecular Probes) and added to an open 10 cm dish and imaged using a TE2000 microscope (Nikon). Single cells were placed directly into a PCR tube. Five microliters of lysis buffer/proteinase K were added (4.5 µL ATL buffer: 0.5 µL proteinase K). Lysis/enzymatic cleavage proceeded for 30 minutes at 56 °C before photocleavage for 15 minutes. Reporter and capture probes (NanoString Technologies) were then directly added to this tube according to manufacturers recommendations.

5.2.13 Calculating proteomic expression profiles

Protein expression profiles were extracted from raw data as follows. First, raw DNA counts were normalized via the mean of the internal NanoString positive controls, which account for hybridization efficiency. These counts were then converted to antibody expression values using the relative DNA/Ab counts. Next, average background signal from control IgG antibodies was subtracted. Lastly, housekeeping proteins were used for normalization that accounted for cell number variations. We normalized signals via Beta-tubulin, which provided the most consistent result. For the taxol treatments we normalized via Histone H3, GAPDH and Actin, because tubulin is a primary target of taxol. Data was transformed into log2 scale as denoted in captions.

5.2.14 Clustering

Heat maps and clustergrams were plotted using MATLAB with a matrix input of marker expression values that were calculated as detailed above. All shown clustergrams were performed as a weighted linkage and were clustered using correlation values as a distance metric. Some clustergrams were normalized by row, as specified in captions, to highlight marker differences among different patients. If a marker was not detectable in one of the patients, it was removed from the matrix or heatmap and is not displayed.

5.2.15 Statistical analysis

Correlation between single-cell analysis and bulk measurement was calculated in GraphPad Prism. Spearman R values were calculated without assuming a normal, consistent distribution. Two-sided p values were calculated. Significant markers were identified by comparing two groups (e.g. treated vs. untreated) in Prism and performing pairwise t-tests with an FDR of 0.2 for multiple test correction error. Significant markers and their p-values are displayed in **Table 5-1**. To identify differentiating markers between responders and non-responders, we used a multi-class sequential forward selection ranking algorithm. We classified the patients as responders or non-responders based on known data. Class separability was measured by the Bhattacharya distance.

Proteins	P value	Untreated	Treated
Phospho-S6 RP	0.0067212	1171.3	58.4
Phospho-Histone H3	0.0091305	4920.6	982.0
Ku80	0.0098001	770.2	120.6
FGFR4	0.0106319	914.9	114.1
CD56	0.0117795	1906.5	334.4
Di-Methyl-Histone H3 (Lys36)	0.0119939	695.7	86.9

Table 5-1. Significant markers between A431 +/- gefitinib (single cells). This displays all markers that showed significant difference between gefitinib-treated vs. untreated A431 single cells and the average expression values as calculated via NanoString profiling for each cohort. Markers were determined by pairwise t-testing and corrected for multiple testing errors by using a false discovery rate of 0.2.

5.3 Results and Discussion

To examine whether the method (**Figure 5-6**) was applicable to protein analysis, we developed over 90 antibody conjugates (**Figure 5-2, Appendix B**) containing unique barcodes and targeted MDA-MB231 cells attached by the photo-cleavable linker (**Figure 5-7**). Antibody-DNA conjugates were isolated via IgG specific pulldown and pooled into a labeling cocktail. Cells were blocked to prevent nonspecific DNA or antibody labeling and then "stained" with the pooled cocktail following standard flow cytometry staining techniques. Next, DNA was released, hybridized to fluorescent probes and imaged on a cartridge via a charge-coupled device (CCD). Probe quantification could then be translated into a proteomic sample profile (**Figure 5-6**) by normalizing according to DNA per antibody and housekeeping proteins (**Figure 5-2**). Repeated analyses showed remarkably consistent results across different batches of cells analyzed on different days and over time (**Figure 5-7**). Our results showed high correlation to gold standards such as flow cytometry (**Figure 5-5 B**). Conjugated antibodies behaved similarly to native, unmodified antibodies as evidenced by head-to-head comparison on flow cytometry (**Figure 5-5 B**).

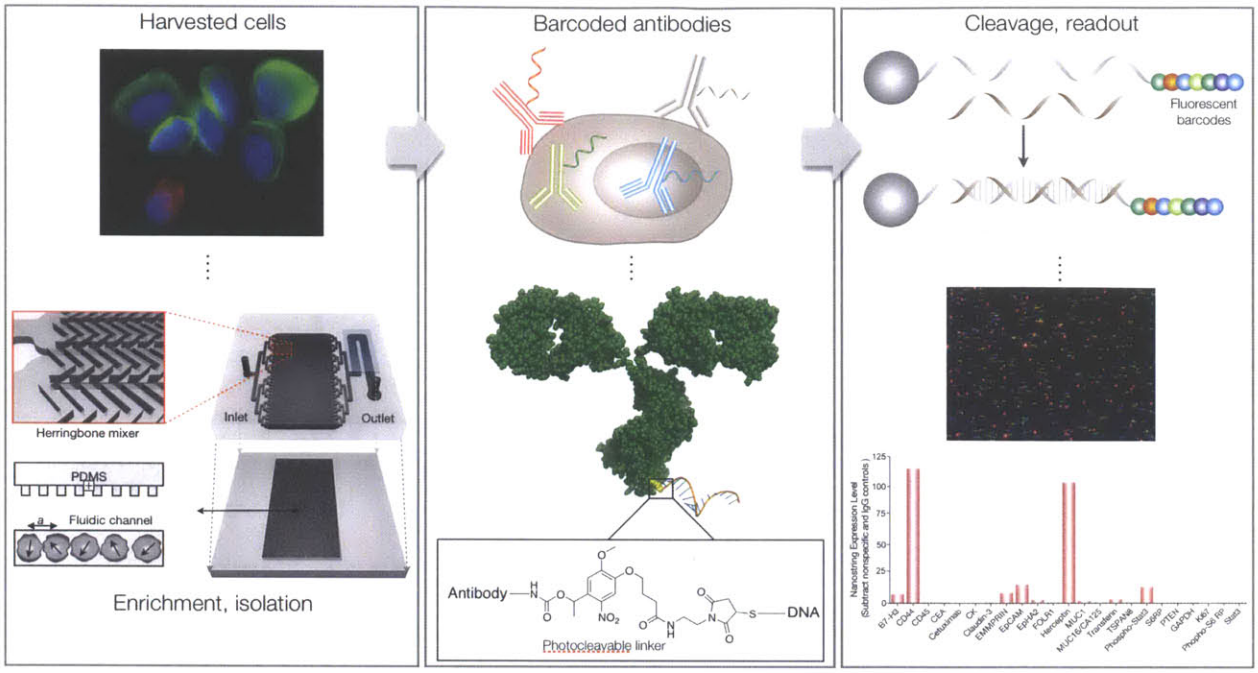

Figure 5-6. Multiplexed protein analysis in single cells. (Left) Cells are harvested from cancer patients by fine needle aspirate. In this case, a heterogeneous population of EpCam positive cancer cells (green) is displayed alongside mesothelial cells (red) with nuclei shown in blue (Hoechst) from an abdominal fine needle cancer aspirate. Cancer cells were enriched and isolated via magnetic separation on microfluidic devices using both positive (e.g. EpCam/CK+) and negative (e.g. CD45-) selection. (Middle) Cells of interest are "stained" with a cocktail of DNA conjugated antibodies. The conjugates contain a photo-cleavable linker (**insert; Figure 5-1**) to allow DNA release after exposure to specific wavelengths of light. DNA-antibody conjugates released from lysed cells are isolated via size-separation and IgG pull down. (Right) Released "alien" DNA barcodes (Appendix C) were processed with a fluorescent DNA barcoding platform (NanoString Technologies). Fluorescent barcodes were hybridized and imaged via a CCD camera. The quantified barcodes were translated to protein expression levels by normalizing according to DNA per antibody and housekeeping genes and subtracting non specific binding from control IgGs.

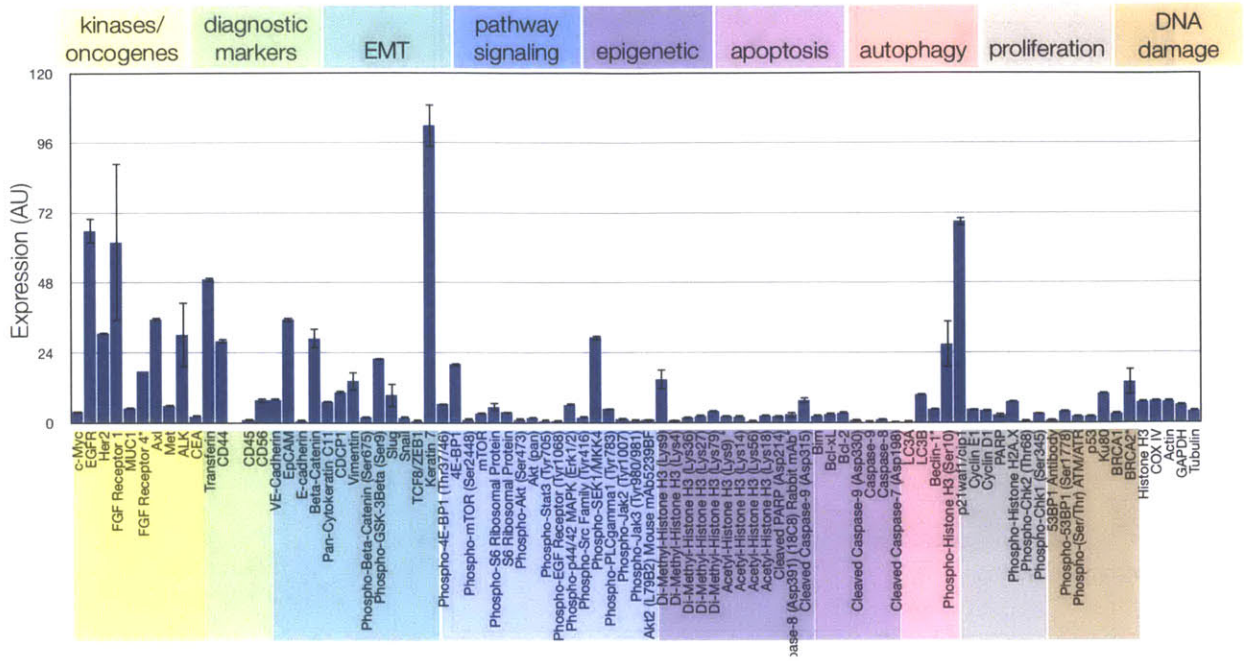

Figure 5-7. Multiplexed cell profiling. Representative example of 88 different antibodies spanning cancer-relevant pathways are profiled in triplicate on the MDA-MB-231 triple negative breast cancer cell line. DNA signal is converted to protein binding by normalizing according to relative DNA per antibody levels. Non-specific binding from expression of six control IgGs is subtracted and expression was normalized by housekeeping proteins. Housekeeping proteins (Cox IV, Histone H3, Tubulin, Actin and GAPDH) are shown at the far right and have consistent expression.

5.3.1 Single cell sensitivity

We then assessed the sensitivity of the method by testing protein detection across varying cell numbers (**Figure 5-8 A**) preparing batches containing 50, 15, or 5 cells in multiple repeats by serial dilution from a bulk sample of 500,000 cells. Analyses in all samples were remarkably linear (**Figure 5-8 B**) with correlation coefficients above 0.9. Additional experiments characterized the method's performance in single cells. For these experiments we harvested individual A431 cells by using a single cell micromanipulator. **Figure 5-8 C** shows expression levels of analyzed proteins amongst different cells and in relation to bulk samples. Consistent with literature (78), we

witnessed some heterogeneity, but generally, single cell profiles matched their respective bulk profiles with correlations as high as 0.96.

A

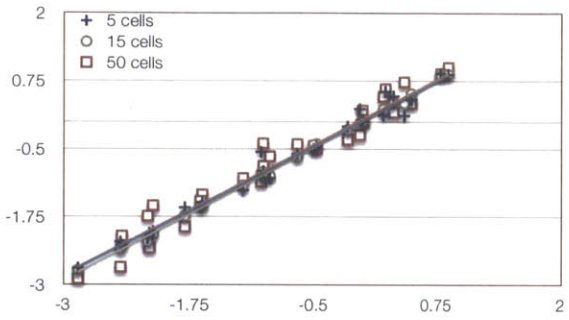

B

Correlation to Bulk	Spearman r	p value
50 cells	0.9526	NA
15 cells	0.9983	< 0.0001
10 cells	0.9292	< 0.0001
5 cells	0.9814	< 0.0001
Single cell 1	0.92	< 0.0001
Single cell 2	0.96	< 0.0001
Single cell 3	0.64	< 0.0001
Single cell 4	0.63	< 0.0001

C

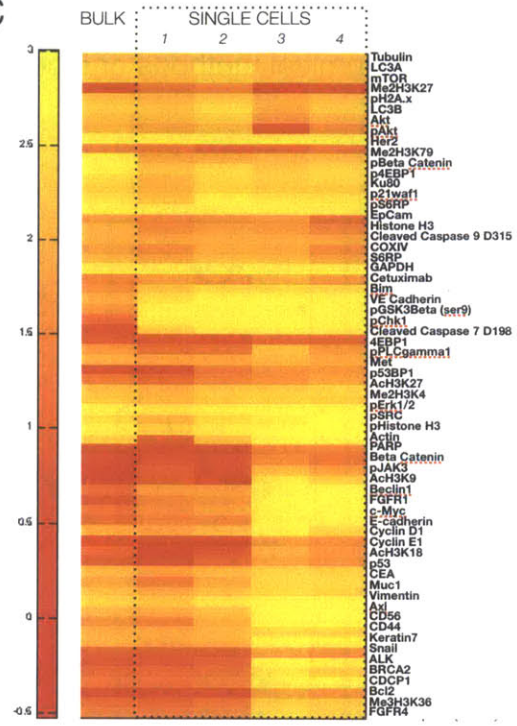

Figure 5-8. Detection sensitivity. (A) 500,000 cells from the epidermoid carcinoma cell line, A431, were lysed and processed as shown in Fig. 1. Dilutions corresponding to 5, 15, and 50 cells were then compared to the bulk measurement, showing good correlation at low cell numbers (Spearman R = 0.98). (B) Correlation values for analyzing small cell numbers as well as single cell analysis selected by micromanipulation. (C) Protein expression profiles (log 2 expression values) of four single cells are compared to profiles of the bulk sample. While all cells showed similar relative protein expression, single cells 1 and 2 showed nearly identical profiles to bulk measurements, whereas single cells 3 and 4 showed lower overall protein levels. Correlations were highly significant when comparing all single cells to bulk measurements ($p<.0001$).

5.3.2 Intratumor heterogeneity

To examine the clinical reach of our analyses, and explore single-cell heterogeneity, a largely under examined topic, we first obtained FNA samples from patients with lung adenocarcinoma (**Figure 5-9**). All investigated cellular proteins were detectable in each of the samples. Single cells (EpCam+, DAPI+, CD45-) correlated with the bulk measurement but with lower levels and wider spread than cell line data.

The highest correlation with the bulk measurement was 0.79 (cell culture showed R= 0.96), while the lowest value was 0.43. This supports findings that cells from a single biopsy location show greater variability than is typically appreciated by current immunohistochemical methods or in vitro models.

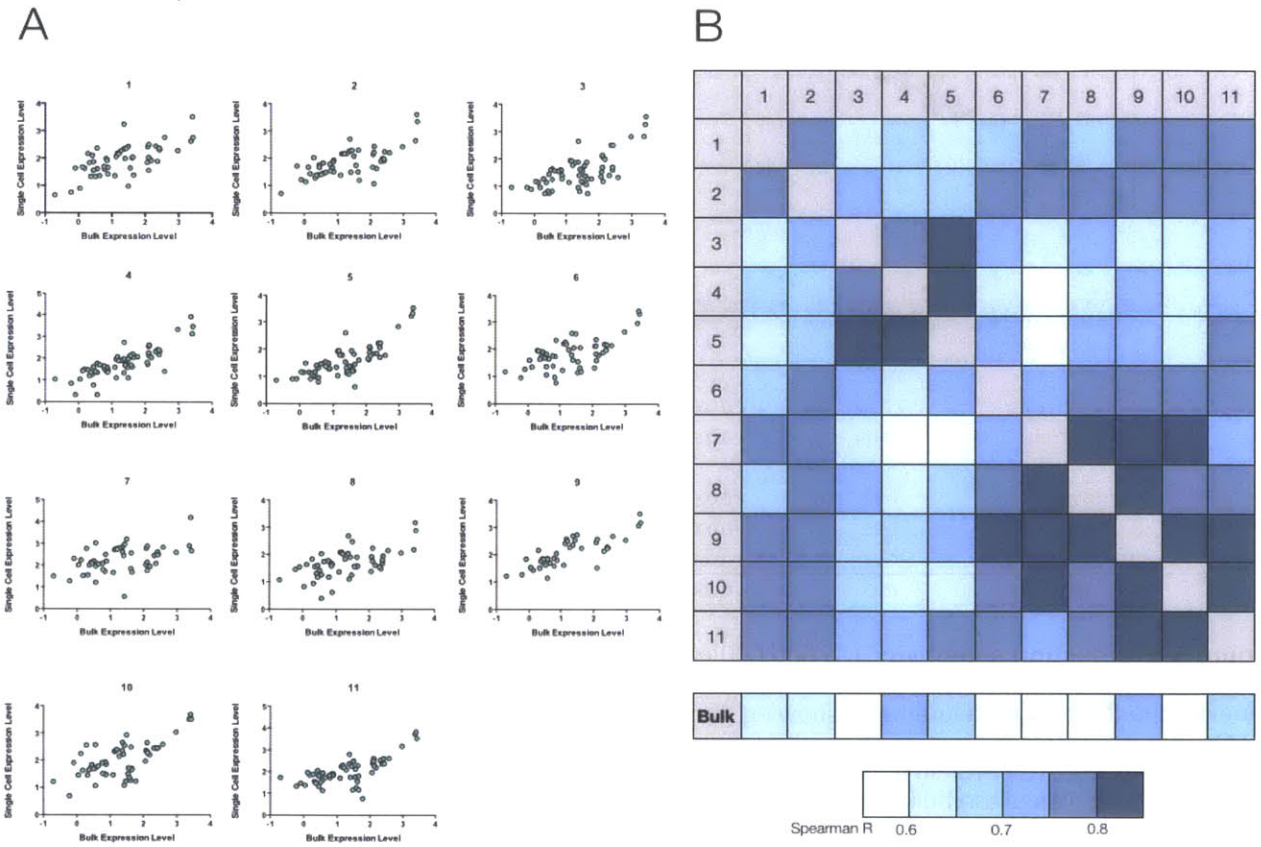

Figure 5-9. Single-cell profiling in patient sample. A fine needle aspirate was obtained from a patient with biopsy-proven lung adenocarcinoma. (A) Eleven harvested cells were analyzed individually, and protein expression levels in each cell (y axis) were correlated with expression levels from the bulk tumor sample (x axis). Though all of the cells show a linear trend, the spread and distribution of the markers varies from cell to cell. (B) Spearman R correlation coefficient values are displayed for each of the single cells to each other and to the bulk measurement. Single cells showed higher correlations to each other as opposed to the bulk. This is expected, as the bulk represents an average measurement of all cells, and thus in a heterogeneous population, is less likely to correlate strongly with a single clonal phenotype.

5.3.3 Interpatient heterogeneity

We next determined inter-patient heterogeneity in six patients with biopsy-proven lung adenocarcinoma (**Figure 5-10**). Though these cancers harbored identical

histopathology, proteomic profiling revealed clear differences even in this small cohort. Experiments were not carried out for diagnostic purposes (i.e. we did not array for TTF-1, napsin, chromogranin, p40, or synaptophysin) but rather to demonstrate protein heterogeneity across a broad range of functional protein networks (16) and relevant for therapy assessment. **Figure 5-10** details similarity among patients 1, 2, and 5 that suggests different genotypes may still result in the same "resistant" proteomic phenotype. This information is an important complement to snapshot genotyping.

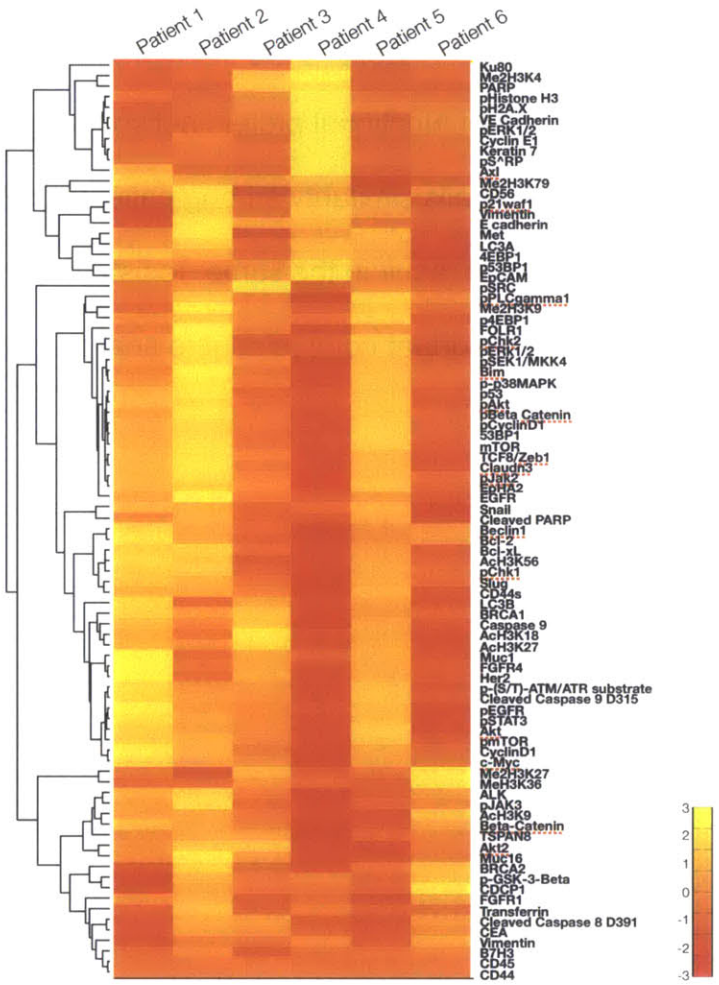

Figure 5-10. Inter-patient heterogeneity in lung cancer. Fine needle aspirates were obtained from six patients with biopsy-proven lung adenocarcinoma, and bulk samples (~100 cells each). Expression data is normalized by row to show differences between each patient. Patients 1, 2, and 5 showed similar protein profiles. This partially concurred with genotyping as both patients 1 and 2 had EGFR exon 19 amplification and T790m mutations. Patient 5 shows a similar profile but had a KRAS mutation. This suggests that different genotypes may result in similar proteomic phenotypes and is consistent with the observation that both EGFR T790M and KRAS mutations are known markers for resistance to EGFR inhibitor therapy [Pao et al., 2005, PLoS medicine, 2, e73; Pao et al., 2005, PLoS medicine, 2, e17]. Patients 3, 4, and 6 all had distinct proteomic profiles, and all had differing mutations. Patient 3 had an exon 20 EGFR mutation, and patient 4 had an EGFR L858R mutation and an additional BRAF mutation. Patient 6 was noted to have an EML4-ALK translocation. Protein clustering also reveals interesting personalized targets. For example, Patient 4 (EGFR/BRAF mutant) had high pERK1/2 and pS6RP as expected; however, this patient also showed a high level of PARP, Ku80 and pH2A.x, which are markers for DNA repair/damage. This suggests that PARP inhibitors or DNA damaging agents (cisplatin) could be effective in this patient.

5.3.4 Treatment response monitoring

The next step was to determine whether the method could readily analyze pathway responses following different drug treatments.We treated triple-negative breast cancer cells with kinase inhibitors and DNA damaging drugs (e.g. gefitinib, cetuximab, PKI-587, olaparib, cis-PT; **Figure 5-11**).

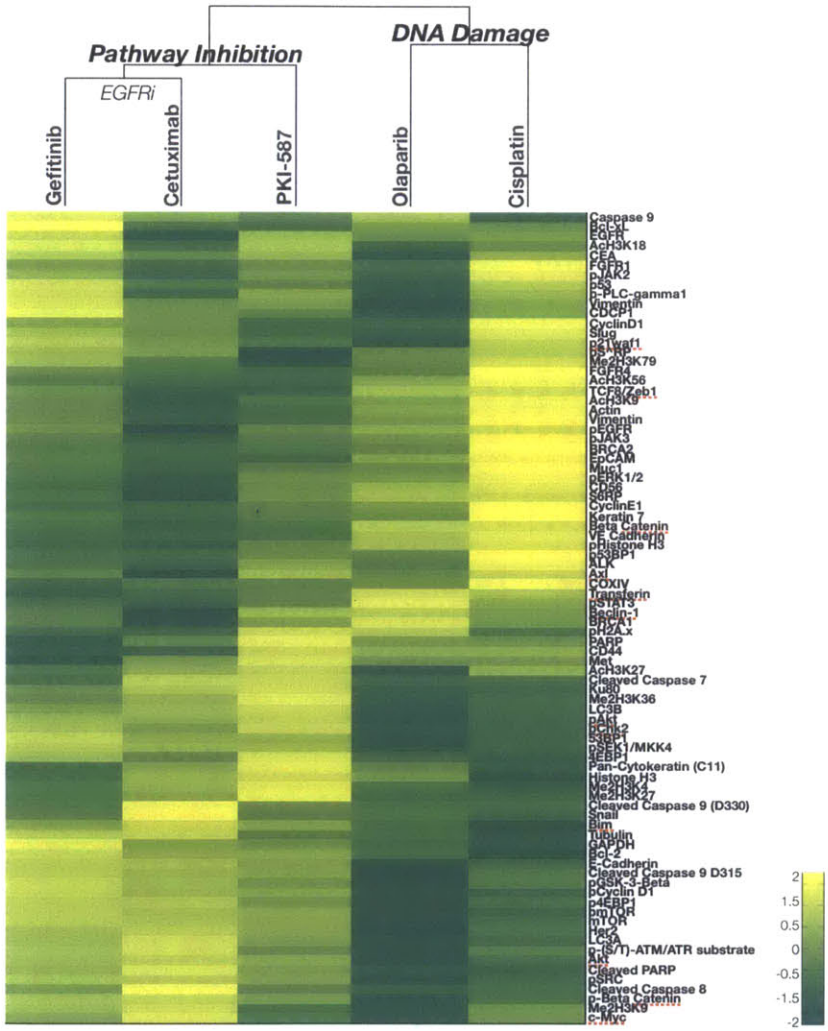

Figure 5-11. Effect of different therapies on protein expression profiles in the triple negative breast cancer cell line MDA-MB-436. MDA-MB-436 cells were treated with different agents and marker proteins were measured. Treatment response markers for each group identified inhibition of expected proteins (p-mTOR, pS6RP, pERK for targeted treatments; pH2A.X, pATM/ATR substrate for DNA damaging agents). Furthermore, unsupervised hierarchical clustering based on euclidean distance (MATLAB) grouped drug treatments by their mechanisms of action (molecularly targeted vs. DNA-damaging) and primary targets (EGFR for Gefitinib/Cetuximab vs. mTOR/PI3K for PKI-587).

Treatment response markers for each group identified known proteins (p-mTOR, pS6RP, pERK for targeted treatments; pH2A.X, pATM/ATR substrate, cleaved PARP for DNA damaging agents; **Figure 5-11**) and mechanisms of action (**Figure 5-12**) but also revealed some unexpected results. For example, the PARP inhibitor induced changes in the PI3K pathway (p-mTOR, pAKT, pS6RP), while the PI3K inhibitor altered DNA repair (PARP and Ku80). This suggests these two pathways may be linked and potential candidates for new combination strategies. Establishing causal and reactive correlations between diseases and altered biomarkers could radically improve physicians' ability to diagnose and treat patients(186,187).

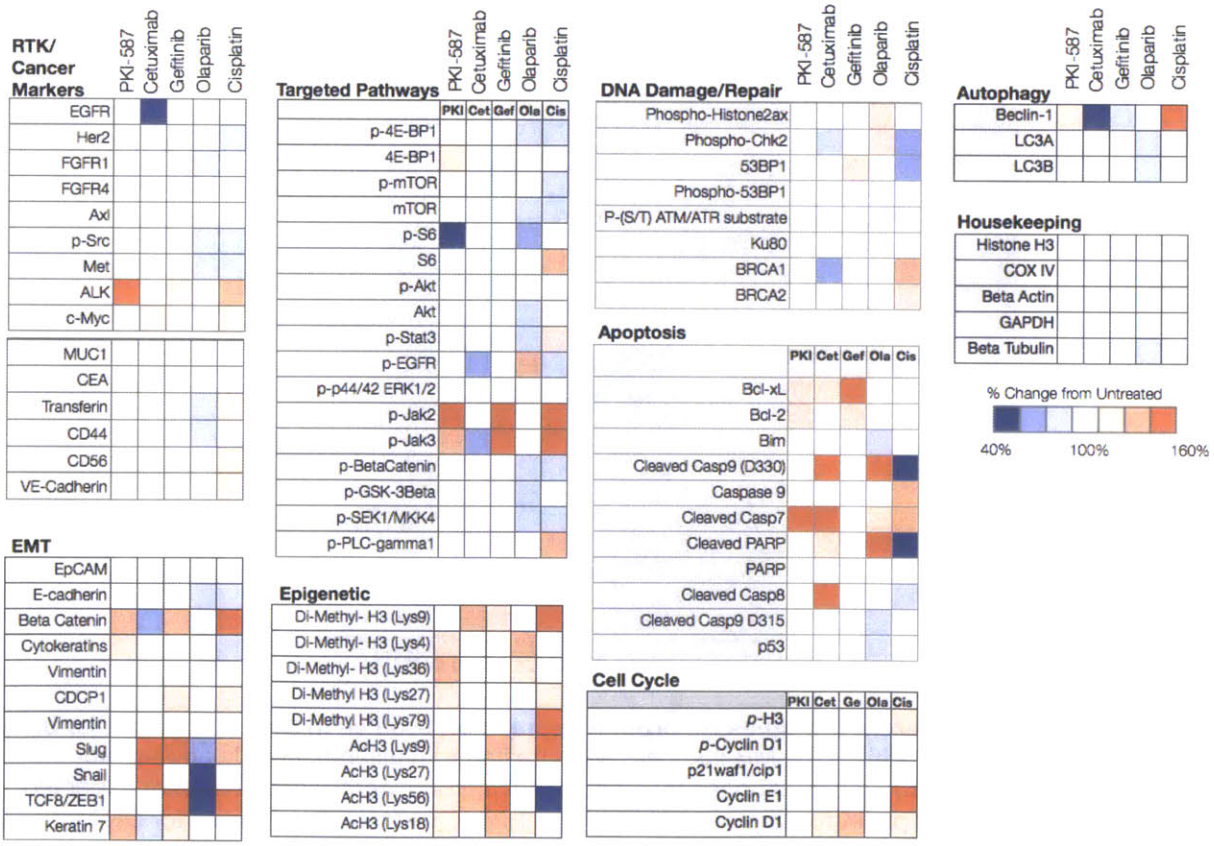

Figure 5-12. Screen for treatment response in triple negative breast cancer cell line (MDA MB 436 ; BRCA1-/-). Heat Map shows fold changes of markers grouped into various categories. Drugs cluster depending on mechanism of action.

An emerging clinical approach is to frequently re-biopsy primary cancers to assess a drug's efficacy and dosage. The ability to analyze small numbers of cells is critical because repeat biopsies are difficult when tumors shrink after treatment and because morbidity and cost preclude highly invasive procedures that collect larger tissue samples. One of our goals was to perform more comprehensive analyses that effectively survey signaling pathways in patient samples. We performed scant cell analyses in 4 patients before and after treatment with a PI3K inhibitors (**Figure 5-13**). In all, two patients responded and two progressed. The two responsive patients received two different doses of the same drug; interestingly, the patient with the higher dose experienced larger-fold changes across the marker panel. The screen could be leveraged to develop companion diagnostics (**Figure 5-13 B**). We employed a marker-ranking algorithm to determine which markers differentiated responders from non-responders. The top marker was H3K79me2, which clustered with several interesting markers: pS6RP (a known downstream target of PI3K and an emerging key biomarker of treatment response (188)), phospho-H2A.X, and PARP. These markers were also identified by in vitro profiling of a PI3K inhibitor. This cluster covered diverse proteins across various pathways: epigenetic changes, DNA damage, and pathway inhibition. Future targeted therapies must rely on biomarkers that predict treatment response, given the considerable costs of treatment. Intra-tumoral heterogeneity may itself be a biomarker of poor clinical outcome (189), and heterogeneity estimates may provide another way to assess tumor propensity for adaptation after drug exposure.

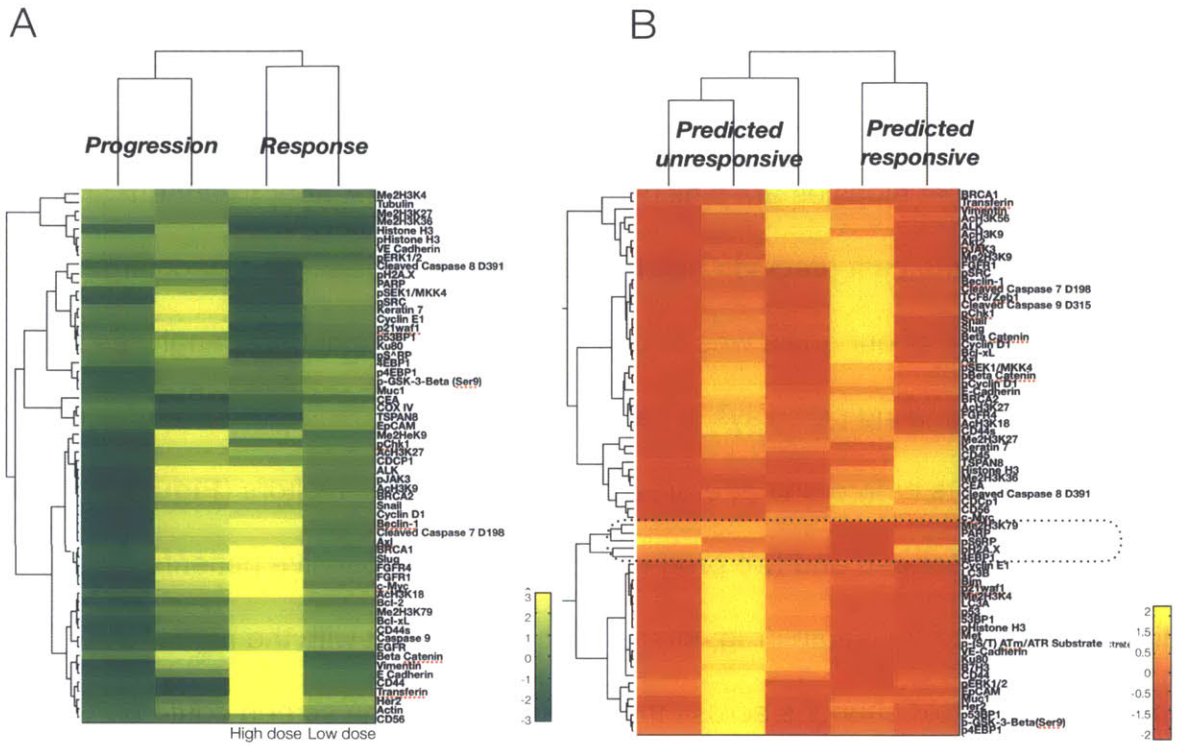

Figure 5-13. Monitoring and predicting treatment response in patients receiving PI3K inhibitors. (A) Four patients with biopsy-proven adenocarcinoma were treated with PI3K inhibitors, and primary cancers were biopsied before and after treatment. The heat map is a pre-post treatment difference map showing log2 fold changes in protein expression (normalized by row to highlight differences between patients). Patients segregate into two clusters (correlation distance metric; weighted linkage): tumors that responded and tumors that progressed. The patient in the third column received a higher dose of the PI3K inhibitor (400 mg bid as opposed to 150 mg bid) and showed greater up-regulation and down-regulation across the marker panel. (B) Profiles of five drug-naive lung cancer patients are shown with clustering based on correlation metrics with weighted linkage. The patients group into responders and non-responders. A marker ranking algorithm identifies H3K79me2 as the top differential marker between responders and non-responders. The dotted box shows that this marker clusters with proteins across many protein networks including pS6RP (a downstream target of PI3K), pH2A.X (DNA damage marker), PARP (DNA repair protein) and 4EBP1 (protein translation). The predictions correlated with subsequent clinical observation.

5.4 Conclusion

In summary, we developed a method that senses tens to hundreds of proteins in human cells by using DNA-barcoded antibodies and photocleavable linkers with subsequent optical readout. Well-established techniques and rapid processing -- cell labeling, washing and analysis that can be completed within several hours -- make same-day protein analysis possible. Beyond its simplicity and efficiency, this method requires far less material than multiplexed cytometry (190) or immunohistochemistry. Extending the coverage of additional protein targets is easily performed through additional labeled antibodies and enables scalable, multiplexed protein screening. In general, the method can provide important insight into protein expression levels within single cells and cell populations. Indeed, we were able to perform single-cell analyses of scarce proteins such as 53BP1 and p-histone H2AX. We expect the method can be used for larger protein mapping and perhaps even topological visualization in cells. Such methods would be useful for single-cell analysis of circulating tumor cells, scant immune cell populations, stem cells, and/or investigations into clonal evolutions. Finally, another advantage is its adaptability to concurrent genetic analyses (DNA/RNA) for multiplexed protein-DNA-RNA investigations.

Chapter 6

Conclusions and Recommendations

Abstract

To conclude my thesis, I have summarized the major findings of each chapter. I have also included a discussion of recommendations for future work.

6.1 Summary

Due to the complexity and heterogeneity of cancer, there has been a continuous need for tools to moleculary profile cancer cells in clinical samples where limited number of cancer cells are the norm rather than the exception. Highly sensitive technologies that yield rapid, quantitative, and multiplexed readouts at the point-of-care setting are desirable. My thesis work sought to develop proteomic tools that met these needs and apply them to the diagnosis, treatment response monitoring, and measurements of intratumoral and intrapatient heterogeneity using clinically attained specimens from cancer patients.

6.1.1 Chapter 2

Chapter 2 refers to a three pronged approach to optimize the magnetic nanoparticle (MNP) labeling step in DMR to increase detection sensitivity and improve assay robustness. First, introduction of a PEG linker reduced background noise from non-specific MNP binding. Second, we implemented a cleavage step to improve assay robustness and sensitivity. Lastly, additional rounds of bioorthogonal nanoparticles successfully amplified signal.

1) *Reducing backround noise.* A lack of appreciable overall signal to noise ratios (SNR) due to increased background noise represented one hurdle limiting signal amplification through multiple rounds of complementary MNP. By adding a PEG spacer between the MNP and the orthogonal reactant the non-specific nanoparticle binding was significantly reduced and the background remained negligible; this led to a considerable increase in overall SNR.

2) Cleavage step. A cleavage step was incorporated to release nanoparticles from cells at the end of labeling -- this further improved assay sensitivity and robustness. Here, a disulfide bond (cleavable with DTT), was placed between the MNP and the PEG linker. Clinical samples are often very heterogenous and, along with cancer cells, can contain cellular debris, aggregates, components of extracellular matrix, and non-cancerous cells such as lymphocytes, neutrophils, macrophages, etc. After cleaving MNPs from cells, the MNPs remained suspended in solution whereas the cells and other contaminants settled out of solution, reducing background noise in the process. In addition, since MNP are no longer bound to cells they may interact more with surrounding water molecules which can lead to further increases in signal.

The cleavage step also solved time sensitivity issues encountered during DMR measurements. Previously, MNPs remained attached to cells and began settling out of solution during measurements, resulting in variability. In summary, the cleavage step improved assay sensitivity, robustness, and reproduciblity while eliminating the need for longitudinal samples to be analyzed real time. Moreover, cells are reusable after measurement for further analyses.

3) Rounds of amplification. Lastly, successive rounds of biorthogonal magnetic nanoparticles (MNP-Tz and MNP-TCO) were implemented in the labeling step to increase signal. The most significant increase occurred when two rounds of magnetic nanoparticles (MNP-Tz and MNP-TCO) were cleaved. This was most likely due to clustering between the cleaved nanoparticles, best explained by a unique phenomenon known as magnetic relaxation switching. Here, clusters of magnetic nanoparticles increase the relaxation rate of water molecules compared to magnetic nanoparticles

evenly dispersed throughout the solution. This phenomenon was exploited to enhance signal.

In conclusion, this three-pronged approach increased detection sensitivity by 1-2 orders of magnitude and improved assay robustness in heterogeneous clinical samples. Cancer cells were readily detected and molecularly profiled in unpurified clinical samples while conventional methods such as flow cytometry were hampered by the need for time-consuming purification steps that resulted in significant cell loss.

6.1.2 Chapter 3

In Chapter 3, we implemented DMR technology in a clinical setting to analyze cells obtained by fine-needle aspirates from suspicious lesions in 50 patients. The results were then validated in an independent cohort of another 20 patients. Single fine-needle aspirates yielded sufficient numbers of cells to enable quantification of multiple protein markers in all patients using DMR. A four-protein signature was identified and enabled us to achieve 96% accuracy for establishing cancer diagnosis, surpassing conventional clinical analysis by immunohistochemistry. Results show that protein expression patterns decay with time, underscoring the need for rapid sampling and diagnosis close to the patient bedside. Also, a surprising degree of heterogeneity in protein expression both across different patient samples and even within the same tumor was observed, which has important implications for molecular diagnostics and therapeutic drug targeting. Our quantitative point-of-care DMR approach shows potential for rapid, multiplexed analysis of human tumors for cancer diagnosis in the clinic.

6.1.3 Chapter 4

In Chapter 4, we hypothesized that ascites, frequently drained for symptomatic relief in ovarian cancer (OvCA) patients, contains intact cancer cells (called ascites tumor cells, or ATCs) that could be used for molecular analysis. First, we profiled a comprehensive panel of validated and putative biomarkers of ovarian cancer since the literature was replete with contradicting data. A total of 85 commercially available antibodies were selected and tested in 12 ovarian cancer cell lines, two mesothelial cell lines, two benign ovarian cell lines, as well as in lymphocytes and neutrophils. From this data, 31 markers were identified and profiled in a training set of human ascites samples (n=18). In this training set we identified an ascites-derived tumor signature termed ATC_{dx} which refers to cells that are either EpCAM+ and/or V3 positive (Vimentin +/Calretinin-/CD45-). This tumor signature was then validated in a cohort of 47 patients (33 ovarian cancer and 14 control), where all 33 ovarian cancer patients were correctly identified. In a smaller subset of patients we obtained serial samples (n=7) where we demonstrated that ATCs can be used to measure treatment response and differentiate responders from non-responders.

Finally, we designed a novel microfluidic enrichment chip that allows visualization of molecular markers such as ATC_{dx} to facilitate detection of tumor cells in heterogeneous ascites fluid. The enrichment of cancer cells is based on a combination of magnetic and size purification. The chip was designed to be optically transparent so that ATCs could be easily visualized after being captured and stained. The chip requires small sample volumes and has single cell detection sensitivity. Furthermore, it is very inexpensive and can be easily fabricated using soft lithographic techniques,

providing a point-of-care method that has potential to find widespread use for ATC analyses and diagnosis.

6.1.4 Chapter 5

In Chapter 5, we developed a highly multiplexed proteomic assay using a photocleavable DNA barcoding method conferring single cell sensitivity. We validated our method using a 94 marker panel in cell lines to examine different treatment responses and heterogeneity at the single cell level. We then extended our analysis to clinical samples to demonstrate the potential of our proteomic approach to assist in monitoring cancer therapy through tumoral changes before and after treatment. We showed that proteomic tumor profiles can provide sufficient information for prediction of treatment response. Finally, we were able to examine interpatient variability and intratumoral heterogeneity of single cells with this highly sensitive assay.

6.2 Recommendations for future work

In my journey through graduate school, I have come to realize that Ph.D. research is never really finished. More paths are invariably available to explore and expand on your research. Here, I outline potential directions for future work on the three tools that were developed for molecular profiling of cancer cells in clinical samples for cancer detection and treatment response monitoring.

In Chapter 2 and 3, I discussed diagnostic magnetic resonance (DMR) technology. Despite the interval progress, we believe that DMR-3 could be further enhanced to maximize clinical utility. We anticipate furnishing the device with more advanced multichannel measurement and microfluidic (e.g. separation) capabilities to facilitate on-

chip processing of clinical samples. We are currently exploring broader technologies for combining sensitive DMR measurements with higher throughput purification chips. Ideally, the goal would be to develop microfluidics upstream of the DMR device that can mix magnetic nanoparticles with complex biological fluids, separate cancer cells, then distribute aliquots to different microcoils for parallel multichannel sensing. We are also investigating ways to improve technologies using miniature magnetometer sensors for single cell analysis in clinical samples such as circulating tumor cells (CTCs) for screening or monitoring cancer recurrence. Finally, DMR analyses could be extended to analyze other cell types including immune cells, stem cells or non-epithelial neoplasms, which could facilitate the development of additional surrogate endpoints for clinical trials.

In Chapter 4, I discussed the development of a microfulidic chip for ascites tumor cell enrichment and purification. One potential avenue of future work would involve modifying chip design to easily recover cells for further dowstream analyses such as genetic, mRNA, or the NS protein assay discussed in chapter 5.

In Chapter 5, I discussed a novel proteomic assay we recently developed in our lab. There are many exciting future applications for this highly sensitive assay such as multiplexed proteomic analysis of rare CTCs, stem cells, or exosomes. It can be used as a tool to screen drugs on clinical samples before and during treatment to allow clinicians to personalize patient's treatment plans. Furthermore, the assay can be coupled with genomic tools to provide an integrated profiling approach examing protein, mRNA, and DNA on the same set of cells without the need for aliquoting.

There are also future opportunities to reduce assay cost. Unfortunately, the most expensive ingredient of this assay remains the antibodies. This is a common issue faced in the proteomic field since antibodies are used for most assays. It is very common for companies to charge $300-500 for small quantities (~100 ug) of antibody. This results in a multiplexed assay looking at 100 protein markers costing a minimum of ~$30,000 excluding other reagent costs. Another problem is that many antibody formulations contain other proteins that need to be removed before DNA conjugation. Typically, currently available separation methods have low yield and result in loss of very expensive antibody. Custom orders of pure antibody formulations further increase the already exorbitant cost. There is a very large unmet need to discover new methods of purification with higher yields. In order to make multiplexed proteomic assays (> 100 markers) an affordable reality in labs, methods to make cheaper antibodies are critically needed.

References

1. Maheswaran, S., Sequist, L. V., Nagrath, S., Ulkus, L., Brannigan, B., Collura, C. V., Inserra, E., Diederichs, S., Iafrate, A. J., Bell, D. W. et al. Detection of Mutations in Egfr in Circulating Lung-Cancer Cells. *N. Engl. J. Med. 359*, 366-377 (2008).
2. Hanahan, D. Weinberg, R. A. The Hallmarks of Cancer. *Cell 100*, 57-70 (2000).
3. Von Hoff, D. D., Stephenson, J. J. J., Rosen, P., Loesch, D. M., Borad, M. J., Anthony, S., Jameson, G., Brown, S., Cantafio, N., Richards, D. A. et al. Pilot Study Using Molecular Profiling of Patients' Tumors to Find Potential Targets and Select Treatments for Their Refractory Cancers. *J. Clin. Oncol. 28*, 4877-4883 (2010).
4. Brennan, D. J., O'Connor, D. P., Rexhepaj, E., Ponten, F. Gallagher, W. M. Antibody-Based Proteomics: Fast-Tracking Molecular Diagnostics in Oncology. *Nat. Rev. Cancer 10*, 605-617 (2010).
5. Vogelstein, B., Papadopoulos, N., Velculescu, V. E., Zhou, S., Diaz, L. A. J. Kinzler, K. W. Cancer Genome Landscapes. *Science 339*, 1546-1558 (2013).
6. Paez, J. G., Janne, P. A., Lee, J. C., Tracy, S., Greulich, H., Gabriel, S., Herman, P., Kaye, F. J., Lindeman, N., Boggon, T. J. et al. Egfr Mutations in Lung Cancer: Correlation With Clinical Response to Gefitinib Therapy. *Science 304*, 1497-1500 (2004).
7. Soda, M., Choi, Y. L., Enomoto, M., Takada, S., Yamashita, Y., Ishikawa, S., Fujiwara, S., Watanabe, H., Kurashina, K., Hatanaka, H. et al. Identification of the Transforming Eml4-Alk Fusion Gene in Non-Small-Cell Lung Cancer. *Nature 448*, 561-566 (2007).
8. Dhingra, V., Gupta, M., Andacht, T. Fu, Z. F. New Frontiers in Proteomics Research: A Perspective. *Int. J. Pharm. 299*, 1-18 (2005).
9. Rogers, S., Girolami, M., Kolch, W., Waters, K. M., Liu, T., Thrall, B. Wiley, H. S. Investigating the Correspondence Between Transcriptomic and Proteomic Expression Profiles Using Coupled Cluster Models. *Bioinformatics 24*, 2894-2900 (2008).
10. Yaffe, M. B. The Scientific Drunk and the Lamppost: Massive Sequencing Efforts in Cancer Discovery and Treatment. *Sci. Signal. 6*, pe13 (2013).
11. Etzioni, R., Urban, N., Ramsey, S., McIntosh, M., Schwartz, S., Reid, B., Radich, J., Anderson, G. Hartwell, L. The Case for Early Detection. *Nat. Rev. Cancer 3*, 243-252 (2003).
12. Farley, J., Penson, R., del Carmen, M. G. Birrer, M. Getting Personal! The Treatment of Epithelial Ovarian Cancer. *Clin. Ovarian Cancer 2*, 9-11 (2009).
13. Schmalfuss, F. Kolominsky-Rabas, P. L. Personalized Medicine in Screening for Malignant Disease: A Review of Methods and Applications. *Biomark Insights 8*, 9-14 (2013).
14. Steffensen, K. D., Waldstrom, M. Jakobsen, A. The Relationship of Platinum Resistance and Ercc1 Protein Expression in Epithelial Ovarian Cancer. *Int. J. Gynecol. Cancer 19*, 820-825 (2009).
15. Mahner, S. Pfisterer, J. Towards Individualised Treatment in Ovarian Cancer. *Lancet Oncol. 14*, 101-102 (2013).
16. Hanahan, D. Weinberg, R. A. Hallmarks of Cancer: The Next Generation. *Cell 144*, 646-674 (2011).

17. Farley, J., Brady, W. E., Vathipadiekal, V., Lankes, H. A., Coleman, R., Morgan, M. A., Mannel, R., Yamada, S. D., Mutch, D., Rodgers, W. H. et al. Selumetinib in Women With Recurrent Low-Grade Serous Carcinoma of the Ovary Or Peritoneum: An Open-Label, Single-Arm, Phase 2 Study. *Lancet Oncol. 14*, 134-140 (2013).
18. Mallon, R., Feldberg, L. R., Lucas, J., Chaudhary, I., Dehnhardt, C., Santos, E. D., Chen, Z., dos Santos, O., Ayral-Kaloustian, S., Venkatesan, A. et al. Antitumor Efficacy of Pki-587, a Highly Potent Dual Pi3K/Mtor Kinase Inhibitor. *Clin. Cancer Res. 17*, 3193-3203 (2011).
19. Pant, A., Lee, I. I., Lu, Z., Rueda, B. R., Schink, J. Kim, J. J. Inhibition of Akt With the Orally Active Allosteric Akt Inhibitor, Mk-2206, Sensitizes Endometrial Cancer Cells to Progestin. *PLoS ONE 7*, e41593 (2012).
20. Mabuchi, S., Hisamatsu, T. Kimura, T. Targeting Mtor Signaling Pathway in Ovarian Cancer. *Curr. Med. Chem. 18*, 2960-2968 (2011).
21. Chen, Y., Zhang, L. Hao, Q. Olaparib: A Promising Parp Inhibitor in Ovarian Cancer Therapy. *Arch. Gynecol. Obstet.* (2013).
22. Blank, S. V., Christos, P., Curtin, J. P., Goldman, N., Runowicz, C. D., Sparano, J. A., Liebes, L., Chen, H. X. Muggia, F. M. Erlotinib Added to Carboplatin and Paclitaxel as First-Line Treatment of Ovarian Cancer: A Phase Ii Study Based on Surgical Reassessment. *Gynecol. Oncol. 119*, 451-456 (2010).
23. Bull Phelps, S. L., Schorge, J. O., Peyton, M. J., Shigematsu, H., Xiang, L. L., Miller, D. S. Lea, J. S. Implications of Egfr Inhibition in Ovarian Cancer Cell Proliferation. *Gynecol. Oncol. 109*, 411-417 (2008).
24. Ohta, T., Ohmichi, M., Shibuya, T., Takahashi, T., Tsutsumi, S., Takahashi, K. Kurachi, H. Gefitinib (Zd1839) Increases the Efficacy of Cisplatin in Ovarian Cancer Cells. *Cancer Biol. Ther. 13*, 408-416 (2012).
25. English, D. P., Roque, D. M. Santin, A. D. Her2 Expression Beyond Breast Cancer: Therapeutic Implications for Gynecologic Malignancies. *Mol. Diagn. Ther. 17*, 85-99 (2013).
26. Yap, T. A., Carden, C. P. Kaye, S. B. Beyond Chemotherapy: Targeted Therapies in Ovarian Cancer. *Nat. Rev. Cancer 9*, 167-181 (2009).
27. Lee, H., Sun, E., Ham, D. Weissleder, R. Chip-Nmr Biosensor for Detection and Molecular Analysis of Cells. *Nat. Med. 14*, 869-874 (2008).
28. Hogemann, D., Ntziachristos, V., Josephson, L. Weissleder, R. High Throughput Magnetic Resonance Imaging for Evaluating Targeted Nanoparticle Probes. *Bioconjug. Chem. 13*, 116-121 (2002).
29. Perez, J. M., Grimm, J., Josephson, L. Weissleder, R. Integrated Nanosensors to Determine Levels and Functional Activity of Human Telomerase. *Neoplasia 10*, 1066-1072 (2008).
30. Lee, H., Yoon, T. J., Figueiredo, J. L., Swirski, F. K. Weissleder, R. Rapid Detection and Profiling of Cancer Cells in Fine-Needle Aspirates. *Proc Natl Acad Sci U S A 106*, 12459-12464 (2009).
31. Chithrani, B. D. Chan, W. C. Elucidating the Mechanism of Cellular Uptake and Removal of Protein-Coated Gold Nanoparticles of Different Sizes and Shapes. *Nano Lett. 7*, 1542-1550 (2007).
32. Jun, Y. W., Lee, J. H. Cheon, J. Chemical Design of Nanoparticle Probes for High-Performance Magnetic Resonance Imaging. *Angew. Chem. Int. Ed. Engl. 47*, 5122-5135 (2008).

33. Laurent, S., Forge, D., Port, M., Roch, A., Robic, C., Vander Elst, L. Muller, R. N. Magnetic Iron Oxide Nanoparticles: Synthesis, Stabilization, Vectorization, Physicochemical Characterizations, and Biological Applications. *Chem. Rev. 108*, 2064-2110 (2008).
34. Shaw, S. Y., Westly, E. C., Pittet, M. J., Subramanian, A., Schreiber, S. L. Weissleder, R. Perturbational Profiling of Nanomaterial Biologic Activity. *Proc Natl Acad Sci U S A 105*, 7387-7392 (2008).
35. Farrar, T. C. *An Introduction To Pulse NMR Spectroscopy* (Farragut Press, Chicago, 1987).
36. Pilnam, K., Keon, W. K., Min, C. P., Sung, H. S., Sun, M. K. Kahp, Y. S. Soft Lithography for Microfluidics: A Review. *Biochip J. 2*, 1-11 (2008).
37. Whitesides, G. M., Ostuni, E., Takayama, S., Jiang, X. Ingber, D. E. Soft Lithography in Biology and Biochemistry. *Annu. Rev. Biomed. Eng. 3*, 335-373 (2001).
38. Zhao, X. M., Younan, X. Whitesides, G. M. Soft Lithographic Methods for Nanofabrication. *J. Mater. Chem. 7*, 1069-1074 (1997).
39. Xia, Y. Whitesides, G. M. Softlithographie. *Angew. Chem. Int. Ed. 110*, 568–594 (1998).
40. Chung, J., Shao, H., Reiner, T., Issadore, D., Weissleder, R. Lee, H. Microfluidic Cell Sorter (Mufcs) for on-Chip Capture and Analysis of Single Cells. *Adv. Healthc. Mater. 1*, 432-436 (2012).
41. Stott, S. L., Hsu, C. H., Tsukrov, D. I., Yu, M., Miyamoto, D. T., Waltman, B. A., Rothenberg, S. M., Shah, A. M., Smas, M. E., Korir, G. K. et al. Isolation of Circulating Tumor Cells Using a Microvortex-Generating Herringbone-Chip. *Proc Natl Acad Sci U S A 107*, 18392-18397 (2010).
42. Weibel, D. B., Diluzio, W. R. Whitesides, G. M. Microfabrication Meets Microbiology. *Nat. Rev. Microbiol. 5*, 209-218 (2007).
43. Geiss, G. K., Bumgarner, R. E., Birditt, B., Dahl, T., Dowidar, N., Dunaway, D. L., Fell, H. P., Ferree, S., George, R. D., Grogan, T. et al. Direct Multiplexed Measurement of Gene Expression With Color-Coded Probe Pairs. *Nat. Biotechnol. 26*, 317-325 (2008).
44. Fortina, P. Surrey, S. Digital Mrna Profiling. *Nat. Biotechnol. 26*, 293-294 (2008).
45. Giljohann, D. A. Mirkin, C. A. Drivers of Biodiagnostic Development. *Nature 462*, 461-464 (2009).
46. Haun, J. B., Yoon, T. J., Lee, H. Weissleder, R. Molecular Detection of Biomarkers and Cells Using Magnetic Nanoparticles and Diagnostic Magnetic Resonance. *Methods Mol. Biol. 726*, 33-49 (2011).
47. Lees, W. J., Spaltenstein, A., Kingery-Wood, J. E. Whitesides, G. M. Polyacrylamides Bearing Pendant Alpha-Sialoside Groups Strongly Inhibit Agglutination of Erythrocytes By Influenza a Virus: Multivalency and Steric Stabilization of Particulate Biological Systems. *J. Med. Chem. 37*, 3419-3433 (1994).
48. Jones, M. R., Osberg, K. D., Macfarlane, R. J., Langille, M. R. Mirkin, C. A. Templated Techniques for the Synthesis and Assembly of Plasmonic Nanostructures. *Chem. Rev. 111*, 3736-3827 (2011).
49. Perez, J. M., Josephson, L., O'Loughlin, T., Hogemann, D. Weissleder, R. Magnetic Relaxation Switches Capable of Sensing Molecular Interactions. *Nat. Biotechnol. 20*, 816-820 (2002).
50. Kim, D., Daniel, W. L. Mirkin, C. A. Microarray-Based Multiplexed Scanometric Immunoassay for Protein Cancer Markers Using Gold Nanoparticle Probes. *Anal. Chem. 81*, 9183-9187 (2009).

51. Yoon, T. J., Lee, H., Shao, H. Weissleder, R. Highly Magnetic Core-Shell Nanoparticles With a Unique Magnetization Mechanism. *Angew. Chem. Int. Ed. Engl. 50*, 4663-4666 (2011).
52. Yoon, T. J., Lee, H., Shao, H., Hilderbrand, S. A. Weissleder, R. Multicore Assemblies Potentiate Magnetic Properties of Biomagnetic Nanoparticles. *Adv. Mater. 23*, 4793-4797 (2011).
53. Aktas, B., Kasimir-Bauer, S., Heubner, M., Kimmig, R. Wimberger, P. Molecular Profiling and Prognostic Relevance of Circulating Tumor Cells in the Blood of Ovarian Cancer Patients At Primary Diagnosis and After Platinum-Based Chemotherapy. *Int. J. Gynecol. Cancer 21*, 822-830 (2011).
54. Armstrong, A. J., Marengo, M. S., Oltean, S., Kemeny, G., Bitting, R. L., Turnbull, J. D., Herold, C. I., Marcom, P. K., George, D. J. Garcia-Blanco, M. A. Circulating Tumor Cells From Patients With Advanced Prostate and Breast Cancer Display Both Epithelial and Mesenchymal Markers. *Mol. Cancer Res. 9*, 997-1007 (2011).
55. Chin, C. D., Linder, V. Sia, S. K. Lab-on-a-Chip Devices for Global Health: Past Studies and Future Opportunities. *Lab Chip 7*, 41-57 (2007).
56. Struelens, M. J., Denis, O. Rodriguez-Villalobos, H. Microbiology of Nosocomial Infections: Progress and Challenges. *Microbes Infect. 6*, 1043-1048 (2004).
57. Urdea, M., Penny, L. A., Olmsted, S. S., Giovanni, M. Y., Kaspar, P., Shepherd, A., Wilson, P., Dahl, C. A., Buchsbaum, S., Moeller, G. et al. Requirements for High Impact Diagnostics in the Developing World. *Nature 444 Suppl 1*, 73-79 (2006).
58. Haun, J. B., Devaraj, N. K., Hilderbrand, S. A., Lee, H. Weissleder, R. Bioorthogonal Chemistry Amplifies Nanoparticle Binding and Enhances the Sensitivity of Cell Detection. *Nat. Nanotechnol. 5*, 660-665 (2010).
59. Haun, J. B., Devaraj, N. K., Marinelli, B. S., Lee, H. Weissleder, R. Probing Intracellular Biomarkers and Mediators of Cell Activation Using Nanosensors and Bioorthogonal Chemistry. *ACS Nano 5*, 3204-3213 (2011).
60. Liong, M., Tassa, C., Shaw, S. Y., Lee, H. Weissleder, R. Multiplexed Magnetic Labeling Amplification Using Oligonucleotide Hybridization. *Adv. Mater. 23*, H254-7 (2011).
61. Agasti, S. S., Liong, M., Tassa, C., Chung, H. J., Shaw, S. Y., Lee, H. Weissleder, R. Supramolecular Host-Guest Interaction for Labeling and Detection of Cellular Biomarkers. *Angew. Chem. Int. Ed. Engl. 51*, 450-454 (2012).
62. Karver, M. R., Weissleder, R. Hilderbrand, S. A. Bioorthogonal Reaction Pairs Enable Simultaneous, Selective, Multi-Target Imaging. *Angew. Chem. Int. Ed. Engl.* (2011).
63. Karver, M. R., Weissleder, R. Hilderbrand, S. A. Synthesis and Evaluation of a Series of 1,2,4,5-Tetrazines for Bioorthogonal Conjugation. *Bioconjug. Chem. 22*, 2263-2270 (2011).
64. Haun, J. B., Castro, C. M., Wang, R., Peterson, V. M., Marinelli, B. S., Lee, H. Weissleder, R. Micro-Nmr for Rapid Molecular Analysis of Human Tumor Samples. *Sci. Transl. Med. 3*, 71ra16 (2011).
65. Reynolds, F., O'loughlin, T., Weissleder, R. Josephson, L. Method of Determining Nanoparticle Core Weight. *Anal. Chem. 77*, 814-817 (2005).
66. Devaraj, N. K., Upadhyay, R., Haun, J. B., Hilderbrand, S. A. Weissleder, R. Fast and Sensitive Pretargeted Labeling of Cancer Cells Through a Tetrazine/Trans-Cyclooctene Cycloaddition. *Angew. Chem. Int. Ed. Engl. 48*, 7013-7016 (2009).
67. Hermanson, G. T. *Bioconjugate Techniques* (Academic Press, San Diego, CA, 1996).

68. Issadore, D., Min, C., Liong, M., Chung, J., Weissleder, R. Lee, H. Miniature Magnetic Resonance System for Point-of-Care Diagnostics. *Lab Chip 11*, 2282-2287 (2011).
69. Brooks, R. A. T(2)-Shortening By Strongly Magnetized Spheres: A Chemical Exchange Model. *Magn. Reson. Med. 47*, 388-391 (2002).
70. Haun, J. B., Yoon, T. J., Lee, H. Weissleder, R. Magnetic Nanoparticle Biosensors. *Wiley Interdiscip. Rev. Nanomed. Nanobiotechnol. 2*, 291-304 (2010).
71. Shao, H., Yoon, T. J., Liong, M., Weissleder, R. Lee, H. Magnetic Nanoparticles for Biomedical Nmr-Based Diagnostics. *Beilstein J Nanotechnol 1*, 142-154 (2010).
72. Han, H. S., Devaraj, N. K., Lee, J., Hilderbrand, S. A., Weissleder, R. Bawendi, M. G. Development of a Bioorthogonal and Highly Efficient Conjugation Method for Quantum Dots Using Tetrazine-Norbornene Cycloaddition. *J. Am. Chem. Soc. 132*, 7838-7839 (2010).
73. Homola, J. Surface Plasmon Resonance Sensors for Detection of Chemical and Biological Species. *Chem. Rev.* (2008).
74. Sendroiu, I. E., Gifford, L. K., Luptak, A. Corn, R. M. Ultrasensitive DNA Microarray Biosensing Via in Situ RNA Transcription-Based Amplification and Nanoparticle-Enhanced Spr Imaging. *J. Am. Chem. Soc. 133*, 4271-4273 (2011).
75. Lee, K., Drachev, V. P. Irudayaraj, J. Dna– Gold Nanoparticle Reversible Networks Grown on Cell Surface Marker Sites: Application in Diagnostics. *ACS nano 5*, 2109-2117 (2011).
76. Ramaswamy, S., Ross, K. N., Lander, E. S. Golub, T. R. A Molecular Signature of Metastasis in Primary Solid Tumors. *Nat. Genet. 33*, 49-54 (2003).
77. Taylor, B. S., Varambally, S. Chinnaiyan, A. M. A Systems Approach to Model Metastatic Progression. *Cancer Res. 66*, 5537-5539 (2006).
78. Spencer, S. L., Gaudet, S., Albeck, J. G., Burke, J. M. Sorger, P. K. Non-Genetic Origins of Cell-to-Cell Variability in Trail-Induced Apoptosis. *Nature 459*, 428-432 (2009).
79. Bruening, W., Fontanarosa, J., Tipton, K., Treadwell, J. R., Launders, J. Schoelles, K. Systematic Review: Comparative Effectiveness of Core-Needle and Open Surgical Biopsy to Diagnose Breast Lesions. *Ann. Intern. Med. 152*, 238-246 (2010).
80. Bast, R. C. J., Lilja, H., Urban, N., Rimm, D. L., Fritsche, H., Gray, J., Veltri, R., Klee, G., Allen, A., Kim, N. et al. Translational Crossroads for Biomarkers. *Clin. Cancer Res. 11*, 6103-6108 (2005).
81. Bolton, K. L., Garcia-Closas, M., Pfeiffer, R. M., Duggan, M. A., Howat, W. J., Hewitt, S. M., Yang, X. R., Cornelison, R., Anzick, S. L., Meltzer, P. et al. Assessment of Automated Image Analysis of Breast Cancer Tissue Microarrays for Epidemiologic Studies. *Cancer Epidemiol Biomarkers Prev 19*, 992-999 (2010).
82. Sheiman, R. G., Fey, C., McNicholas, M. Raptopoulos, V. Possible Causes of Inconclusive Results on Ct-Guided Thoracic and Abdominal Core Biopsies. *AJR Am J Roentgenol 170*, 1603-1607 (1998).
83. Mueller, P. R. vanSonnenberg, E. Interventional Radiology in the Chest and Abdomen. *N. Engl. J. Med. 322*, 1364-1374 (1990).
84. Weissleder, R., Moore, A., Mahmood, U., Bhorade, R., Benveniste, H., Chiocca, E. A. Basilion, J. P. In Vivo Magnetic Resonance Imaging of Transgene Expression. *Nat. Med. 6*, 351-355 (2000).
85. Weissleder, R. Pittet, M. J. Imaging in the Era of Molecular Oncology. *Nature 452*, 580-589 (2008).

86. Durr, E., Yu, J., Krasinska, K. M., Carver, L. A., Yates, J. R., Testa, J. E., Oh, P. Schnitzer, J. E. Direct Proteomic Mapping of the Lung Microvascular Endothelial Cell Surface in Vivo and in Cell Culture. *Nat. Biotechnol. 22*, 985-992 (2004).
87. Nagrath, S., Sequist, L. V., Maheswaran, S., Bell, D. W., Irimia, D., Ulkus, L., Smith, M. R., Kwak, E. L., Digumarthy, S., Muzikansky, A. et al. Isolation of Rare Circulating Tumour Cells in Cancer Patients By Microchip Technology. *Nature 450*, 1235 (2007).
88. Sequist, L. V., Nagrath, S., Toner, M., Haber, D. A. Lynch, T. J. The Ctc-Chip: An Exciting New Tool to Detect Circulating Tumor Cells in Lung Cancer Patients. *J Thorac Oncol 4*, 281-283 (2009).
89. Ho, S. B., Niehans, G. A., Lyftogt, C., Yan, P. S., Cherwitz, D. L., Gum, E. T., Dahiya, R. Kim, Y. S. Heterogeneity of Mucin Gene Expression in Normal and Neoplastic Tissues. *Cancer Res. 53*, 641-651 (1993).
90. Vogel, C. L., Cobleigh, M. A., Tripathy, D., Gutheil, J. C., Harris, L. N., Fehrenbacher, L., Slamon, D. J., Murphy, M., Novotny, W. F., Burchmore, M. et al. Efficacy and Safety of Trastuzumab as a Single Agent in First-Line Treatment of Her2-Overexpressing Metastatic Breast Cancer. *J. Clin. Oncol. 20*, 719-726 (2002).
91. Roth, T. J., Sheinin, Y., Lohse, C. M., Kuntz, S. M., Frigola, X., Inman, B. A., Krambeck, A. E., McKenney, M. E., Karnes, R. J., Blute, M. L. et al. B7-H3 Ligand Expression By Prostate Cancer: A Novel Marker of Prognosis and Potential Target for Therapy. *Cancer Res. 67*, 7893-7900 (2007).
92. Stott, S. L., Lee, R. J., Nagrath, S., Yu, M., Miyamoto, D. T., Ulkus, L., Inserra, E. J., Ulman, M., Springer, S., Nakamura, Z. et al. Isolation and Characterization of Circulating Tumor Cells From Patients With Localized and Metastatic Prostate Cancer. *Sci. Transl. Med. 2*, 25ra23 (2010).
93. Mischak, H., Allmaier, G., Apweiler, R., Attwood, T., Baumann, M., Benigni, A., Bennett, S. E., Bischoff, R., Bongcam-Rudloff, E., Capasso, G. et al. Recommendations for Biomarker Identification and Qualification in Clinical Proteomics. *Sci. Transl. Med. 2*, 46ps42 (2010).
94. Saadi, A., Shannon, N. B., Lao-Sirieix, P., O'Donovan, M., Walker, E., Clemons, N. J., Hardwick, J. S., Zhang, C., Das, M., Save, V. et al. Stromal Genes Discriminate Preinvasive From Invasive Disease, Predict Outcome, and Highlight Inflammatory Pathways in Digestive Cancers. *Proc Natl Acad Sci U S A 107*, 2177-2182 (2010).
95. Cristofanilli, M., Valero, V., Buzdar, A. U., Kau, S. W., Broglio, K. R., Gonzalez-Angulo, A. M., Sneige, N., Islam, R., Ueno, N. T., Buchholz, T. A. et al. Inflammatory Breast Cancer (Ibc) and Patterns of Recurrence: Understanding the Biology of a Unique Disease. *Cancer 110*, 1436-1444 (2007).
96. Erez, N., Truitt, M., Olson, P., Arron, S. T. Hanahan, D. Cancer-Associated Fibroblasts Are Activated in Incipient Neoplasia to Orchestrate Tumor-Promoting Inflammation in an Nf-Kappab-Dependent Manner. *Cancer Cell 17*, 135-147 (2010).
97. Kalluri, R. Weinberg, R. A. The Basics of Epithelial-Mesenchymal Transition. *J. Clin. Invest. 119*, 1420-1428 (2009).
98. Lahat, G., Zhu, Q. S., Huang, K. L., Wang, S., Bolshakov, S., Liu, J., Torres, K., Langley, R. R., Lazar, A. J., Hung, M. C. et al. Vimentin is a Novel Anti-Cancer Therapeutic Target; Insights From in Vitro and in Vivo Mice Xenograft Studies. *PLoS ONE 5*, e10105 (2010).
99. Creighton, C. J., Li, X., Landis, M., Dixon, J. M., Neumeister, V. M., Sjolund, A., Rimm, D. L., Wong, H., Rodriguez, A., Herschkowitz, J. I. et al. Residual Breast Cancers After

Conventional Therapy Display Mesenchymal as Well as Tumor-Initiating Features. *Proc Natl Acad Sci U S A 106*, 13820-13825 (2009).
100. Tsao, M. S., Sakurada, A., Cutz, J. C., Zhu, C. Q., Kamel-Reid, S., Squire, J., Lorimer, I., Zhang, T., Liu, N., Daneshmand, M. et al. Erlotinib in Lung Cancer - Molecular and Clinical Predictors of Outcome. *N. Engl. J. Med. 353*, 133-144 (2005).
101. Tan, D. S., Thomas, G. V., Garrett, M. D., Banerji, U., de Bono, J. S., Kaye, S. B. Workman, P. Biomarker-Driven Early Clinical Trials in Oncology: A Paradigm Shift in Drug Development. *Cancer J 15*, 406-420 (2009).
102. Betensky, R. A., Louis, D. N. Cairncross, J. G. Influence of Unrecognized Molecular Heterogeneity on Randomized Clinical Trials. *J. Clin. Oncol. 20*, 2495-2499 (2002).
103. Liu, Y. Wang, H. Nanomedicine: Nanotechnology Tackles Tumours. *Nat. Nanotechnol. 2*, 20-21 (2007).
104. Alper, J. Us Nci Launches Nanotechnology Plan. *Nat. Biotechnol. 22*, 1335-1336 (2004).
105. Ferrari, M. Cancer Nanotechnology: Opportunities and Challenges. *Nat. Rev. Cancer 5*, 161-171 (2005).
106. Farokhzad, O. C. Langer, R. Impact of Nanotechnology on Drug Delivery. *ACS Nano 3*, 16-20 (2009).
107. Thaxton, C. S., Elghanian, R., Thomas, A. D., Stoeva, S. I., Lee, J. S., Smith, N. D., Schaeffer, A. J., Klocker, H., Horninger, W., Bartsch, G. et al. Nanoparticle-Based Bio-Barcode Assay Redefines "Undetectable" Psa and Biochemical Recurrence After Radical Prostatectomy. *Proc Natl Acad Sci U S A 106*, 18437-18442 (2009).
108. Sun, J., Masterman-Smith, M. D., Graham, N. A., Jiao, J., Mottahedeh, J., Laks, D. R., Ohashi, M., DeJesus, J., Kamei, K., Lee, K. B. et al. A Microfluidic Platform for Systems Pathology: Multiparameter Single-Cell Signaling Measurements of Clinical Brain Tumor Specimens. *Cancer Res. 70*, 6128-6138 (2010).
109. Komohara, Y., Hirahara, J., Horikawa, T., Kawamura, K., Kiyota, E., Sakashita, N., Araki, N. Takeya, M. Am-3k, an Anti-Macrophage Antibody, Recognizes Cd163, a Molecule Associated With an Anti-Inflammatory Macrophage Phenotype. *J Histochem Cytochem 54*, 763-771 (2006).
110. Leimgruber, A., Berger, C., Cortez-Retamozo, V., Etzrodt, M., Newton, A. P., Waterman, P., Figueiredo, J. L., Kohler, R. H., Elpek, N., Mempel, T. R. et al. Behavior of Endogenous Tumor-Associated Macrophages Assessed in Vivo Using a Functionalized Nanoparticle. *Neoplasia 11*, 459-68, 2 p following 468 (2009).
111. Swirski, F. K., Nahrendorf, M., Etzrodt, M., Wildgruber, M., Cortez-Retamozo, V., Panizzi, P., Figueiredo, J. L., Kohler, R. H., Chudnovskiy, A., Waterman, P. et al. Identification of Splenic Reservoir Monocytes and Their Deployment to Inflammatory Sites. *Science 325*, 612-616 (2009).
112. Wildgruber, M., Lee, H., Chudnovskiy, A., Yoon, T. J., Etzrodt, M., Pittet, M. J., Nahrendorf, M., Croce, K., Libby, P., Weissleder, R. et al. Monocyte Subset Dynamics in Human Atherosclerosis Can be Profiled With Magnetic Nano-Sensors. *PLoS ONE 4*, e5663 (2009).
113. Pierga, J. Y., Bidard, F. C., Mathiot, C., Brain, E., Delaloge, S., Giachetti, S., de Cremoux, P., Salmon, R., Vincent-Salomon, A. Marty, M. Circulating Tumor Cell Detection Predicts Early Metastatic Relapse After Neoadjuvant Chemotherapy in Large Operable and Locally Advanced Breast Cancer in a Phase Ii Randomized Trial. *Clin. Cancer Res. 14*, 7004-7010 (2008).

114. Kaiser, J. Medicine. Cancer's Circulation Problem. *Science 327*, 1072-1074 (2010).
115. Hanash, S. Taguchi, A. The Grand Challenge to Decipher the Cancer Proteome. *Nat. Rev. Cancer 10*, 652-660 (2010).
116. D'Alfonso, T., Liu, Y. F., Monni, S., Rosen, P. P. Shin, S. J. Accurately Assessing Her-2/ Neu Status in Needle Core Biopsies of Breast Cancer Patients in the Era of Neoadjuvant Therapy: Emerging Questions and Considerations Addressed. *Am. J. Surg. Pathol. 34*, 575-581 (2010).
117. Khan, A., Sabel, M. S., Nees, A., Diehl, K. M., Cimmino, V. M., Kleer, C. G., Schott, A. F., Hayes, D. F., Chang, A. E. Newman, L. A. Comprehensive Axillary Evaluation in Neoadjuvant Chemotherapy Patients With Ultrasonography and Sentinel Lymph Node Biopsy. *Ann. Surg. Oncol. 12*, 697-704 (2005).
118. Makris, A., Powles, T. J., Allred, D. C., Ashley, S. E., Trott, P. A., Ormerod, M. G., Titley, J. C. Dowsett, M. Quantitative Changes in Cytological Molecular Markers During Primary Medical Treatment of Breast Cancer: A Pilot Study. *Breast Cancer Res. Treat. 53*, 51-59 (1999).
119. Siegel, R., Naishadham, D. Jemal, A. Cancer Statistics, 2013. *CA Cancer J Clin 63*, 11-30 (2013).
120. Na, Y. J., Farley, J., Zeh, A., del Carmen, M., Penson, R. Birrer, M. J. Ovarian Cancer: Markers of Response. *Int. J. Gynecol. Cancer 19 Suppl 2*, S21-9 (2009).
121. Bast, R. C. J., Hennessy, B. Mills, G. B. The Biology of Ovarian Cancer: New Opportunities for Translation. *Nat. Rev. Cancer 9*, 415-428 (2009).
122. Lutz, A. M., Willmann, J. K., Drescher, C. W., Ray, P., Cochran, F. V., Urban, N. Gambhir, S. S. Early Diagnosis of Ovarian Carcinoma: Is a Solution in Sight? *Radiology 259*, 329-345 (2011).
123. Zhang, B., Cai, F. F. Zhong, X. Y. An Overview of Biomarkers for the Ovarian Cancer Diagnosis. *Eur. J. Obstet. Gynecol. Reprod. Biol. 158*, 119-123 (2011).
124. Nolen, B. M. Lokshin, A. E. Protein Biomarkers of Ovarian Cancer: The Forest and the Trees. *Future Oncol. 8*, 55-71 (2012).
125. Li, A. J., Madden, A. C., Cass, I., Leuchter, R. S., Lagasse, L. D. Karlan, B. Y. The Prognostic Significance of Thrombocytosis in Epithelial Ovarian Carcinoma. *Gynecol. Oncol. 92*, 211-214 (2004).
126. Obermayr, E., Castillo-Tong, D. C., Pils, D., Speiser, P., Braicu, I., Van Gorp, T., Mahner, S., Sehouli, J., Vergote, I. Zeillinger, R. Molecular Characterization of Circulating Tumor Cells in Patients With Ovarian Cancer Improves Their Prognostic Significance - a Study of the Ovcad Consortium. *Gynecol. Oncol. 128*, 15-21 (2013).
127. Taylor, D. D. Gercel-Taylor, C. Tumour-Derived Exosomes and Their Role in Cancer-Associated T-Cell Signalling Defects. *Br. J. Cancer 92*, 305-311 (2005).
128. Meirelles, K., Benedict, L. A., Dombkowski, D., Pepin, D., Preffer, F. I., Teixeira, J., Tanwar, P. S., Young, R. H., MacLaughlin, D. T., Donahoe, P. K. et al. Human Ovarian Cancer Stem/Progenitor Cells Are Stimulated By Doxorubicin But Inhibited By Mullerian Inhibiting Substance. *Proc Natl Acad Sci U S A 109*, 2358-2363 (2012).
129. Taylor, D. D., Gercel-Taylor, C. Parker, L. P. Patient-Derived Tumor-Reactive Antibodies as Diagnostic Markers for Ovarian Cancer. *Gynecol. Oncol. 115*, 112-120 (2009).
130. Yip, P., Chen, T. H., Seshaiah, P., Stephen, L. L., Michael-Ballard, K. L., Mapes, J. P., Mansfield, B. C. Bertenshaw, G. P. Comprehensive Serum Profiling for the Discovery of Epithelial Ovarian Cancer Biomarkers. *PLoS ONE 6*, e29533 (2011).

131. Kinde, I., Bettegowda, C., Wang, Y., Wu, J., Agrawal, N., Shih, I., Kurman, R., Dao, F., Levine, D. A., Giuntoli, R. et al. Evaluation of DNA From the Papanicolaou Test to Detect Ovarian and Endometrial Cancers. *Sci. Transl. Med. 5*, 167ra4 (2013).
132. Buckanovich, R. J., Sasaroli, D., O'Brien-Jenkins, A., Botbyl, J., Hammond, R., Katsaros, D., Sandaltzopoulos, R., Liotta, L. A., Gimotty, P. A. Coukos, G. Tumor Vascular Proteins as Biomarkers in Ovarian Cancer. *J. Clin. Oncol. 25*, 852-861 (2007).
133. Emmanuel, C., Gava, N., Kennedy, C., Balleine, R. L., Sharma, R., Wain, G., Brand, A., Hogg, R., Etemadmoghadam, D., George, J. et al. Comparison of Expression Profiles in Ovarian Epithelium in Vivo and Ovarian Cancer Identifies Novel Candidate Genes Involved in Disease Pathogenesis. *PLoS ONE 6*, e17617 (2011).
134. Oribabor, J. W., Ambrosio, A., Castro, C. M. Birrer, M. J. in *Biotargets of Cancer in Current Clinical Practice* 381-402 (Springer/Humana Press, New York, 2012).
135. Kipps, E., Tan, D. S. Kaye, S. B. Meeting the Challenge of Ascites in Ovarian Cancer: New Avenues for Therapy and Research. *Nat. Rev. Cancer 13*, 273-282 (2013).
136. Zorn, K. K., Jazaeri, A. A., Awtrey, C. S., Gardner, G. J., Mok, S. C., Boyd, J. Birrer, M. J. Choice of Normal Ovarian Control Influences Determination of Differentially Expressed Genes in Ovarian Cancer Expression Profiling Studies. *Clin. Cancer Res. 9*, 4811-4818 (2003).
137. Voldman, J., Gray, M. L. Schmidt, M. A. Microfabrication in Biology and Medicine. *Annu. Rev. Biomed. Eng. 1*, 401-425 (1999).
138. Attanoos, R. L., Webb, R., Dojcinov, S. D. Gibbs, A. R. Value of Mesothelial and Epithelial Antibodies in Distinguishing Diffuse Peritoneal Mesothelioma in Females From Serous Papillary Carcinoma of the Ovary and Peritoneum. *Histopathology 40*, 237-244 (2002).
139. Comin, C. E., Saieva, C. Messerini, L. H-Caldesmon, Calretinin, Estrogen Receptor, and Ber-Ep4: A Useful Combination of Immunohistochemical Markers for Differentiating Epithelioid Peritoneal Mesothelioma From Serous Papillary Carcinoma of the Ovary. *Am. J. Surg. Pathol. 31*, 1139-1148 (2007).
140. Laury, A. R., Hornick, J. L., Perets, R., Krane, J. F., Corson, J., Drapkin, R. Hirsch, M. S. Pax8 Reliably Distinguishes Ovarian Serous Tumors From Malignant Mesothelioma. *Am. J. Surg. Pathol. 34*, 627 (2010).
141. Ordonez, N. G. Role of Immunohistochemistry in Distinguishing Epithelial Peritoneal Mesotheliomas From Peritoneal and Ovarian Serous Carcinomas. *Am. J. Surg. Pathol. 22*, 1203-1214 (1998).
142. Ordonez, N. G. The Diagnostic Utility of Immunohistochemistry and Electron Microscopy in Distinguishing Between Peritoneal Mesotheliomas and Serous Carcinomas: A Comparative Study. *Mod. Pathol. 19*, 34-48 (2006).
143. Integrated Genomic Analyses of Ovarian Carcinoma. *Nature 474*, 609-615 (2011).
144. Elschenbroich, S., Ignatchenko, V., Clarke, B., Kalloger, S. E., Boutros, P. C., Gramolini, A. O., Shaw, P., Jurisica, I. Kislinger, T. In-Depth Proteomics of Ovarian Cancer Ascites: Combining Shotgun Proteomics and Selected Reaction Monitoring Mass Spectrometry. *J. Proteome Res. 10*, 2286-2299 (2011).
145. Karst, A. M. Drapkin, R. The New Face of Ovarian Cancer Modeling: Better Prospects for Detection and Treatment. *F1000 Med. Rep. 3*, 22 (2011).

146. Scarberry, K. E., Dickerson, E. B., Zhang, Z. J., Benigno, B. B. McDonald, J. F. Selective Removal of Ovarian Cancer Cells From Human Ascites Fluid Using Magnetic Nanoparticles. *Nanomedicine 6*, 399-408 (2010).
147. Uhlen, M., Oksvold, P., Fagerberg, L., Lundberg, E., Jonasson, K., Forsberg, M., Zwahlen, M., Kampf, C., Wester, K., Hober, S. et al. Towards a Knowledge-Based Human Protein Atlas. *Nat. Biotechnol. 28*, 1248-1250 (2010).
148. LaRocca, P. J. Rheinwald, J. G. Coexpression of Simple Epithelial Keratins and Vimentin By Human Mesothelium and Mesothelioma in Vivo and in Culture. *Cancer Res. 44*, 2991-2999 (1984).
149. Laury, A. R., Perets, R., Piao, H., Krane, J. F., Barletta, J. A., French, C., Chirieac, L. R., Lis, R., Loda, M. Hornick, J. L. A Comprehensive Analysis of Pax8 Expression in Human Epithelial Tumors. *Am. J. Surg. Pathol. 35*, 816 (2011).
150. Armstrong, D. K., White, A. J., Weil, S. C., Phillips, M. Coleman, R. L. Farletuzumab (a Monoclonal Antibody Against Folate Receptor Alpha) in Relapsed Platinum-Sensitive Ovarian Cancer. *Gynecol. Oncol.* (2013).
151. Teng, L., Xie, J., Teng, L. Lee, R. J. Clinical Translation of Folate Receptor-Targeted Therapeutics. *Expert Opin Drug Deliv 9*, 901-908 (2012).
152. Suh, K. S., Park, S. W., Castro, A., Patel, H., Blake, P., Liang, M. Goy, A. Ovarian Cancer Biomarkers for Molecular Biosensors and Translational Medicine. *Expert Rev Mol Diagn 10*, 1069-1083 (2010).
153. Latifi, A., Abubaker, K., Castrechini, N., Ward, A. C., Liongue, C., Dobill, F., Kumar, J., Thompson, E. W., Quinn, M. A., Findlay, J. K. et al. Cisplatin Treatment of Primary and Metastatic Epithelial Ovarian Carcinomas Generates Residual Cells With Mesenchymal Stem Cell-Like Profile. *J. Cell. Biochem. 112*, 2850-2864 (2011).
154. Savagner, P. The Epithelial-Mesenchymal Transition (Emt) Phenomenon. *Ann. Oncol. 21 Suppl 7*, vii89-92 (2010).
155. Heitz, F., Harter, P., Barinoff, J., Beutel, B., Kannisto, P., Grabowski, J. P., Heitz, J., Kurzeder, C. du Bois, A. Bevacizumab in the Treatment of Ovarian Cancer. *Adv. Ther. 29*, 723-735 (2012).
156. Carden, C. P., Stewart, A., Thavasu, P., Kipps, E., Pope, L., Crespo, M., Miranda, S., Attard, G., Garrett, M. D., Clarke, P. A. et al. The Association of Pi3 Kinase Signaling and Chemoresistance in Advanced Ovarian Cancer. *Mol. Cancer Ther. 11*, 1609-1617 (2012).
157. Shepherd, T. G., Theriault, B. L., Campbell, E. J. Nachtigal, M. W. Primary Culture of Ovarian Surface Epithelial Cells and Ascites-Derived Ovarian Cancer Cells From Patients. *Nat. Protoc. 1*, 2643-2649 (2006).
158. Latifi, A., Luwor, R. B., Bilandzic, M., Nazaretian, S., Stenvers, K., Pyman, J., Zhu, H., Thompson, E. W., Quinn, M. A., Findlay, J. K. et al. Isolation and Characterization of Tumor Cells From the Ascites of Ovarian Cancer Patients: Molecular Phenotype of Chemoresistant Ovarian Tumors. *PLoS ONE 7*, e46858 (2012).
159. Han, L., Dong, Z., Qiao, Y., Kristensen, G. B., Holm, R., Nesland, J. M. Suo, Z. The Clinical Significance of Epha2 and Ephrin a-1 in Epithelial Ovarian Carcinomas. *Gynecol. Oncol. 99*, 278-286 (2005).
160. Landen, C. N., Kinch, M. S. Sood, A. K. Epha2 as a Target for Ovarian Cancer Therapy. *Expert Opin. Ther. Targets 9*, 1179-1187 (2005).
161. Lee, J. W., Han, H. D., Shahzad, M. M., Kim, S. W., Mangala, L. S., Nick, A. M., Lu, C., Langley, R. R., Schmandt, R., Kim, H. S. et al. Epha2 Immunoconjugate as Molecularly

Targeted Chemotherapy for Ovarian Carcinoma. *J. Natl. Cancer Inst. 101*, 1193-1205 (2009).
162. Huang, C. Y., Cheng, W. F., Lee, C. N., Su, Y. N., Chien, S. C., Tzeng, Y. L., Hsieh, C. Y. Chen, C. A. Serum Mesothelin in Epithelial Ovarian Carcinoma: A New Screening Marker and Prognostic Factor. *Anticancer Res. 26*, 4721-4728 (2006).
163. Bellone, S., Siegel, E. R., Cocco, E., Cargnelutti, M., Silasi, D. A., Azodi, M., Schwartz, P. E., Rutherford, T. J., Pecorelli, S. Santin, A. D. Overexpression of Epithelial Cell Adhesion Molecule in Primary, Metastatic, and Recurrent/Chemotherapy-Resistant Epithelial Ovarian Cancer: Implications for Epithelial Cell Adhesion Molecule-Specific Immunotherapy. *Int. J. Gynecol. Cancer 19*, 860-866 (2009).
164. Ghazani, A. A., Castro, C. M., Gorbatov, R., Lee, H. Weissleder, R. Sensitive and Direct Detection of Circulating Tumor Cells By Multimarker Micro-Nuclear Magnetic Resonance. *Neoplasia 14*, 388-395 (2012).
165. Kristiansen, G., Denkert, C., Schluns, K., Dahl, E., Pilarsky, C. Hauptmann, S. Cd24 is Expressed in Ovarian Cancer and is a New Independent Prognostic Marker of Patient Survival. *Am. J. Pathol. 161*, 1215-1221 (2002).
166. Richter, C. E., Cocco, E., Bellone, S., Silasi, D. A., Ruttinger, D., Azodi, M., Schwartz, P. E., Rutherford, T. J., Pecorelli, S. Santin, A. D. High-Grade, Chemotherapy-Resistant Ovarian Carcinomas Overexpress Epithelial Cell Adhesion Molecule (Epcam) and Are Highly Sensitive to Immunotherapy With Mt201, a Fully Human Monoclonal Anti-Epcam Antibody. *Am. J. Obstet. Gynecol. 203*, 582.e1-582.e7 (2010).
167. Zecchini, S., Bombardelli, L., Decio, A., Bianchi, M., Mazzarol, G., Sanguineti, F., Aletti, G., Maddaluno, L., Berezin, V., Bock, E. et al. The Adhesion Molecule Ncam Promotes Ovarian Cancer Progression Via Fgfr Signalling. *EMBO Mol Med 3*, 480-494 (2011).
168. Kachali, C., Eltoum, I., Horton, D. Chhieng, D. C. Use of Mesothelin as a Marker for Mesothelial Cells in Cytologic Specimens. *Semin Diagn Pathol 23*, 20-24 (2006).
169. Kim, J. H., Kim, G. E., Choi, Y. D., Lee, J. S., Lee, J. H., Nam, J. H. Choi, C. Immunocytochemical Panel for Distinguishing Between Adenocarcinomas and Reactive Mesothelial Cells in Effusion Cell Blocks. *Diagn. Cytopathol. 37*, 258-261 (2009).
170. Choi, J.-H., Choi, K.-C., Auersperg, N. Leung, P. C. K. Overexpression of Follicle-Stimulating Hormone Receptor Activates Oncogenic Pathways in Preneoplastic Ovarian Surface Epithelial Cells. *J. Clin. Endocrinol. Metab. 89*, 5508-5516 (2004).
171. Ji, Q., Liu, P. I., Chen, P. K. Aoyama, C. Follicle Stimulating Hormone-Induced Growth Promotion and Gene Expression Profiles on Ovarian Surface Epithelial Cells. *Int. J. Cancer 112*, 803-814 (2004).
172. Radu, A., Pichon, C., Camparo, P., Antoine, M., Allory, Y., Couvelard, A., Fromont, G., Hai, M. T. Ghinea, N. Expression of Follicle-Stimulating Hormone Receptor in Tumor Blood Vessels. *N. Engl. J. Med. 363*, 1621-1630 (2010).
173. Zheng, W., Lu, J. J., Luo, F., Zheng, Y., Feng, Y.-j., Felix, J. C., Lauchlan, S. C. Pike, M. C. Ovarian Epithelial Tumor Growth Promotion By Follicle-Stimulating Hormone and Inhibition of the Effect By Luteinizing Hormone. *Gynecol. Oncol. 76*, 80-88 (2000).
174. Jaaback, K., Johnson, N. Lawrie, T. A. Intraperitoneal Chemotherapy for the Initial Management of Primary Epithelial Ovarian Cancer. *Cochrane Database Syst. Rev.* CD005340 (2011).
175. de Bree, E. Helm, C. W. Hyperthermic Intraperitoneal Chemotherapy in Ovarian Cancer: Rationale and Clinical Data. *Expert Rev. Anticancer Ther. 12*, 895-911 (2012).

176. Haber, D. A., Gray, N. S. Baselga, J. The Evolving War on Cancer. *Cell 145*, 19-24 (2011).
177. Paez, J. G., Janne, P. A., Lee, J. C., Tracy, S., Greulich, H., Gabriel, S., Herman, P., Kaye, F. J., Lindeman, N. Boggon, T. J. Egfr Mutations in Lung Cancer: Correlation With Clinical Response to Gefitinib Therapy. *Sci. Signal. 304*, 1497 (2004).
178. Soda, M., Choi, Y. L., Enomoto, M., Takada, S., Yamashita, Y., Ishikawa, S., Fujiwara, S.-i., Watanabe, H., Kurashina, K. Hatanaka, H. Identification of the Transforming Eml4–Alk Fusion Gene in Non-Small-Cell Lung Cancer. *Nature 448*, 561-566 (2007).
179. Hsi, E. D. A Practical Approach for Evaluating New Antibodies in the Clinical Immunohistochemistry Laboratory. *Arch. Pathol. Lab. Med. 125*, 289-294 (2001).
180. Bendall, S. C., Simonds, E. F., Qiu, P., Amir, e.-A. D., Krutzik, P. O., Finck, R., Bruggner, R. V., Melamed, R., Trejo, A., Ornatsky, O. I. et al. Single-Cell Mass Cytometry of Differential Immune and Drug Responses Across a Human Hematopoietic Continuum. *Science 332*, 687-696 (2011).
181. Guo, J., Wang, S., Dai, N., Teo, Y. N. Kool, E. T. Multispectral Labeling of Antibodies With Polyfluorophores on a DNA Backbone and Application in Cellular Imaging. *Proc. Natl. Acad. Sci. U.S.A 108*, 3493-3498 (2011).
182. Shi, Q., Qin, L., Wei, W., Geng, F., Fan, R., Shin, Y. S., Guo, D., Hood, L., Mischel, P. S. Heath, J. R. Single-Cell Proteomic Chip for Profiling Intracellular Signaling Pathways in Single Tumor Cells. *Proc. Natl. Acad. Sci. U.S.A 109*, 419-424 (2012).
183. Niemeyer, C. M., Adler, M. Wacker, R. Detecting Antigens By Quantitative Immuno-Pcr. *Nat. Protoc. 2*, 1918-1930 (2007).
184. Adler, M., Wacker, R. Niemeyer, C. M. Sensitivity By Combination: Immuno-Pcr and Related Technologies. *Analyst 133*, 702-718 (2008).
185. Geiss, G. K., Bumgarner, R. E., Birditt, B., Dahl, T., Dowidar, N., Dunaway, D. L., Fell, H. P., Ferree, S., George, R. D. Grogan, T. Direct Multiplexed Measurement of Gene Expression With Color-Coded Probe Pairs. *Nat. Biotechnol. 26*, 317-325 (2008).
186. Bousquet, J., Anto, J. M., Sterk, P. J., Adcock, I. M., Chung, K. F., Roca, J., Agusti, A., Brightling, C., Cambon-Thomsen, A., Cesario, A. et al. Systems Medicine and Integrated Care to Combat Chronic Noncommunicable Diseases. *Genome Med 3*, 43 (2011).
187. Schadt, E. E. Molecular Networks as Sensors and Drivers of Common Human Diseases. *Nature 461*, 218-223 (2009).
188. Andersen, J. N., Sathyanarayanan, S., Di Bacco, A., Chi, A., Zhang, T., Chen, A. H., Dolinski, B., Kraus, M., Roberts, B., Arthur, W. et al. Pathway-Based Identification of Biomarkers for Targeted Therapeutics: Personalized Oncology With Pi3K Pathway Inhibitors. *Sci. Transl. Med. 2*, 43ra55 (2010).
189. McGranahan, N., Burrell, R. A., Endesfelder, D., Novelli, M. R. Swanton, C. Cancer Chromosomal Instability: Therapeutic and Diagnostic Challenges. *EMBO Rep. 13*, 528-538 (2012).
190. Benoist, C. Hacohen, N. Flow Cytometry, Amped Up. *Sci. Signal. 332*, (2011).
191. Pao, W., Miller, V. A., Politi, K. A., Riely, G. J., Somwar, R., Zakowski, M. F., Kris, M. G. Varmus, H. Acquired Resistance of Lung Adenocarcinomas to Gefitinib Or Erlotinib is Associated With a Second Mutation in the Egfr Kinase Domain. *PLoS Med. 2*, e73 (2005).
192. Pao, W., Wang, T. Y., Riely, G. J., Miller, V. A., Pan, Q., Ladanyi, M., Zakowski, M. F., Heelan, R. T., Kris, M. G. Varmus, H. E. Kras Mutations and Primary Resistance of Lung Adenocarcinomas to Gefitinib Or Erlotinib. *PLoS Med. 2*, e17 (2005).

Appendix A

Primary Antibodies (Chapter 4)

Number	Biomarker	Clone	Company	Cat #	Species	Dilution
1	53BP1	Polyclonal	Cell Signaling	4937	Rabbit	1 to 100
2	B7-H3	185504	R&D	MAB1027	Mouse IgG1	1 to 100
3	B7-H4	MIH43	Pierce	MA1-74439	Mouse IgG1	1 to 100
4	CA-125	X75	Abcam	ab1107	Mouse IgG1	1 to 100
5	CA-19-9	SPM110	Abcam	ab15146	Mouse IgG1	1 to 20
6	Caldesmon	h-CD	Dako	M3557	Mouse IgG1	1 to 30
7	Calretinin	DC8	Invitrogen	180211	Rabbit	1 to 100
8	Calretinin	DAK-Calret 1	Dako	M7245	Mouse IgG1	1 to 50
9	CD15	28	AbCam	ab20137	Mouse IgM	1 to 100
10	CD24	SN3 A5-2H10	Ebioscience	14-0247-82	Mouse IgG1	1 to 50
11	CD44	IM7	Biolegend	103002	Rat IgG2b	1 to 50
12	CD44v6	2F10	R&D	BBA13	Mouse IgG1	1 to 100
13	CD44v9	RV3	Dr. Hideyuki Saya (Keio University)	ALG011	Rat IgG2a	1 to 250
14	CD45	YTH24.5	Abcam	ab30446	Rat IgG2b	1 to 100
15	CD45	H130	Biolegend	304002	Mouse IgG1	1 to 50
16	CD45	Polyclonal	Abcam	ab10559	Rabbit	1 to 100
17	CD56	MOC-31	Abcam	ab134301	Mouse IgG1	1 to 100
18	CEA (a)	M111146	Fitzgerald	10-C10E	Mouse IgG1	1 to 100
19	CEA (b)	M85151A	Fitzgerald	10-C10C	Mouse IgG1	1 to 100
20	CEA (c)	M111147	Fitzgerald	10-C10D	Mouse IgG1	1 to100
21	CEA (d)	487618	R&D	MAB4128	Mouse IgG1	1 to 100
22	CK18	DA-7	EXBIO (Axxora)	EXB-11-110-C100	Mouse IgG1	1 to 100
23	CK19	A53-B/A2.26	Neomarkers (Pierce)	MA5-12663	Mouse IgG2a	1 to 20
24	CK20	Q2	Thermo Scientific	MS1853P	Mouse IgG1	1 to 20
25	CK7	OV-TL 12/30	Neomarker	MS-1352-P0	Mouse IgG1	1 to 20
26	CK8	C-43	Affinity Bioreagents	MA1-19038	Mouse IgG1	1 to 100
27	Claudin 3	385021	R&D	MAB4620	Mouse IgG2a	1 to 100
28	Claudin 7	4D4	Abnova	H00001366-M01	Mouse IgG2a	1 to 50
29	Cleaved Caspase 3	5A1E	Cell Signaling	9664	Rabbit	1 to 100
30	Cleaved Caspase 8	18C8	Cell Signaling	9496S	Rabbit	1 to 100
31	Cleaved Caspase 9	Polyclonal	Cell Signaling	9505S	Rabbit	1 to 100
32	Cleaved Parp	Polyclonal	Cell Signaling	9541S	Rabbit	1 to 100
33	Cyclin D1	CD1.1	GeneTex	GTX26152	Mouse IgG1	1 to 100
34	D2-40	D2-40	Abcam	ab77854	Mouse IgG1	1 to 50
35	E-Cadherin	HECD-1	Life Technologies	13-1700	Mouse IgG1	1 to 30
36	EGFR	F4	Abcam	ab62	Mouse IgG1	1 to 100
37	EMA	E29	Dako	M0613	Mouse IgG2a	1 to 30
38	EMMPRIN	109403	R&D	MAB972	Mouse IgG2b	1 to 100

39	EpCAM (a)	MOC-31	Dako	M3525	Mouse IgG1	1 to 30
40	EpCAM (b)	BerEP4	Dako	M0804	Mouse IgG1	1 to 100
41	EpCAM-FITC	BerEP4	Dako	F0860	Mouse IgG1	1 to 100
42	EpHA2	371805	R&D	MAB3035	Mouse IgG2a	1 to 100
43	ER (Estrogen Receptor alpha)	SP1	Dako	M3634	Mouse IgG1	1 to 100
44	ESE-1	Polyclonal	Abcam	ab1392	Rabbit	1 to 100
45	FGFR-4	4FR6D3	Biolegend	324302	Mouse IgG1	1 to 50
46	FOLR1	548908	R&D	MAB5646	Mouse IgG1	1 to 100
47	FSHR (a)	Polyclonal	GeneTex	GTX108202	Rabbit	1 to 100
48	FSHR (b)	H-190	Santa Cruz	sc-13935	Rabbit	1 to 20
49	FSHR (c)	Polyclonal	Novus Biologicals	NBP-00835	Rabbit	1 to 100
50	FSHR (d)	Polyclonal	Genetex	GTX71451	Rabbit	1 to 100
51	HE4	3F9	Abnova	H00010406-M01	Mouse IgG2b	1 to 50
52	Her2	191924	R&D	MAB1129	Mouse IgG2b	1 to 100
53	Her3	RTJ2	Abcam	ab20161	Mouse IgG1	1 to 100
54	Ki67	B56	BD Pharmingen	550609	Mouse IgG1	1 to 50
55	Ku80	C48E7	Cell Signaling	2180	Rabbit	1 to 100
56	MAGP2	Polyclonal	Abnova	PAB10261	Rabbit	1 to 100
57	Mesothelin	K1	Abcam	ab3362	Mouse IgG1	1 to 100
58	Mesothelioma	ME1	Thermo Scientific	MA2-310	Mouse IgG1	1 to 50
59	MUC1	M01102909	Fitzgerald	10-M93A	Mouse IgG1	1 to 100
60	MUC18	128018	R&D	MAB932	Mouse IgG1	1 to 100
61	MUC2	M53	Neomarker (Pierce)	MA5-11240	Mouse IgG2a	1 to 20
62	p-4E-BP1	17489	Cell Signaling	9456S	Rabbit	1 to 100
63	P-Cadherin	104805	R&D	MAB861	Mouse IgG1	1 to 100
64	p-Cyclin D	D29B3	Cell Signaling	3300	Rabbit	1 to 100
65	p-Histone 3	D2C8	Cell Signaling	3377	Rabbit	1 to 100
66	p-Histone H2Ax	2.00E+04	Cell Signaling	9718	Rabbit	1 to 100
67	p-p44/42 MAPK (p-ERK 1/2)	D13.14.4E	Cell Signaling	4370	Rabbit	1 to 100
68	p53	1C12	Cell Signaling	2524	Mouse IgG1	1 to 100
69	Pan Cytokeratin	C-11	Axxora	EXB-11-108-M001	Mouse IgG1	1 to 100
70	PARP	46D11	Cell Signaling	9532S	Rabbit	1 to 100
71	PAX8	Polyclonal	Proteintech	10336-1-AP	Rabbit Poly	1 to 50
72	phospho-p53	FP3.2	Pierce	MA1-19424	Mouse IgG1	1 to 100
73	Podoplanin	NZ-1.3	Ebioscience	14-9381-82	Mouse IgG1	1 to 100
74	PR (progesterone receptor)	1A6	Millipore	MAB429	Mouse IgG1	1 to 30
75	pS6RP (a)	D57.2.2E	Cell Signaling	4858	Rabbit	1 to 50
76	pS6RP (b)	2F9	Cell Signaling	4856	Rabbit	1 to 50
77	S100	6G1	Fitzgerald	10R-S100a	Mouse IgG1	1 to 200
78	S100-A1	1D5	Abgent	AT3750a	Mouse IgG1	1 to 100
79	S100-A11	2F4	Abgent	AT3752a	Mouse IgG2a	1 to 50
80	S100-A2	M2	Abgent	AT3755a	Mouse IgG2a	1 to 50
81	S100-A4	1F12-167	Abgent	AT3757a	Mouse IgG1	1 to 100
82	S100-A6	6B5	Abgent	AT3759a	Mouse IgG1	1 to 100
83	S100-A7	1A4	Abgent	AT3761a	Mouse IgG1	1 to 100

84	S100-A8	2H2	Abgent	AT3763a	Mouse IgG2a	1 to 100
85	S100-A9	1C10	Abgent	AT3764a	Mouse IgG1	1 to 100
86	S100B	472806	R&D	MAB1820	Mouse IgG2a	1 to 100
87	S100P	4.00E+07	Abnova	H00006286	Mouse IgG2b	1 to 100
88	S6RP (a)	5G10	Cell Signaling	2217	Rabbit	1 to 50
89	S6RP (b)	54D2	Cell Signaling	2317	Mouse IgG1	1 to 50
90	TAG-72	CC49	Abcam	ab16838	Mouse IgG1	1 to 30
91	Thrombomodulin	1009	Dako	M0617	Mouse IgG1	1 to 30
92	Transferrin	29806	R&D	MAB2474	Mouse IgG1	1 to 100
93	TSPAN8	458811	R&D	FAB4734P	Rat IgG2b	1 to 100
94	uPAR	62022	R&D	MAB807	Mouse IgG1	1 to 100
95	VEGF	VG1	Dako	M7273	Mouse IgG1	1 ot 30
96	VEGFR 2	KDR/EIC	Abcam	ab9530	Mouse IgG1	1 to 100
97	Vimentin	Vim 3B4	Abcam	ab28028	Mouse IgG2a	1 to 100
98	WT1	6f-H2	Millipore	05-753	Mouse IgG1	1 to 100

Secondary antibodies (Chapter 4)

Fluorophore	Biomarker	Clone	Company	Cat #	Species	Dilution
Alexa 647	Anti Mouse	Polyclonal	Cell Signalling	4410S	Goat	1 to 900
FITC	Anti Mouse	Polyclonal	Abcam	ab98807	Goat	1 to 300
Dylight 650	Anti Rabbit	Polyclonal	Abcam	ab96886	Goat	1 to 300
PE/Cy7	Anti Rat	Poly4054	Biolegend	405413	Goat	1 to 300
Dylight 488	Anti Rabbit	Poly4064	Biolegend	406404	Donkey Ig	1 to 300
FITC	Anti Mouse IgM	II/41	eBioscience	11-5790-82	Rat IgG2a	1 to 150
FITC	Anti Rat IgG2a	RG7/1.30	BD Pharmingen	553896	Mouse IgG2b	1 to 150
FITC	Anti Rat IgG2b	G15-337	BD Pharmingen	553884	Mouse IgG2b	1 to 150
FITC	Anti Rabbit	RG-96	Sigma	F4151	Mouse IgG1	1 to 150

Appendix B

List of antibodies that were conjugated to DNA (Chapter 5)

Antibody	Catalog	Vendor
GAPDH (14C10) Rabbit mAb	2118BF	Cell Signaling
β-Tubulin (9F3) Rabbit mAb	2128BF	Cell Signaling
Ku80 (C48E7) Rabbit mAb	2180BF	Cell Signaling
Phospho-Chk2 (Thr68) (C13C1) Rabbit mAb	2197BF	Cell Signaling
S6 Ribosomal Protein (54D2) Mouse mAb	2317BF	Cell Signaling
Phospho-Chk1 (Ser345) (133D3) Rabbit mAb	2348BF	Cell Signaling
VE-Cadherin (D87F2) XP® Rabbit mAb	2500BF	Cell Signaling
p53 (7F5) Rabbit mAb	2527BF	Cell Signaling
Phospho-53BP1 (Ser1778) Antibody	2675BF	Cell Signaling
Phospho-(Ser/Thr) ATM/ATR Substrate Antibody	2851BF	Cell Signaling
Phospho-4E-BP1 (Thr37/46) (236B4) Rabbit mAb	2855BF	Cell Signaling
Bim (C34C5) Rabbit mAb	2933BF	Cell Signaling
Cyclin D3 (DCS22) Mouse mAb	2936BF	Cell Signaling
Cyclin D1 (92G2) Rabbit mAb	2978BF	Cell Signaling
mTOR (7C10) Rabbit mAb	2983BF	Cell Signaling
Phospho-Cyclin D1 (Thr286) (D29B3) XP® Rabbit mAb	3300BF	Cell Signaling
Phospho-Histone H3 (Ser10) (D2C8) XP® Rabbit mAb	3377BF	Cell Signaling
ALK (D5F3) XP® Rabbit mAb	3633BF	Cell Signaling
Phospho-EGF Receptor (Tyr1068) (D7A5) XP® Rabbit mAb	3777BF	Cell Signaling
Phospho-Akt (Ser473) (D9E) XP® Rabbit mAb	4060BF	Cell Signaling
CDCP1 Antibody	4115BF	Cell Signaling
Cyclin E1 (HE12) Mouse mAb	4129BF	Cell Signaling
Phospho-Cyclin E1 (Thr62) Antibody	4136BF	Cell Signaling
Phospho-p44/42 MAPK (Erk1/2) (Thr202/Tyr204) (D13.14.4E) XP® Rabbit mAb	4370BF	Cell Signaling
Keratin 7 (D1E4) XP® Rabbit mAb	4465BF	Cell Signaling
Histone H3 (D1H2) XP® Rabbit mAb	4499BF	Cell Signaling
Phospho-p38 MAPK (Thr180/Tyr182) (D3F9) XP® Rabbit mAb	4511BF	Cell Signaling
Phospho-SEK1/MKK4 (Ser257) (C36C11) Rabbit mAb	4514BF	Cell Signaling
Pan-Keratin (C11) Mouse mAb	4545BF	Cell Signaling
Keratin 8/18 (C51) Mouse mAb	4546BF	Cell Signaling
Keratin 18 (DC10) Mouse mAb	4548BF	Cell Signaling
Akt (pan) (C67E7) Rabbit mAb	4691BF	Cell Signaling
p44/42 MAPK (Erk1/2) (137F5) Rabbit mAb	4695BF	Cell Signaling
COX IV (3E11) Rabbit mAb	4850BF	Cell Signaling
Phospho-S6 Ribosomal Protein (Ser235/236) (D57.2.2E) XP® Rabbit mAb	4858BF	Cell Signaling
53BP1 Antibody	4937BF	Cell Signaling
β-Actin (13E5) Rabbit mAb	4970BF	Cell Signaling
Akt2 (L79B2) Mouse mAb	5239BF	Cell Signaling
Phospho-mTOR (Ser2448) (D9C2) XP® Rabbit mAb	5536BF	Cell Signaling
Cleaved PARP (Asp214) (D64E10) XP® Rabbit mAb	5625BF	Cell Signaling
Vimentin (D21H3) XP® Rabbit mAb	5741BF	Cell Signaling
Cleaved Caspase-9 (Asp330) (D2D4) Rabbit mAb	7237BF	Cell Signaling
Met (D1C2) XP® Rabbit mAb	8198BF	Cell Signaling
FGF Receptor 4 (D3B12) XP® Rabbit mAb	8562BF	Cell Signaling
Axl (C89E7) Rabbit mAb	8661BF	Cell Signaling
p38 MAPK (D13E1) XP® Rabbit mAb	8690BF	Cell Signaling
BRCA1 (D54A8) Rabbit mAb	9025BF	Cell Signaling
Phospho-Stat3 (Tyr705) (D3A7) XP® Rabbit mAb	9145BF	Cell Signaling
Cleaved Caspase-7 (Asp198) Antibody	9491BF	Cell Signaling
Cleaved Caspase-8 (Asp391) (18C8) Rabbit mAb	9496BF	Cell Signaling
Cleaved Caspase-9 (Asp315) Antibody (Human Specific)	9505BF	Cell Signaling
PARP (46D11) Rabbit mAb	9532BF	Cell Signaling
4E-BP1 (53H11) Rabbit mAb	9644BF	Cell Signaling
Cleaved Caspase-3 (Asp175) Antibody	9661BF	Cell Signaling
Phospho-Histone H2A.X (Ser139) (20E3) Rabbit mAb	9718BF	Cell Signaling

FGF Receptor 1 (D8E4) XP® Rabbit mAb	9740BF	Cell Signaling
Caspase-8 (1C12) Mouse mAb	9746BF	Cell Signaling
Caspase-9 Antibody (Human Specific)	9502 BF	Cell Signaling
Phospho-β-Catenin (Ser675) (D2F1) XP® Rabbit mAb #4176	4176BF	Cell Signaling
Phospho-GSK-3β (Ser9) (D85E12) XP® Rabbit mAb #5558	5558BF	Cell Signaling
Di-Methyl-Histone H3 (Lys9) (D85B4) XP® Rabbit mAb #4658	4658BF	Cell Signaling
Di-Methyl-Histone H3 (Lys4) (C64G9) Rabbit mAb #9725	9725BF	Cell Signaling
Di-Methyl-Histone H3 (Lys36) (C75H12) Rabbit mAb #2901	2901BF	Cell Signaling
Di-Methyl-Histone H3 (Lys27) Antibody #9755	9755BF	Cell Signaling
Di-Methyl-Histone H3 (Lys79) Antibody #9757	9757BF	Cell Signaling
Acetyl-Histone H3 (Lys9) (C5B11) Rabbit mAb #9649	9649BF	Cell Signaling
Acetyl-Histone H3 (Lys14) Antibody #4318	4318BF	Cell Signaling
Acetyl-Histone H3 (Lys27) Antibody #4353	4353BF	Cell Signaling
Acetyl-Histone H3 (Lys56) Antibody #4243	4243BF	Cell Signaling
Acetyl-Histone H3 (Lys18) Antibody #9675	9675BF	Cell Signaling
LC3A (D50G8) XP® Rabbit mAb #4599	4599BF	Cell Signaling
LC3B (D11) XP® Rabbit mAb #3868	3868BF	Cell Signaling
p21waf1/cip1	2947BF	Cell Signaling
Beclin-1 (D40C5) Rabbit mAb #3495	3495BF	Cell Signaling
CDCP1 Antibody #4115	4115BF	Cell Signaling
β-Catenin (6B3) Rabbit mAb #9582	9582BF	Cell Signaling
Slug (C19G7) Rabbit mAb #9585	9585BF	Cell Signaling
Snail (C15D3) Rabbit mAb #3879	3897BF	Cell Signaling
TCF8/ZEB1 (D80D3) Rabbit mAb #3396	3396BF	Cell Signaling
c-Myc (D84C12) XP® Rabbit mAb #5605	5605BF	Cell Signaling
Met (D1C2) XP® Rabbit mAb #8198	8198BF	Cell Signaling
Phospho-Src Family (Tyr416) (D49G4) Rabbit mAb #6943	6943BF	Cell Signaling
Phospho-Jak2 (Tyr1007) (D15E2) Rabbit mAb #4406	4406BF	Cell Signaling
Phospho-Jak3 (Tyr980/981) (D44E3) Rabbit mAb #5031	5031BF	Cell Signaling
Phospho-PLCγ1 (Tyr783) Antibody #2821	2821BF	Cell Signaling
Bcl-2 (D55G8) Rabbit mAb (Human Specific) #4223	4223BF	Cell Signaling
Bcl-xL (54H6) Rabbit mAb #2764	2764BF	Cell Signaling
Ctrl MIgG1	400102	Biolegend
Ctrl MIgG2a	400202	Biolegend
Ctrl MIgG2b	401202	Biolegend
Ctrl Rabbit	550875	BD Bioscience
Ctrl Rat IgG2b	553986	BD Bioscience
Her2	Herceptin	Genentech
EGFR	Cetuximab	Bristol-Meyers
EpCAM	MAB9601	R&D
MUC1	M01102909	Fitzgerald
MUC16	ab1107	Abcam
EpHA2	MAB3035	R&D
FOLR1	MAB5646	R&D
FSHR	GTX71451	Genetex
TSPAN8	MAB4734	R&D
Claudin-3	MAB4620	R&D
Transferin	MAB2474	R&D
CD44s	BBA10	R&D
CD44	103002	Biolegend
E-Cadherin	324102	Biolegend
Her3	MS-313 - PABX	Labvision
CEA	10-C10C	Fitzgerald
B7-H3	MAB1027	R&D
EMMPRIN	MAB972	R&D
CD45	304002	Biolegend
Calretinin	sc-135853	Santa Cruz biotechnology
Ki67	556003	BD Bioscience
Control Mouse IgG	5414BF	Cell Signaling
Control Rabbit IgG	3900BF	Cell Signaling

Appendix C

List of 70mer alien potato sequences used for unique barcoding (Chapter 5)

Target Sequence	Tm_ (Capture Probe)	Tm_ (Reporter Probe)
GCTAAGTTTGGAATTAAGAAAGGAGTTGCTGGAGGTCCTTTCCAGCATAAGAACCAGCCATATTGCTTAA	79	79
TGCCTTCTGAAAGAGACGTTATTGTTGAAGCAAGAGATAGCTTAGTAACAAATGCTATAGCTCAGGCAGG	80	78
CCTGATCATGCTTTGTCAGCAGACCCAGAAGAATTCATCACAATCACTGGAAGATTGAGCTTAGGAAAGT	82	78
GAGCGGATGTTATTGAGAAGCACTTTACCTTAGATTTCTAAAGCTCTCTTCCTCCTCTCTTCTCCGCTCA	78	82
ATCGGCTGTGCGATTGCTATTGATGTGTTAAGAAATTTGGTTTGTGATTGGCAAATCTCTCCTCCAACTC	80	81
ATTTGGATGAAGTCGGCTTTATGGTGACACAAATCATGATGAGCTGAGGTTCTGACAGCAAATACGCTCA	79	82
ATAGAACCATTTGCTGATGAGGTGACAACAGATCGTTGCACTTATGCTATCCCGTTAGACTATCTGCTAT	80	78
ACTACCATGTACTGCGCGAGACTAGCCTATCATTGGATTGCAGCGATGACTATATCTGAGCACCTGTGAC	82	81
ATATGAGACGACTAGCACGCCATAGCGTTACATACGTGTCGATCCGAGAACATCACTCTAATGACGAGTG	80	81
CATCATCGACAGTTCGCAGCCCTATAACATGATACTAGATAACGATGCTCCATGTTAGTGAATGCGAGTC	80	79
ACTCACACATAGTACTGACACGTAAGATAGGATGCTATATGGTCATTGGTCACCCGAGTTACGATCAAAT	79	79
CAGATAGACTCACCTCGATATACAGGGAGCCACGACTTAGGACTATGGATAAGTCATCTAAAGCGTCCGA	82	78
CACTGTCTATACATGGACGACACTTTGCACATCATTACCAAAGAGCGCAACGTATCTAGGATTGAGCAGT	80	81
AGACTAATTGATCGGACCGATGACAGTTCACAGAGGGATACACTGTTGAGCCGACCCTATTAGCTGATAT	80	80
TGATCCACACTGACGAATCATGTACTCACTCGATCGCCACTTCACACAAGAACACAAATTTGGAGTATTG	80	79
CTCGAGAATCACACACAGTCGTCTAAGACACGACAAGTGCAACAGCAATCCACATCTTAGATGAGATTAG	81	78
CGATTACAAGGCGTGGTCAGATATTAGACTCCAGGGGATTTAATGCCAGTCCAAGCTCTCTTCCACATTC	81	81
ATCTGCATGAACGGGAAAGGAGTTCGATGAGACTTTCAAACCAACATAATGTCTCTCCAACCTCAGGAAG	82	80
ATAGTCTTTAGAGCCTCAGAATAGGCTGTGACGCGGAAGATAACTCATAAGTGCCTCCCTCGGTAATTTG	82	79
GCCAGGTATGCCGTGAACGAGTTCTTCATTAACTGTTATGTCTCGGGAGTCTGATATTGGTACTTCTCCC	82	80
TTAGCACCGATATCAATACTGATGATGTCACCGTCGAGCTCGTGTTGAACCCTTCAAGTAACAACCTGAC	79	82
ACTTGTTCGACTGACAGTTTAACGCCTGACATGAACGGCTTGCTTATAATGACTGGCAGGGTTATGAATG	81	81
AAACTGACCGTACCGTTAGAAGAGAGTTCCGCTTCTCTCATGATGTGCGCATCTCCCACATTATTTGACC	82	81
TGATGACAGTGACAATTGACCGAATTGCCTGATCATTACCTTACAGTGCGCAGATTGGGATAATCGATTT	81	79
TAGGCGTTGAGGCTTTGTTTCTTTGCCTCTATTGTAAGACTCATTCTGACGGCCTCTAGTCGTTGATATG	81	80
AAGGACATTCTTTCGAATGCAAGTTCAAGGCACATTTTCTATATCAGCCACCATGGGAGTGACATTTCTT	80	79

Target Sequence	Tm_ (Capture Probe)	Tm_ (Reporter Probe)
CAATAGCTCCAGTAGTAATTGTTGTCGCTCCGCTGAGCAGTTAATCCTTATGTCAACAACCTCAGCATAG	82	78
TTCACCAAGCTGAACAGGGTTGCGCTGAATAAATTTTACAGGATACTATGGACAGGTTCAGAATCCTCGA	82	79
GGAATGAATCCATTGCATTTCCATGAGAATGCAGACTTAATCGGACGTATCGACTTTGGGTCCACGATAT	79	80
GAGGTCTTGTTTCATCTAAACCGAGCAGGATGATAAGCCATAATTCGTAACCCGAGGGTATAATTCGTTA	79	79
GTCCTTCTGCTTATGACATTCCGTGCATTCCGTAGCTACGTCAAGCGTTACATAGTGACGGAACTGTTAG	82	80
TCTGTACCTTGGCACTCCATCTGGTAAGTCACTTATAGTTGTATGGTTTCAGATGAGGGAACGTGTAGGA	81	80
AATTTCTGAGATTGTTGGTAGAGGGAGAAATGGGAAGGACATGTTTCAACAATCACCGGATTAAAGCCTT	79	80
TGTGGAAGGACTGTGATAAACCAATAGGGTGTCAAGATCTGTAAGTATGGGATTAGGGATGTTCTGCCAG	80	80
GCCGTCGGACATAACCACTTGGATATATACGTAGTTCATCAACCTTAACTCCCTCTGGGTTCATTGGGAG	80	82
GCTATTGCAGCAAAGAGAACAGACGCTTTAACTGGTATCGAGCGCTTAGATGGCTATATGGTCTACTAGA	81	78
GAAATCAGATCAGTTCTACATTCGGTGGGAGCCCTCTATATGATTAGATCCTGCAGCCGTACTTCCGTCA	82	80
GGTGGCTTGATTTAACTGAATCAGGCCCTAACCATTTGTATTGTGTCTACACTGGTCCGTTCTTAGACGC	82	81
GTTGTTTACCTTGTAGATCGACTTCACATCAGCGGCAGAAGGCCCTCAACGTAAATCTGCTCCACATTTA	80	81
TGTTGACATCCGCAACAATGTACCTTATATCGGCATATGGATCTCTTGATCGAGCGAACCTCCCTTTAAC	81	80
AAGGTGATTCACTAACCAGCTCTTACTCCTCGTTCGGTAGCAAATGAAATGCCGGATGCTGTTGAAGTAG	80	81
CGCATAACTCGAACCACAGTTACTATCAGTCGACATCCCACCAGAGAAATTGAAGGATATTGTTGAAGCA	80	79
GAATCTTGGAAGGTTTCCAGTTAAATAGGGCGTGCGAAGATTCCAGGCAGATTTCTCAGGAATTCAGTCA	81	80
CTGCTAATGCTGATGGCCCACCTTCTCTATTTGTCGCCATTATATGCGTTGAGGTTAGTTCAAGCAATAC	82	78
GAACAGCTTTCCTTGCTCCCTCTAAATCACCATTTCCATTAGATGAAACCGACTTCATTCCAGACTCAAT	80	78
AATGCATTTGCCAATGTAGCCATTGTATAACCAGATACACTAGTCCAATGTCTCAACCAGGGATACCACA	79	81
CTCAGAGCTTCAAATCTATCCTCTGGAATCTCTGTATAAGCCCTCGAATACAACTTGAGGTATCCCGCAT	79	81
CTCTTCTGCCCTACATCACTATCGACTATAGCAACATATCTTTCTCGGGTAAAGATTAGGCGTCCGATAT	79	78
GTAACCGTAGTCGCGCAAACCGTTATATTACGGATATGATCCAAGTTATATACATTAGGACGCGGTTGCT	81	79
ATGGTTAGTAAACAGCTTTGATTTCTACATCCGCCTAGCAAACCCATAGTTCTGCAGTAGATTCACAGCG	79	81
TTCAGTTATAATGTGTCCAGCAGAAGCAGGAATTGAATTACCCAAGTTGCAAGTGGAAGATTTGGAGTTA	79	78
TTGCAGAAGCATTCCCAATATGGGTTTCAAGAGTTTAAAGAATGTGGAACATTCATGGGAACTGGTGAAG	80	79
GCAACAACCTCATCTATACTGTGAATAGTCCCTCCGCTGTCTATATTGGAACTGCTGCAATGGTTGCTCT	80	82
CCGCAGATTATCGTTTACGATGCATCCATGGTCTCCGACCCATTGAGAGAGCCAATGGAATTAAGAACTT	82	80
CACCATTCAGCCTGATATTGCGTTTGGTGTTGATGTGGCAACTGCATACTGAATAACTCCCTGAAATAGC	81	80
CGTTACATACTCAGCCATAGGCTTCGATAACAGCATTATTGGAACCTCTGGGACATTAACAGAGACAACA	81	79

Target Sequence	Tm_ (Capture Probe)	Tm_ (Reporter Probe)
AGCGTACTAGGCATCTATTGGCTGAACTACCATGTAATTAGTGGTGTTCCAGCCTCTAAGATGATGTGGT	81	80
GATAGGATGCGACTGCGTATCATATAGGCTGCACATTAGCTGTTGCTTCAAATGCCAATCTTACCTCAAC	82	79
AATGTATGAGCGGACACTATGCTAAGAGAGACTCCATCAATCCCTCTATGCAAGATAACAACATCTGGCT	80	79
TGCACATCATAGTGCGACGTTGATCCAGATAGACTATAAGACGGCTTGGCATTTACCCTAGTCACTATCT	81	80
AATGTGTCAGCGGCCTAACTGTAATTGATCCACACCTTAGTTCGGGAGCTACCGATCTAATCAACCGTTT	82	80
AGACTCCAGGTCGATCATTGGATAACCAACCAGTCGGTTATCCATGACGAGTGAATAATCTTACCGCAGG	82	80
TTTAGATCCTAAGAATGCGAAATGCCGATTCCCGCATATTTCGTAAGCTCGTTCGGGACTTTGTATCGGC	82	81
GAGTGATAGGATCACTCTAAGATCGGCCACTATACGACGCTGAGGTTTATATGAACGGCCGCAATTATGA	79	81
TCTTGACCAACACCATGTCCGACATACTCCCTAACATGGGTACGGCGACTACTGAATCGTTCTTTGAGAG	82	82
TGTGTAAATGAAAGCATCTGACTCAACAGGCATCAGTAACGATAATGAGTACAACGCCCAATGGTCATAG	80	79
GCTTCAACGATTTCAATATACCCATTCGTCAGAGGAAGTAGTAGATCCCGCCGTCTTAGTCGGATTGAAA	79	81
TGTGGTTCCGGTTGCGTATAGATCATGATTCTTTACCCACCTCTTGCTGTAATGACCACAATCAACGTAG	79	82
GTATCGGCGAACACGAAATCCTCTACTCTTGACAAACTCCCATTCCTACCTCTCCAAAGTTAGAGGAGAT	81	80
TTGCATTACAATGGCCGATCAAGATAAGGACATTCATAATGGAGCTATAGAATACAACACCAACGTCGCA	79	79
TAATTCTTCCTTGATTCCGTGATTGGATGTCCCTCAGGAGTAGTAGTGTGGATGTTGTTGTTAGACACTT	79	78
TGGAGGGTCGTAACCGCTATAGATGTGATTCACTCCAACAACTTCCCTATCTTTAATCCTCTCACTCCAC	81	78
TGAATAAATTCGTTGGCGCTGTAGAGATCGGAGTTCCGGATTCGTACTACTCGTTTACGGGATTTACAGA	80	80
GCTAAAGGAGACTCCGGTTTAAACGTCATCGCAATCTTTGATGGGCAAGCGAGCACATAGATATGCGTTA	81	82
AATATTCTCCGGCATGAATGGCGTGGGAATGAATCCGGCTTTGTGTTTATTGTACATAGACGTTGTCCCG	82	81
GAGAACGAGCGGAGCAAGATAGCCTTTAACTGAATCGTCGTCTTATTCCCAGTACACATCATTCCAAATG	81	79
ATATTCTGTACTCAGTGCCTATCCACCTAATAGGGACCTCAGCGACCTGTCCGTTACATTAATGAAACAT	78	81
CATTCCGTAGAATTACTACACCGCGGGATCATTATAACGTCGAAGAGCTTCAGAGGTAAGTGAAACAAGG	79	81
CCCGAAGGCATAATCAACATCCATTGTACATCCCTTGTTATAGCTCCAGGGCCAGAGATTAAAGGAATAG	81	79
CTAGGATGTAACTTGCGTTAGTTGCAGATTCGCTATATTGCTTAAGCTCTGAGCTCCATGTCCAGTAATT	79	79
TTCTCGCAGTTGTAAACTTATAGTGTCGCGCCTAGAAATTCATAGCCACAAATTCTCTTTGGGCAGAGAT	81	78
TATAGTTACCAAGTACTATGGGTTGGTGGAAGCCGAACGTCTGTCCAAATGGAGCTATAGTTAAGAGGGA	80	80
AGACGCACACCGATAGAGGAGAGATCTTACATACCTGCTAAGGTTGTTAATGGCATTGCAGATAGCTTAG	81	79
CCAGAAAGGTACAGGGCCAATTAACACGTAATCGGCCTCCAACTCTGCCATCTTTAAGCATTCTAAAGCT	82	80
AATTCTCCGTCATGTGGTCGTCTGATGCCTAACTTTATCTGCTATCAATGTAGAGGATCGTGCATTACCG	82	79
CGCGGGCTAAGTAGTAGGGTTCTAATGCTACTTTAAATACGCTCACAATCCAGGCTATATCGCTGTAGCT	80	81

Target Sequence	Tm_ (Capture Probe)	Tm_ (Reporter Probe)
TAATCACTGTATTTGTTAATCATGGCTAGGCGGGTCCAATAGGGAAACTGATACTAACGTAGGAGCACGC	79	81
GTATTCTGGAGAACCTCGTGGCAATGGCAATTCTCCACGAGTGCTAAGATCTGAGCCGTTTACCAAAGAG	82	81
ATAACCTGGTCTCCGGTTGATCGTTTACCTGAAACATGAGATTAGCAACGACCCAAACATGCCACTTCAC	81	82
CACAACATGCAGCAGGCAAGTAGGGTTTCTGATTATAAGCATCCAGCAATAAAGCCTCCTTCAAACCAAC	81	81
CCCTAACCATGTTCTACGAGCGGTCACAGATTATATTCAACTACAAGTGTAAATGTACGAGCGCCGAGAT	80	80
GAAAGGCATTTGACGGGAGCATTGACGAAGACATACGGTAATTTGTCGTCGCACGGACAATTAGTGAGTT	82	81
TAATACTGGGTCACAAGATTAGATTCCAGCTGTGACGGCGATGAAGTCCGCGAGGATATGTTTCTATATC	78	81
GGTTCATTGTCTCATCGTACGGCTAATGTAGATACGAGGTAGCCGAGTATGACACACCACAGCAGTTAAT	78	82
TTATGGATTCCGATGATCCTCCGCGTGGTACAAATGTTACCTTGATGCAATAGTCTCTGTATGCGATCGG	82	80
AGCGGTACTAATATGCTATGAGCGAGTTCCCTAACGAGAGATAACGACCCTCTGTCGTAAGCACTTAAGG	80	81
GAGGCATCTCTGCTAACTATATGCTGAACAGCTTTTCCACGATATAGGTACATTGGACGCTTACAGGATA	80	79
TTTCGGCCCAACTTATATGCTCTCCGAATCTTGGAGCAGTCATCGTAACCTGATAGCAATCTACGTCAAG	82	80
ACTGCAGTGAGGGCAACCAATACAAATTAAATCTGCCTCCTATTGGGATACCTCCCGTCCATTAAGTTAG	79	80
TTGGAGAAACAACCATACAGGTGTCTTTAACTACCTGGAACTCTACCAATTGGAGCTTTCTTAGCTGTCT	78	80
GCTATCAACTTCCCTATCCAAACCGTTGGATGAATTGAAAGCATAGATGTTCCTTGGAGAGGTTTCCCAG	80	81
TGAGGAGTAAGTATACGACGCCTGCACTAGTCACTTGCTGGCTTTGAGCCAATAGATGTGTTAATGGCTA	82	81
CACAGCCAATCTCTTAGGACAGTACATGGTTAGTAACGTCTGTGGAAGTCATGAGCACACGATCTGTAAG	79	82
TGAGTATCTACAGGTGTTCTCATGGGATCGTAGTTGGTCTGTCCAACATGACGTTATAGGCATAACTCCA	79	81
TACCTTAAACTGCGCTGGTAACTTGGATCGTGTAGTCATTGGGAGCAAACCATCTGTCTTTCGTATGGAG	81	81
GTTAGGTTCAGCCTCATTCCCTAAGAATCCAACTCATAACTCAATCATGCGCGTCCAGCAAAGACAAATG	80	81
ACTGTCTAATACAACCGGATTCTAAGACCACATGGTCTTAGACGCGCGTGCAATTCTGAACTATATGATT	79	79
TGGCTATTGCCGCAGTAGATCAAAGATTGAGAGAGATATAGATTACTCCATGATACACCCAAGCCTCGAC	81	79
GCAACAAGTGATGCTGACGCAGTTGTTATAGATGGCCTTTGGCTCACGCTAATTGAGTTACTGTAGGAAA	81	80
GCTATCTCACCAGCTCCTCACCATGACATTTACTCTCCACATTTATCTGCGACCTGTTTCGTAAACGATG	81	80